INVESTIGATION OF METHODS TO IMPROVE PROCESS PERFORMANCE IN CENTERLESS GRINDING OF INCONEL 718 AND TI-6AL-4V SUPERALLOYS

A Thesis
Presented to
The Academic Faculty

By

Sead Dzebo

In Partial Fulfillment
of the Requirements for the Degree
of Master of Science in the
George W. Woodruff School of Mechanical Engineering

Georgia Institute of Technology
December, 2009

INVESTIGATION OF METHODS TO IMPROVE PROCESS PERFORMANCE IN CENTERLESS GRINDING OF INCONEL 718 AND TI-6AL-4V SUPERALLOYS

Approved by:

Dr. Shreyes Melkote, Advisor
George W. Woodruff School of
Mechanical Engineering
Georgia Institute of Technology

Dr. Roshan Vengazhiyil
H. Milton Stewart School of
Industrial and Systems Engineering
Georgia Institute of Technology

Dr. Steven Danyluk
George W. Woodruff School of
Mechanical Engineering
Georgia Institute of Technology

Dr. Kyriaki Kalaitzidou
George W. Woodruff School of
Mechanical Engineering
Georgia Institute of Technology

Date Approved: 11/13/2009

ACKNOWLEDGEMENTS

First, I would like to thank my advisor Dr. Shreyes Melkote for all the academic guidance and support throughout the course of my graduate studies. I would also like to thank the members of my thesis committee, Dr. Steven Danyluk, Dr. Roshan Vengazhiyil, and Dr. Kyriaki Kalaitzidou for their input and constructive feedback on the thesis topics. I would also like to thank all the members of the MARC staff, especially John Morehouse for providing organizational assistance and Steven Sheffield and John Graham for providing equipment training in the machine shop and metrology labs.

Second, I would like to acknowledge my colleagues Ramesh Singh, Xavier Brun, Thomas Newton, Mukund Kumar, Alex Williams, and Andrea Marcon and thank them for their assistance with all the experiments.

Third, I would like to acknowledge Alcoa Fastening Systems (AFS) for sponsoring this research study and thank all the members of their engineering team for providing technical assistance and material supplies for the project.

Finally, I would especially like to thank my family members for their encouragement throughout the course of my graduate studies. The completion of this thesis would not be possible without their unconditional support.

TABLE OF CONTENTS

LIST OF TABLES

LIST OF FIGURES

LIST OF SYMBOLS

U_d	dressing overlap ratio
w_d	cutting width of dressing diamond
s_d	dressing lead
V_f	feed rate
Δx	radial infeed distance
V_g	grinding wheel surface speed
D_g	grinding wheel diameter
$\bar{D}_g$	average of wheel diameters before and after wear
Δr_g	decrease in wheel radius due to wear
ΔV_g	volume of radial wheel wear
V_r	regulating wheel surface speed
N_r	regulating wheel rotational speed
D_r	regulating wheel diameter
V_w	workpiece surface speed
N_w	workpiece rotational speed
D_w	workpiece diameter
b	grinding width
D_e	equivalent diameter
d	stock removed or diameter reduction per pass

WM	grinding wheel material
a	depth of cut per workpiece revolution
a_i	depth of cut at beginning of spark-out stage
a_f	depth of cut at end of spark-out stage
t_s	spark-out time
n	number of workpiece half-revolutions
N	number of full workpiece revolutions
Q_w	volumetric material removal rate
Q_w'	specific material removal rate
h_{eq}	equivalent chip thickness
e	specific grinding energy
e_{ch}	specific energy for chip formation
e_c	critical specific grinding energy for workpiece thermal damage
R_t	theoretical fraction of heat energy conducted to workpiece
R_w	experimental fraction of heat energy conducted to workpiece
R_g	experimental fraction of heat energy conducted to grinding wheel
R_c	experimental fraction of heat energy conducted to chips
R_f	experimental fraction of heat energy conducted to fluid
P	grinding power
ρ_w	density of workpiece material
κ_w	thermal conductivity of workpiece material
c_w	specific heat of workpiece material

α_w	thermal diffusivity of workpiece material
ρ_g	density of abrasive grain material
κ_g	thermal conductivity of abrasive grain material
c_g	specific heat of abrasive grain material
T_c	grinding zone temperature at onset of workpiece burn
T_m	melting temperature of workpiece material
$(\kappa\rho c)_w$	workpiece material thermal coefficient
$(\kappa\rho c)_g$	grinding wheel material thermal coefficient
r_o	grain contact radius
K_t	heat flux distribution coefficient
l_g	wheel-workpiece geometric contact length
R_a	arithmetic average surface roughness
DE	diameter error
TRE	transition radius error
β	tangent angle
α'	work blade angle
γ	center height angle
ψ	regulating wheel tilt angle
K	machining elasticity parameter
θ	workpiece angle of rotation with respect to grinding wheel contact point
$\theta - \alpha$	workpiece angle of rotation with respect to work blade contact point
$\theta - \alpha + \beta$	workpiece angle of rotation with respect to regulating wheel contact point

δ_1	magnitude of irregularity at work blade contact point
δ_2	magnitude of irregularity at regulating wheel contact point
$r(\theta)$	instantaneous reduction of workpiece radius at position θ
$X(\theta)$	set reduction of workpiece radius at position θ
h	workpiece center height
η	S/N ratio parameter
$c_0, c_1 ..., c_n$	regression model coefficients
ε	random error

SUMMARY

Grinding is an abrasive machining process widely used for the final shaping of components that require very smooth surfaces and a high dimensional accuracy. The performance attainable in this process as measured by levels of productivity, cost, and final part quality is determined by the selected combination of (i) the machine tool, (ii) workpiece material (iii) grinding wheel (iv) setup parameters, (v) grinding parameters and (vi) grinding fluid. In many industrial operations, the grinding parameters are still commonly selected according to machining data handbooks or machine operator experience. However, selecting the grinding parameters solely based on prior experience without establishing any guidelines to verify whether or not the selected values are optimum for an operation can be very costly for any high-volume manufacturer. In many cases, the selected parameters are too conservative and not adapted to maximize the utility of the machine tool and the grinding wheel. A similar practice is prevalent in the selection of grinding fluid application settings, where different oils are typically used to flood the grinding contact zone without considering more effective alternatives. Although grinding has been used extensively in the production of precision components, these common practices confirm that it still remains one of the least understood and most inefficiently conducted machining process in the manufacturing industry.

In recent years, the costs of the grinding operation have increased further with a greater demand for high-strength, low-weight superalloy components. Titanium and nickel-based alloys commonly used in the aerospace industry demonstrate high creep-rupture strength and excellent corrosion resistance in high-temperature environments

including gas turbines, engine combustors, pressure vessels, and heat exchangers. Although they possess excellent performance characteristics, these alloys are very difficult to grind due to a combination of poor thermal properties, work-hardening behavior, and high strength and chemical reactivity at elevated temperatures, leading to unsatisfactory material removal rates and rapid grinding wheel wear. As the hardness of materials processed by grinding continues to increase, it becomes even more important to find effective ways to improve the productivity of this material removal operation.

In this thesis, two different methods are investigated for improving process performance in the plunge centerless grinding of Inconel 718 and Ti-6Al-4V superalloy fasteners: (i) economic optimization of grinding process parameters and (ii) reduced quantity lubrication using a grinding fluid enhanced with solid lubricant additives. In the first part of the thesis, a systematic methodology is developed and carried out using Taguchi's Design of Experiments (DOE) method and classical machining economics theory to find the optimum grinding conditions in two stages: (i) modeling of process and part quality constraints (ii) determination of optimum grinding conditions in the feasible operating region. In the second part, the performance of a graphite nanoplatelet-enhanced grinding fluid in reduced quantity lubrication centerless grinding is evaluated to assess its potential as a cost-effective alternative to the traditional flood cooling method. The results indicate that an appreciable reduction in the cost of the superalloy grinding operation can be achieved by operating at the cost-optimum parameters. In addition, it is shown that the application of a graphite-enhanced fluid at a reduced flow rate is more effective than high-volume flood cooling in reducing specific grinding energy levels and wheel wear rates, thus offering the potential to increase the process productivity.

CHAPTER 1

INTRODUCTION

1.1 Background

Centerless grinding is a high-precision, shallow-cut finishing operation used in the mass production of cylindrical components. Developed in the 1920s, this profiling operation is able to achieve extremely precise dimensional tolerances for cylindrical parts with outer diameters of 0.003-3 in. (0.0762-76.2 mm). Some of the components typically produced in large quantities by this grinding operation include drill bits, piston pins, rotary shafts, valve stems, needles, fasteners, roller bearings, and bearing rings as shown in Figure 1.1. Centerless grinding holds several advantages over center-type cylindrical grinding in production, including shorter machine setup times, shorter part loading times, and a higher dimensional accuracy.

Figure 1.1: Cylindrical components produced by the centerless grinding operation

The basic elements of the centerless grinding system are the grinding wheel, the regulating or control wheel, and the workpiece support blade as shown in Figure 1.2. In contrast to center-type cylindrical grinding where the part is chucked and rotated by an external motor, centerless grinding does not utilize a mechanical fixture to constrain the motion of the part. Instead, the part is supported on its own outer diameter by an inclined rest blade and its rotational motion is controlled by a low-speed regulating wheel that serves as a frictional driving and braking element (Figure 1.2). Based on the initial shape of the part, two primary part feeding methods are used to achieve the final desired part geometry in this operation, including through-feed and infeed or plunge centerless grinding. Through-feed centerless grinding is used to shape straight or tapered cylindrical workpieces and infeed or plunge centerless grinding is used to shape cylindrical workpieces that have projections, multiple diameters, transition radii, or other irregular geometric features. In the plunge centerless grinding of fasteners analyzed in this study, the regulating wheel is retracted and the part is loaded from above onto the support blade. The part is then plunged to a set distance in the radial direction into the rotating grinding wheel to remove the desired amount of material.

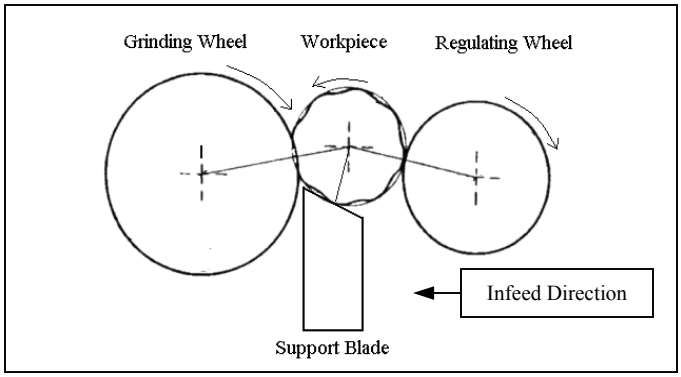

Figure 1.2: Basic elements of the centerless grinding system

As shown in Figure 1.3, the levels of productivity and final part quality attainable in the centerless grinding operation are determined by the selected combination of (i) the machine tool, (ii) workpiece material, (iii) grinding wheel, (iv), setup parameters, (v) grinding parameters and (vi) grinding fluid. For a particular workpiece material and geometry, the selection of grinding parameters and grinding fluid is primarily guided by the specified part quality levels. In many industrial applications, the productivity of the grinding process is a secondary objective since it is very difficult to determine the effect of each input parameter on the key process responses without incurring large capital expenses for the costly and difficult-to-grind superalloy materials. Consequently, many grinding operations are still conducted at suboptimum productivity levels without evaluating or implementing solutions that can improve the process performance.

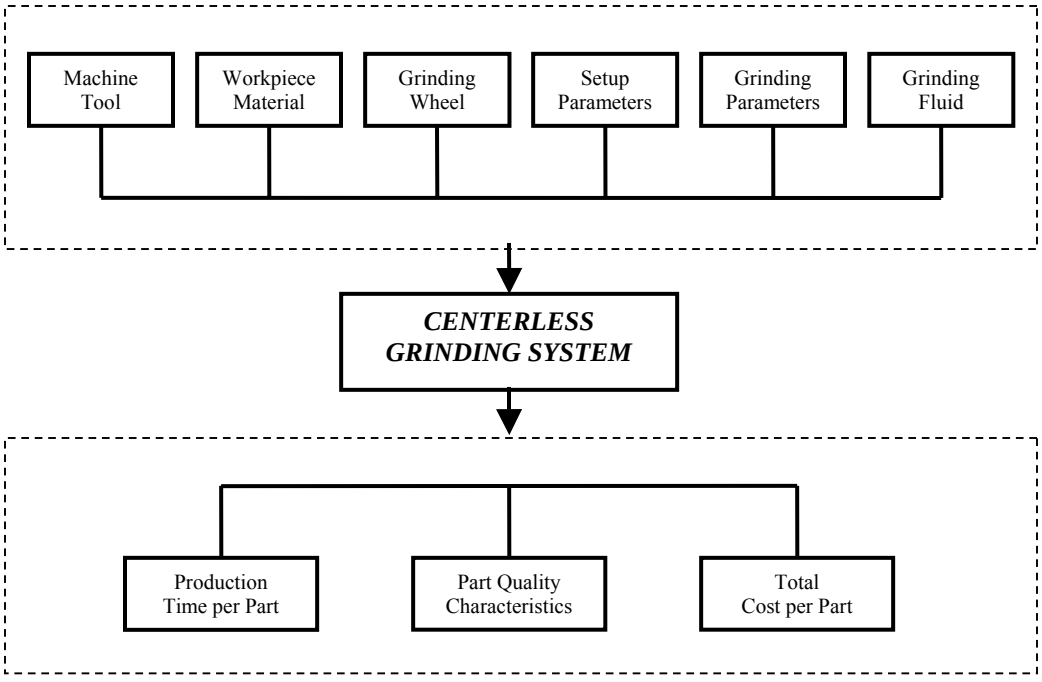

Figure 1.3: Relationship among grinding system parameters and performance metrics

1.2 Problem Statement

The productivity of the grinding operation is defined as the rate at which the components can be produced at the specified quality levels for surface integrity, dimensional accuracy, and surface finish. In the review of academic literature presented in the next chapter, two general approaches were identified for improving the productivity of grinding operations. The first approach consists of optimizing the machine setup conditions to improve the part accuracy. An improvement in the accuracy capability of a machine tool usually results in higher productivity because it enables the use of more aggressive material removal rates while still remaining within the specified tolerance requirements. The second approach consists of off-line grinding parameter optimization using experimental design techniques or on-line grinding parameter optimization using adaptive control to reduce production time with improved feed cycles.

As discussed in the next chapter, a great majority of the research studies conducted to increase the productivity of the centerless grinding process have been focused on the optimization of the machine setup geometry to improve the part dimensional accuracy. For the alloys studied in this thesis, very limited work has been conducted on the optimization of grinding or fluid application parameters as a means to improve the process productivity. In this thesis, two other methods are investigated for improving the performance of this process: (1) economic optimization of grinding process parameters and (2) reduced quantity lubrication using a grinding fluid enhanced with graphite nanoplatelet additives.

1.3. Research Objectives

To investigate the optimization of grinding parameters as a method to improve the process performance in plunge centerless grinding of Inconel 718 and Ti-6Al-4V alloys, the following research objectives are addressed in this study:

- Characterization of the effects of the major grinding parameters on the key process performance responses and part quality characteristics
- Formulation of the constraint-bound feasible operating region
- Development of an algorithm to simulate a typical industrial production sequence and find the optimum grinding parameters within the feasible operating region based on the objective of minimum cost per part

To investigate reduced quantity lubrication using a graphite nanoplatelet-enhanced grinding fluid as a method to improve the process performance in plunge centerless grinding of Inconel 718 and Ti-6Al-4V alloys, the following research objectives are addressed in this study:

- Characterization of the effects of key parameters in graphite nanoplatelet-enhanced grinding fluid application on process performance responses
- Evaluation of the effectiveness of fluid application under different grinding conditions

1.4 Thesis Organization

The contents of this thesis are summarized in Figure 1.4. Chapter 2 discusses the scientific literature on the modeling and optimization of the centerless grinding process. Chapter 3 discusses the experiments conducted to characterize the effects of key grinding parameters on process performance in plunge centerless grinding of Inconel 718 and Ti-6Al-4V aerospace fasteners. Chapter 4 presents the methodology for the economic optimization of process parameters in the fastener grinding operation. Chapter 5 discusses the experiments conducted to evaluate the potential of graphite nanoplatelet-enhanced fluids in reduced quantity lubrication centerless grinding of Inconel 718 and Ti-6Al-4V alloys. Finally, Chapter 6 summarizes the key findings of the study and identifies some future research topics relevant to the optimization of this process.

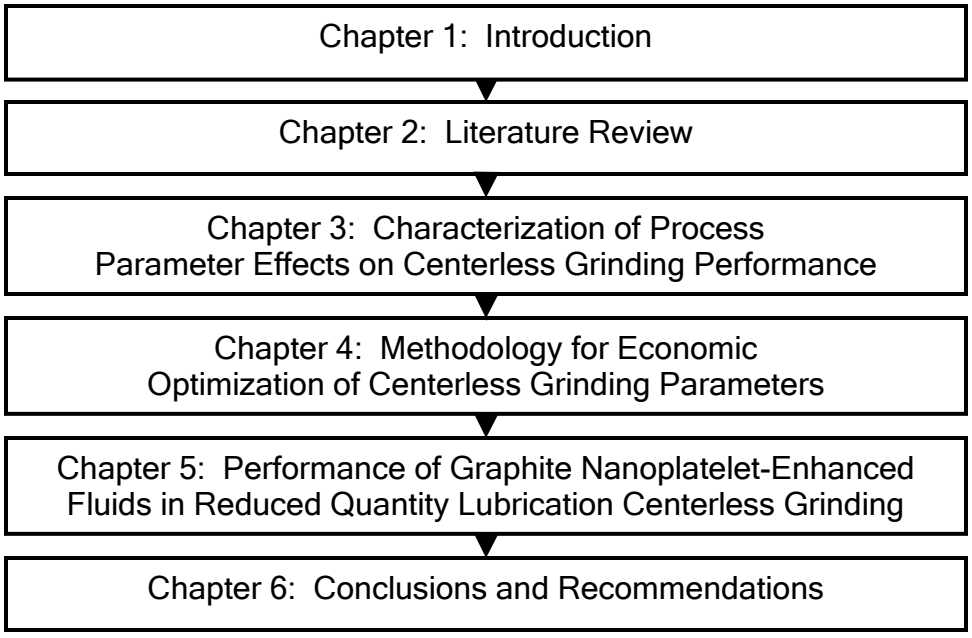

Figure 1.4: Thesis organization flow chart

CHAPTER 2

LITERATURE REVIEW

This chapter presents a review of the scientific literature on the subjects of grinding system modeling and optimization related to the objectives defined for this thesis study in Chapter 1. The literature review is divided into five major sections: (1) overview of grinding process fundamentals, (2) techniques for modeling and optimization of grinding processes, (3) advancements in modeling and optimization of centerless grinding, (4) modeling of heat transfer and optimization of fluid application and (5) summary.

The first section provides an introductory overview of the grinding process fundamentals. The second section presents some of the major techniques utilized in the modeling and optimization of grinding processes. The third section discusses the advancements in the modeling and optimization of process performance for the centerless grinding operation analyzed in this thesis. The fourth section reviews the models developed to study the heat transfer process in grinding and the investigations conducted to optimize the fluid application parameters in various operations. In view of the process optimization strategies and the previous studies conducted for centerless grinding, the last section justifies the tasks undertaken in this study.

2.1 Overview of Grinding Process Fundamentals

Traditional machining operations such as turning, milling, drilling, and grinding are used extensively in the manufacturing industry to remove material from a workpiece and form the final part shape with the desired dimensional characteristics. Unlike the turning, milling, and drilling processes that utilize a cutting tool with a well-defined cutting edge geometry, the grinding process utilizes a cutting tool with a large number of small, multipoint cutting edges in the form of hard abrasive particles bonded to a matrix material. The abrasive particles have a stochastic geometry, orientation, and spatial distribution on the surface of the cutting tool.

The two primary differences between grinding and traditional machining processes (turning, milling, and drilling) are the scale of material chips and the amount of force or energy required to remove a unit volume of material. Traditional machining processes use cutting tools with a deterministic cutting edge geometry that provide positive rake angles and produce more continuous chips with thickness of up to several millimeters, while grinding processes use cutting tools with a stochastic cutting edge geometry that provide high negative rake angles (-45^{o} to -60^{o}) and produce much smaller chip thicknesses (0.25-25 μm). Due to a combination of highly negative rake angles and wear flat areas that develop on each cutting edge with prolonged cutting tool use, the rubbing and ploughing action between the tool and workpiece is much higher for the grinding process, resulting in up to 100 times higher specific energies for material removal in comparison to most traditional machining processes. The mechanics of chip formation in the grinding process are illustrated in Figure 2.1.

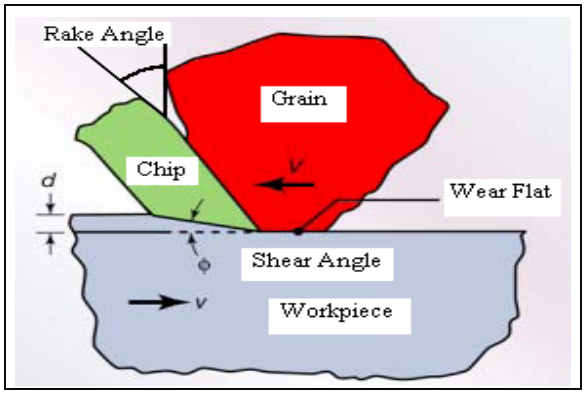

Figure 2.1: Mechanics of chip formation in the grinding process

The mechanics of chip formation in grinding are characterized by the mechanical (sliding, plowing, shearing), chemical (diffusion, adhesion), thermal, and tribological interactions that occur among a large number of multipoint cutting edges and the workpiece material at the tool-workpiece contact interface as described in Figure 2.2. The understanding of these complex interactions is the science behind the process that has evolved over many years from very basic to more complex micro scale models [2-9]. To improve the accuracy of these models, many related studies have also been conducted to characterize the geometry, orientation, and spatial distribution of abrasive grains [10].

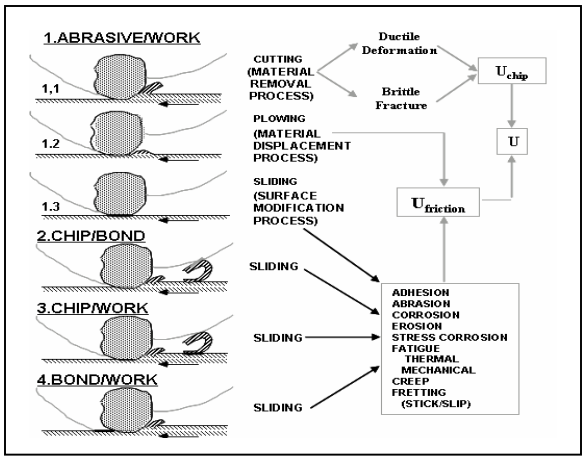

Figure 2.2: Micro scale interactions in abrasive machining [1]

2.2 Techniques for Modeling and Optimization of Grinding Processes

In industrial grinding operations, many system parameters are still commonly selected according to machine operator experience without exploring the technological limits of the process. Researchers have identified two major objectives that must be accomplished in order to define the technological limits of the grinding process and to improve its productivity without compromising part quality: (i) modeling of system parameter effects on key process responses, and (ii) determination of optimum or near-optimum grinding conditions. The major modeling and optimization techniques used to achieve performance gains in grinding as well as in many traditional machining operations are shown in Figure 2.3.

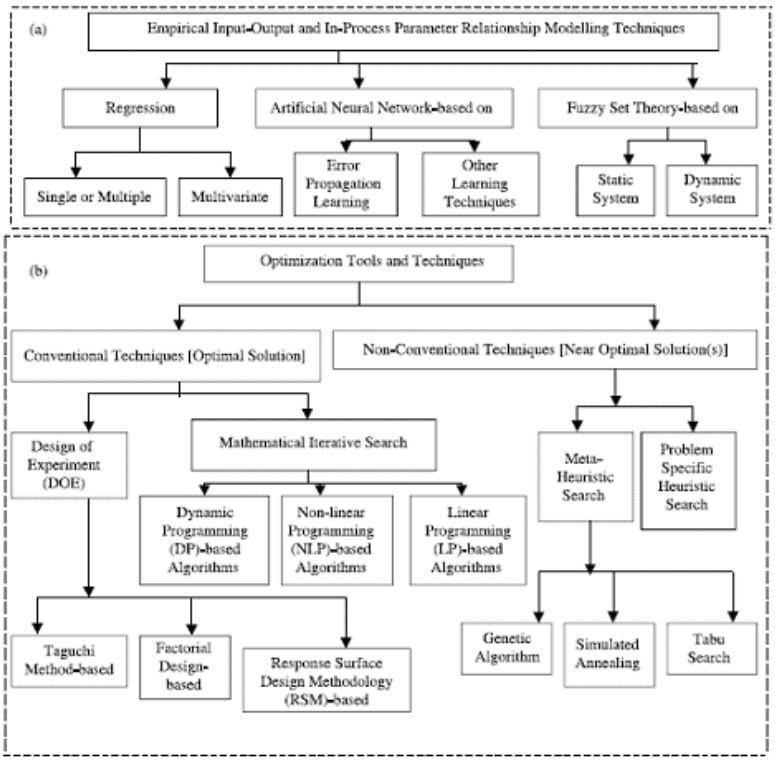

Figure 2.3: Overview of (a) modeling and (b) optimization techniques in machining [24]

Most of the mechanistic micro scale models developed in the early literature for predicting grinding process responses have limited utility as they cannot account for the effects of all the parameters encountered in complex, real world operations. In addition, they utilize variables that can only be measured in a laboratory setting and are therefore not suitable for use on the production floor. To supplement the available mechanistic models, several empirical relations have been developed over the years for different grinding geometries that correlate the micro scale parameters (i.e. chip thickness and length) to the macro scale parameters that can be varied to control the process performance. Hahn and Lindsay [11-14] developed several expressions to quantify the effect of the grain load intensity, chip thickness and length, and cutting edge geometry on the key process responses such as the part surface finish, wheel wear, and grinding energy. Malkin [15] and Shaw [16] developed similar relationships for modeling the effects of grinding parameters on the process responses. Brinksmeier et al. [17] provide a general form for some of the empirical models used to characterize grinding parameter effects on process performance and summarizes the methods for measuring key process responses as shown in Figures 2.4 and 2.5, respectively.

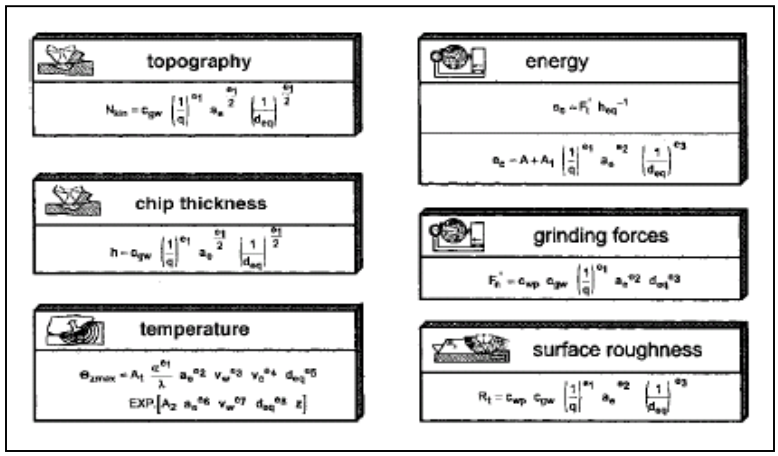

Figure 2.4: Empirical models for grinding process responses [17]

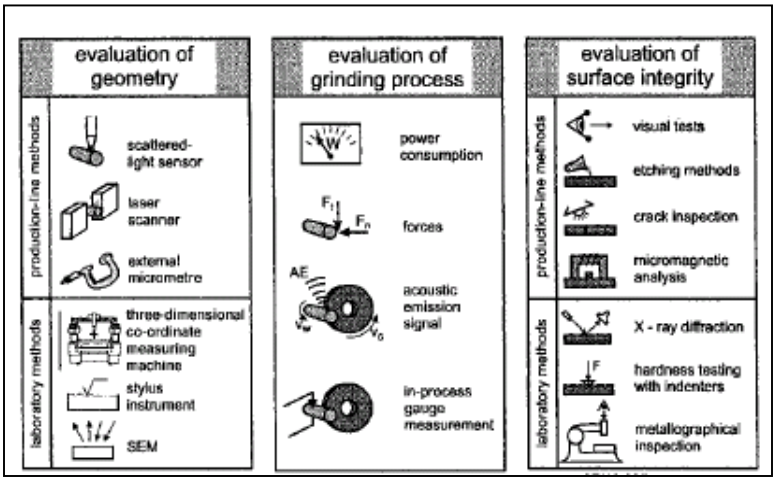

Figure 2.5: Methods for measuring process responses and part quality characteristics [17]

The empirical models developed in these earlier works are still used extensively by researchers and practitioners to predict the key responses in traditional grinding operations such as surface and cylindrical grinding. However, one of the main disadvantages of using the classical empirical relations is that the associated exponents and coefficients must be determined for each combination of workpiece material, grinding wheel, and grinding parameters by controlled experimental tests for different grinding configurations found in practice, which can be a costly and time-consuming procedure. As the diversity and complexity of industrial operations have increased over time, different modeling approaches have been developed and used to predict responses not addressed by the empirical models presented in the early literature.

The major techniques utilized in the modeling of machining process responses consist of statistical regression [18], artificial neural networks [19, 20] and fuzzy set theory [21, 22] as shown in Figure 2.6. All of these techniques rely on experimental design methodology for data collection and analysis. Another more advanced modeling approach that combines the mechanistic models available for different grinding

operations with computational software is finite element analysis (FEA) [23]. Each of these techniques has its advantages and limitations according to factors such as accuracy, process applicability, and computational cost [24], which are summarized in Table 2.1.

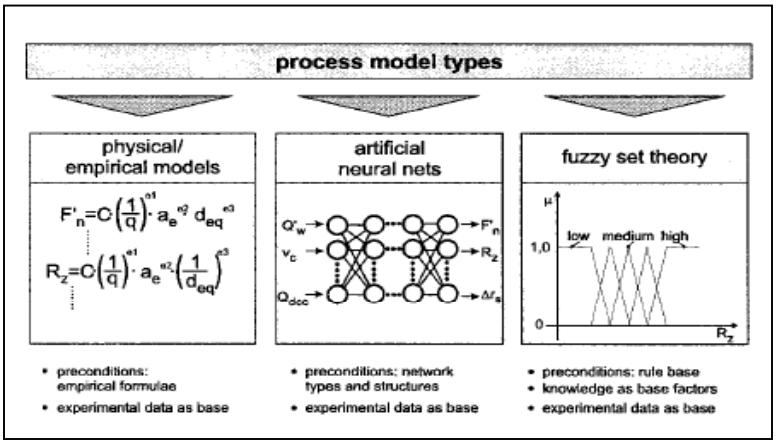

Figure 2.6: Techniques for modeling relationships among variables and process responses [17]

Table 2.1: Advantages and limitations of modeling techniques in machining

Modeling Technique	Advantages	Limitations and Constraints
Statistical Regression (SR)	-Computationally inexpensive -Useful for prediction inference, hypothesis testing, and verification of causal relationships	-Predictor variables must be linearly independent with a normal distribution and constant variance of residuals -Based on prior assumptions about relationships -Not valid outside range of experimental parameters
Artificial Neural Networks (ANN)	-Can handle many variables -Useful for time series prediction, data pattern and sequence recognition, and data clustering -Effective in adaptive machine tool control applications	-No universal rules exist for selection of ANN scheme -Model parameters may not be interpretable for highly non-linear relationships -Requires voluminous data set for sufficient training of network nodes -Finite converge is not guaranteed
Fuzzy Set Theory Models (FST)	-Can handle many variables -Useful when subjective knowledge of process experts is used to define variables and objective functions	-Rules applied using subjective knowledge are not valid when process changes are made at system level
Finite Element Analysis (FEA)	-Provides the most insight into the physical nature of the process	-Experimental verification is limited by accuracy and resolution of current measurement tools

Several optimization techniques have been developed and used in combination with different modeling strategies to determine the best operating conditions in different grinding operations. The conventional optimization techniques attempt to provide a single local optimum solution, while non-conventional techniques attempt to provide an approximate, near-optimum solution. The first category of conventional techniques consists of design of experiments (DOE) approaches [25-30] and classical machining economics [31-33]. The second category of conventional techniques consists of iterative mathematical search methods such as linear programming (LP), non-linear programming (NLP), and dynamic programming (DP) typically used to optimize grinding cycles with intelligent machine tools [34-42]. The non-conventional techniques consist of meta-heuristic search methods such as the genetic algorithm (GA), tabu search (TS), and simulated annealed (SA) [43-45]. Each technique has its advantages and limitations according as summarized in Table 2.2.

Table 2.2: Advantages and limitations of optimization techniques in machining

Optimization Technique	Advantages	Limitations and Constraints
Design of Experiments (TM, RSM)	-Computationally inexpensive -Provide considerable reduction in time and resources needed to identify key effects and to optimize settings	-May not be able to adequately capture higher order and interaction terms -Reliability of results decreases as the number of responses to be optimized increases -Each objective function must be continuously differentiable to obtain closed-form solution
Classical Machining Economics	-Computationally inexpensive -Highlight the effects of process cost and time factors in production to facilitate decision making	-Lack reliable relationships for different process responses measured in production -Derived optimum conditions are often difficult to implement as they violate process constraints
Mathematical Search (LP, NLP, DP)	-Handle large number of variables -Effective for non-linear, multi-objective optimization	-Require continuity of feasible solution space -Intelligent machine tools can be very expensive and inefficient to implement
Meta-Heuristic Search (GA, TS, SA)	-Do not require continuity of feasible solution space -Search direction is probabilistic and very large spaces can be explored	-No universal rules exist for algorithm structure -Finite convergence is not guaranteed -Repeatability of solution using same initial conditions is not guaranteed

In summary, grinding process modeling and optimization has traditionally been accomplished using both conventional and non-conventional methods. The next section discusses how some of the presented techniques have been used in combination with different models to analyze the centerless grinding process studied in this thesis.

2.3 Advancements in Modeling and Optimization of Centerless Grinding

Centerless grinding is a high-precision finishing operation used in the mass production of cylindrical components. In the production environment, it holds several advantages over center-type cylindrical grinding, including shorter machine setup times, shorter part loading and unloading times, and higher part dimensional accuracy and roundness. Despite its advantages over center-type grinding, several problems are still commonly encountered with this operation such as the production of out-of-round workpieces and chatter resulting in dimensional inaccuracies.

Over the years, researchers have identified that the following key aspects of the centerless grinding process limit the productivity and part quality of the operation: (1) workpiece rounding instability, (2) dynamic system instability, and (3) workpiece rotation instability. Workpiece rounding instability or unstable geometric lobing occurs even during dynamically-stable grinding conditions due to random non-uniformities in the workpiece or regulating wheel profile such as flats and lobes that lead to higher roundness errors. Dynamic system instability or work-regenerative chatter vibration related to the dynamic characteristics of the grinding machine causes the workpiece to oscillate in the grinding gap between the wheels and leads to various dimensional errors.

Workpiece rotation instability related to the frictional characteristics of the regulating wheel that controls the cutting pressure and the rotational motion of the workpiece occurs when the workpiece rotational velocity suddenly increases toward the rotational velocity of the grinding wheel. Among these issues, sudden rotational instability is the most important to control as it may lead to part ejection. Most of the studies conducted on the centerless grinding operation have been focused on analyzing the process kinematics and developing simulation models to visualize the surface generation mechanism. The simulation results have been used to identify the optimum setup conditions for stable grinding that minimize instabilities leading to geometric errors.

Some of the earliest attempts to analyze the influence of setup and process parameters on the workpiece roundness instability in centerless grinding were made during the 1940s by Dall [46] and during the 1960s by Rowe et al. [47, 48]. In the study by Rowe et al., a two-dimensional simulation of the workpiece rounding mechanism was carried out for plunge centerless grinding operation considering uniform modes of infeed and several theoretical equations governing the workpiece motion and stability were established. Using these equations, it is possible to determine the setup conditions for stable workpiece rounding. The results obtained by Rowe in the analysis of workpiece rounding are confirmed in contemporary studies conducted by Gurney [49] and Romanov [50]. The key geometric principles of the plunge centerless grinding operation presented by these researchers are illustrated in Figure 2.7. The final out-of-roundness error produced on the workpiece is governed by a large number of setup and process parameters, including the tangent angle β, the work blade angle α', the machining elasticity parameter K, the wheel diameters, the workpiece surface speed, and the infeed.

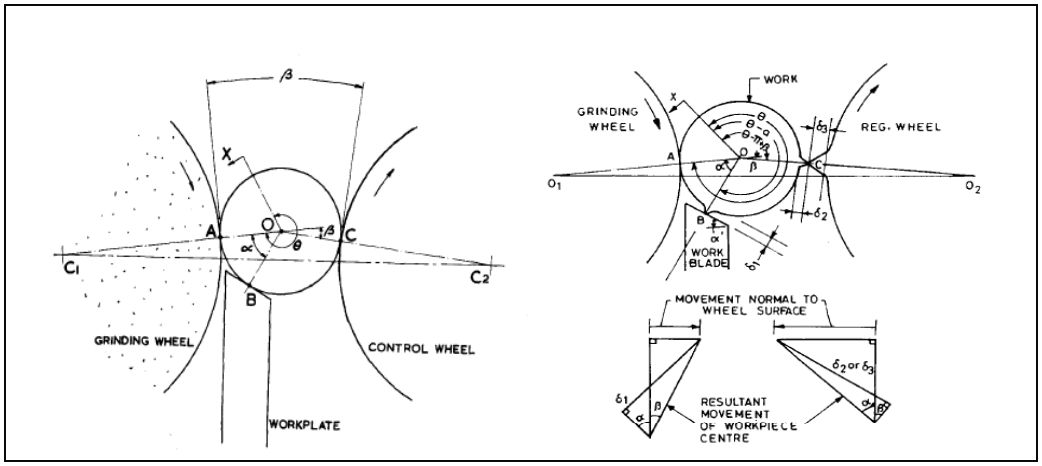

Figure 2.7: Geometric configuration of the plunge centerless grinding operation [48]

Using the parameters defined in Figure 2-7, the rotational motion of the workpiece can be visualized by viewing line OX as the reference vector for its rotational position with respect to the origin line OA. Angles θ, θ-α, and θ-α+β define the contact points of the workpiece with the grinding wheel, the work support blade, and the regulating wheel, respectively. During the surface generation process, an irregularity of magnitude δ_1 at the work blade contact point causes the center of the workpiece to move away from the grinding wheel surface (Figure 2-7). Similarly, an irregularity of magnitude δ_2 at the regulating wheel contact point causes the center of the workpiece to move toward the grinding wheel surface. The basic kinematic equation that describes the instantaneous reduction of the workpiece radius, $r(\theta)$, is given by

$$r(\theta) = K[X(\theta) + \left(\frac{\sin\beta}{\sin(\alpha+\beta)}\right) r(\theta-\alpha) - \left(\frac{\sin\alpha}{\sin(\alpha+\beta)}\right) r(\theta-\pi+\beta) - r(\theta-2\pi)] + r(\theta-2\pi) \quad (2.1)$$

where K is the machining elasticity parameter defined as the ratio of the true depth of cut to the apparent depth of cut and $X(\theta)$ is the set reduction of workpiece radius at position θ. The tangent angle β (radians) is defined according to the other setup parameters as

$$\beta = \sin^{-1}\left(\frac{2h}{D_g + D_w}\right) + \sin^{-1}\left(\frac{2h}{D_r + D_w}\right) \tag{2.2}$$

where h is the height of the workpiece center above the centerline of the grinding and regulating wheels and D_g, D_r, and D_w are the diameters of the grinding wheel, regulating wheel, and workpiece, respectively. Similarly, the expression for the angle α (radians) is defined according to the other geometric parameters as

$$\alpha = \frac{\pi}{2} - \alpha' - \beta\left(1 + \frac{D_g + D_w}{D_r + D_w}\right)^{-1} \tag{2.3}$$

Sample results obtained for the computer simulation of the workpiece cross-sectional profile in plunge centerless grinding using Equation 2.1 assuming a perfectly round part are shown in Figure 2.8 [48]. The simulation can also be repeated for workpieces and regulating wheels with profile variations such as flats and lobes, which shows that such profile deviations usually deteriorate the roundness of the workpiece.

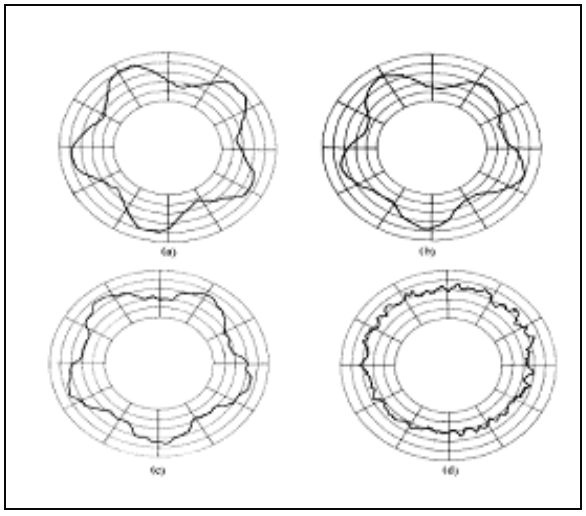

Figure 2.8: Workpiece roundness profiles simulated for different setup conditions [48]

According to the results of the simulation, the most important geometric parameters that determine the final workpiece roundness error are the included tangent angle β and the work blade angle α'. In practical applications, these angles are determined during machine setup by the operator who selects the work blade geometry for a particular workpiece size and sets the height at which the workpiece rests above the centerline of the grinding and regulating wheels (center height h). A typical geometric lobing stability map generated from the model simulations is illustrated in Figure 2.9 [51]. Geometric instability is more likely to occur by using very low work blade angles and by increasing the workpiece center height.

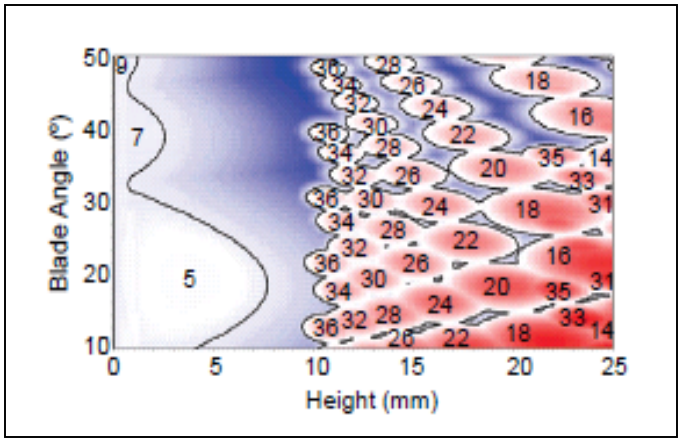

Figure 2.9: Geometric lobing stability map [51]

Many authors subsequently generated their own computer simulations based on the governing equations of motion outlined by Rowe and used methods such as harmonic frequency analysis to identify the setup conditions that minimize the dominant harmonic amplitudes leading to roundness errors [52-54]. In addition, some authors have used design of experiments (DOE) techniques such as response surface methodology (RSM) to find the optimum settings in the infeed and through-feed centerless grinding operation

that minimize the roundness and surface roughness responses [55-57]. In general, it was found that geometric errors and surface roughness increase using higher feeds and regulating wheel speeds.

In summary, the typical setup conditions that can be used to minimize roundness errors and ensure geometric stability as identified by some of these studies are shown in Table 2.3. At the beginning of the operation, it is important for the machine operator to adhere to the suggested setup guidelines to minimize workpiece geometry errors.

Table 2.3: Typical setup conditions for geometric stability in centerless grinding

Geometric Setup Parameter	Optimum Range
Work Blade Angle α'	15-60^o
Tangent Angle β	5-10^o
Workpiece Center Height h	1-10 mm
Regulating Wheel Rotating Frequency N_r	20-60 rpm
Regulating Wheel Tilt Angle ψ	0^o (plunge), 1-3^o (through-feed)
Radial Infeed Distance Δx	50-200 μm

A second factor that limits higher productivity in centerless grinding is the dynamic system instability due to work-regenerative chatter vibration. This phenomenon has been studied by many researchers [58-63] to identify the excitation frequencies that should be avoided to minimize system deflections and how the setup parameters should be selected to suppress the effect of resonant and forced machine vibrations around the wave frequencies where lobing instability may occur (50-100 Hz). A typical chatter stability diagram derived from a dynamic simulation is shown in Figure 2.10 [63]. For a particular center height angle γ that is equivalent to the tangent angle β in Figure 2.7, it is shown that a chatter-free process may be achieved at a relatively low or high work rotational speed N_w.

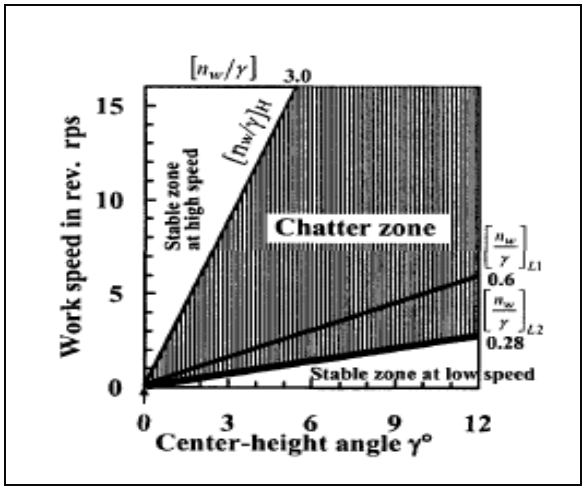

Figure 2.10: Workpiece chatter stability diagram [63]

Another factor that limits higher productivity in centerless grinding is the workpiece rotational instability due to frictional losses at the contact interface between the workpiece and regulating wheel. This phenomenon has been studied and modeled extensively by Hashimoto et al. [64]. The regulating wheel is the system element that controls the rotational movement of the workpiece by exerting a braking moment over the workpiece surface, and many experimental studies have been conducted to understand its frictional characteristics [65-67]. Under certain conditions when high feed velocities or very dull regulating wheels are used, the workpiece rotational movement becomes unstable, resulting in irregular velocity accelerations called “spinners” that can eject the part very suddenly and compromise the safety of the machine operator. In the absence of other instabilities, this phenomenon is the limiting factor to higher productivity since the feed rate establishes the cutting force exerted by the grinding wheel and the required braking moment to control the workpiece rotation. The risk of rotational instability can be reduced by using a regulating wheel with a higher coefficient of friction, using a work blade with a steeper angle, and minimizing the workpiece center height (Figure 2.11).

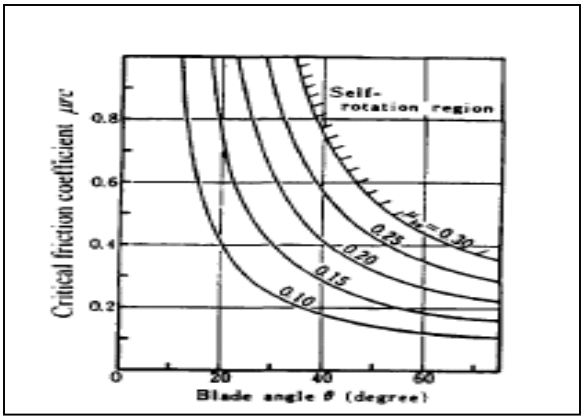

Figure 2.11: Rotational stability as function of the regulating wheel friction coefficient and blade angle [63]

A typical rotational stability map derived using the static torque equilibrium equation derived by Hashimoto et al. is shown in Figure 2.12. The setup conditions for workpiece rotational stability are generally similar to those for minimizing geometric errors.

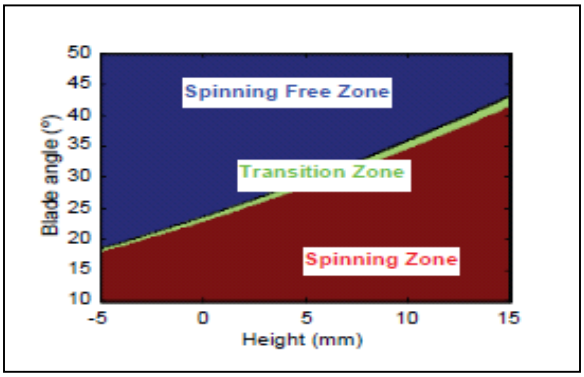

Figure 2.12: Workpiece rotational stability map [51]

Considering the large number of studies conducted on the process kinematics, many researchers view the workpiece motion instabilities as the primary limit to higher levels of productivity and part quality in centerless grinding. To limit workpiece motion instabilities in high material removal rate centerless grinding, a few non-conventional methods have been proposed including grinding below the center position using a

functional work blade [68] and changing the setup configuration during the cutting process to allow a faster correction of the initial roundness error of the workpiece [69]. In comparison to the large number of studies conducted to analyze motion instabilities, the studies on the optimization of grinding parameters have been rather limited [70-72]. In one study, Rowe et al. [71] formulated a basic strategy for process control using limit charts as shown in Figure 2.13 and confirmed that productivity can be increased by using higher wheel speeds and feed rates up to the machine power, grinding burn, or workpiece chatter constraint. In some other analyses of process performance, the cost-optimum specific material removal rate was found to be in the range of 1-6 mm^2/s [70, 72].

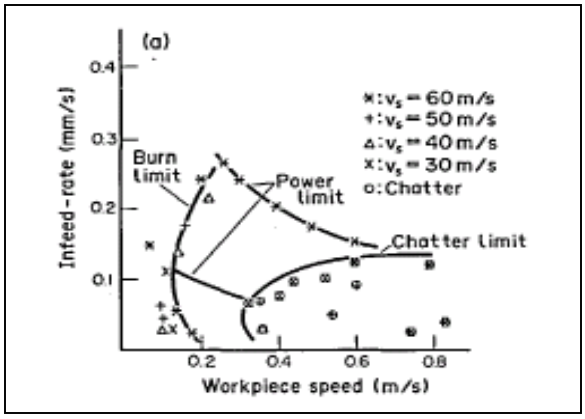

Figure 2.13: Limit chart for material removal rate in centerless grinding [71]

While a comprehensive optimization strategy has yet to be formulated for this complex operation, it is still feasible to explore the variation of grinding parameters as a method to improve productivity while adhering to the guidelines established for workpiece motion stability outlined in these early studies. The next section reviews some heat transfer modeling approaches applicable to different operations and discusses the optimization of fluid application as another method to improve the process performance.

2.4 Heat Transfer Modeling and Optimization of Fluid Application

Grinding is a temperature-dependent machining process that can result in several problems when performed incorrectly, including (1) workpiece thermal damage, (2) unsatisfactory material removal rates, (3) high abrasive costs due to excessive wheel wear and frequent dressing, and (4) ineffective cooling by fluid application. In the grinding contact zone, many randomly shaped and oriented cutting edges cut, plough, and slide against the workpiece surface, generating a large quantity of heat energy that enters the workpiece and adversely affects its surface integrity and final dimensional accuracy.

In the early days of heat transfer analysis, it was found that 60-90% of the grinding energy enters the workpiece material as heat in dry grinding using conventional abrasives [73]. This range of values has been confirmed using various methods to measure the process temperatures such as embedded thermocouples and high-speed IR imaging, which also show that the peak or flash temperatures in the contact zone approach the melting temperature of the workpiece material. A typical workpiece temperature profile measured in a surface grinding operation is shown in Figure 2.14.

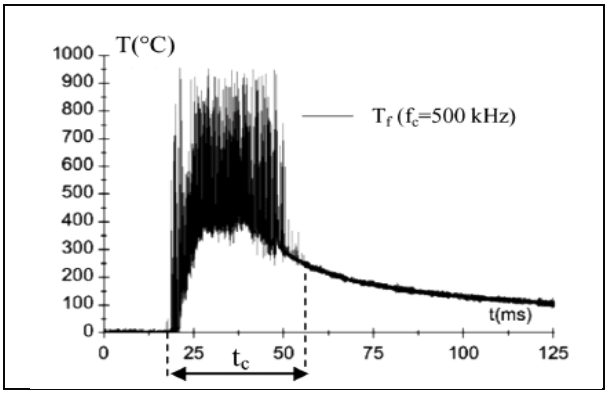

Figure 2.14: Workpiece temperature profile measured by thermocouple [74]

In most grinding operations, the peak temperatures are of extremely short duration since it takes only up to 100 μs for a single grain to move across the length of the contact interface, and they are highly localized on the tips of the microscopic chips removed during the process [75]. The duration of the heat pulse for an individual grain is too short to cause anything more than a very localized plastic deformation along its cutting path. However, the effect of many such pulses averaged over a longer period of heat transfer (1-10 ms) is more significant. In this case, the workpiece continuously absorbs heat pulses just below its surface, which in turn may lead to a significant increase in the workpiece temperature. If a critical temperature is exceeded in the contact zone, different forms of thermal damage may occur that reduce the fatigue life and wear resistance of the component, including burning, metallurgical phase transformations, residual tensile stresses, and micro-cracking [76, 77]. Under very severe grinding conditions with depths of cut exceeding 100 μm, grinding burn is visible and undesirable metallurgical phase transformations in the form of hardened white layers (WL) can also be detected in the workpiece subsurface using SEM as shown in Figure 2.15. The temperature rise in the bulk of the material is only a fraction of the temperature rise at the surface, but it should also be controlled to avoid thermal expansion leading to dimensional inaccuracies [78].

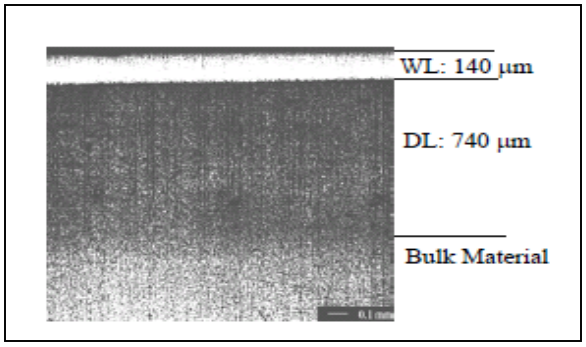

Figure 2.15: Cross-sectional view of ground surface with hardened white layer [79]

The effect of process parameters on grinding temperatures has traditionally been modeled using empirical relations similar to those developed for other process responses. However, these relations provide a very limited understanding of how the magnitude and duration of temperatures affects the surface integrity of the workpiece material for the variety of complex grinding operations found in practice. To supplement the empirical models, numerous theoretical studies have been conducted over the years using heat transfer theory to enhance the understanding of how grinding and fluid application parameters affect heat generation in different operations and how they can be selected to control the quality of ground surfaces.

In most early models, the theoretical grinding temperatures were predicted using the moving heat source analysis developed by Jaeger [80, 81]. According to Jaeger, the temperature rise in the grinding contact zone may be obtained by modeling the heated contact area as a plane band heat source moving at a known velocity along the surface of an adiabatic, semi-infinite solid. It is assumed that the grinding energy is generated over the entire contact zone and that the heat flux is distributed over the surface of a workpiece material with constant thermal properties as shown in Figure 2.16.

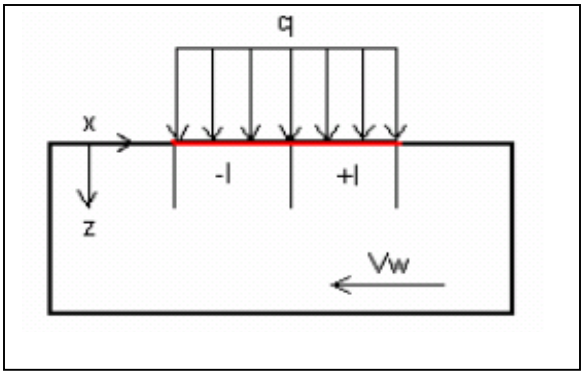

Figure 2.16: Uniformly distributed plane band heat source moving along workpiece surface

Outwater and Shaw [82] used Jaeger's moving heat source analysis to develop a basic heat partitioning model based on a sliding heat source at the shear plane. Ignoring the effects of the forces in the shear plane, Hahn [83] developed a similar sliding model to estimate the heat partition ratio between the workpiece and the abrasive surface in which the primary source of heat is the rubbing between the grain wear flats and the workpiece surface. Considering frictional heating effects, Malkin and Anderson [73, 75] developed a model to predict the grinding zone temperature as a sum of localized heat pulses generated by individual grains in contact with the workpiece surface. Ramanath and Shaw [84] showed that the fraction of heat conducted in the workpiece also depends on the thermal properties of the workpiece and abrasive materials. Makino et al. [85] identified that the actual or dynamic heat source length was two to three times the geometric contact length and that the assumption of a geometric contact length in models results in an overestimation of the intensity of the heat source in the grinding zone. In general, all of these early works identify that the heat energy generated in the grinding process is partitioned into three heat sinks: (i) the grinding wheel, (ii) the workpiece material, and (iii) the grinding chips. In addition, they also confirm that the heat source intensity is a function of the physical interactions between the abrasive grains and workpiece material and their thermal properties. However, the early models neglect the effect of convective cooling by fluid application, which is an additional heat sink that affects process temperatures.

Subsequent analytical and numerical studies have provided a more detailed understanding of the effect of convective cooling on the grinding temperatures and identified methods for controlling workpiece thermal damage. Des Ruisseaux and Zerkle

[86] expanded on Jaeger's moving heat source analysis and developed a model to estimate how the heat energy is partitioned among the grinding wheel, workpiece material, grinding fluid, and grinding chips. In this study, it was found that convective cooling by fluid application in the grinding contact zone is not significant in shallow cut grinding operations using conventional abrasives. In a later study, Howes et al. [87] also found that convective cooling is negligible in shallow cut operations because of the small arc length of the grinding contact zone and confirmed that the primary role of the fluid in this material removal regime is to provide effective lubrication. However, for the creep-feed grinding operation characterized by low workpiece speeds and larger depths of cut, Shafto [88] showed that convective cooling plays a much greater role in removing heat from the contact zone but only up to the boiling temperature of the grinding fluid. Following the onset of fluid film boiling, the workpiece surface temperature may rise up to 1000°C as expected under dry grinding conditions (Figure 2.17) and result in thermal damage. Rowe et al. [89] found that the critical grinding zone temperature for the visible onset of temper colors for many ferrous materials is 450-500°C.

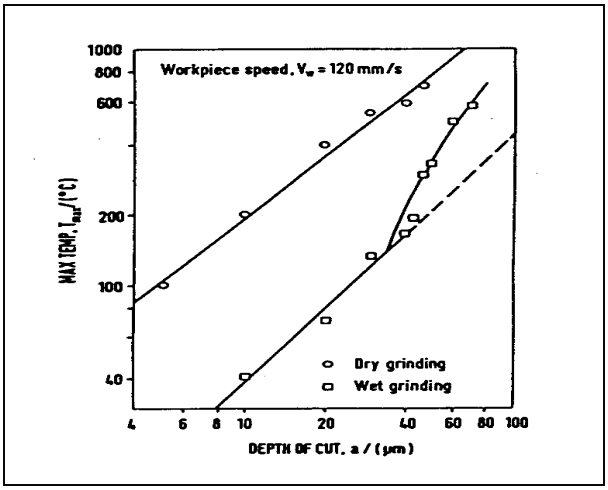

Figure 2.17: Conditions for onset of fluid film boiling [88]

Many related studies have been conducted on the nature of convective cooling by fluid application. Lavine [90] developed a heat transfer model for predicting grinding temperatures based on the convective heat transfer coefficient at the workpiece surface and the fraction of energy entering the workpiece. Jen and Lavine [91-93] also investigated the onset of fluid film boiling to assess the likelihood of thermal damage and the findings were generally in agreement with earlier results. In general, it was found that the effect of convective cooling by fluid application on the grinding zone temperatures is not significant and that grinding fluids do not affect the partition of heat energy in most conventional shallow-cut operations, with creep-feed grinding being the only exception. However, the effect of grinding fluids as lubricants on the grinding zone temperatures is more prominent. As lubricants, grinding fluids reduce the amount of friction at the wheel-workpiece contact interface, which results in a lower energy input.

Using the fluid film boiling temperature as the limit to which the production rate can be increased without incurring thermal damage (~130^{o}C for water-based emulsions and ~300^{o}C for straight cutting oils), the specific material removal rate attainable in shallow-cut grinding using conventional abrasives is typically 5-10 mm^2/s. Yasui and Tsukada [94] first identified a specific material removal rate of ~1 mm^2/s as the limiting value using aluminum oxide grinding wheels. However, in a subsequent study, Kim et al. [95] recognized that Yasui and Tsukada's model overestimates the grinding temperatures by using the geometric contact length instead of the actual contact length and showed that the specific material removal rates can be increased up to 15 mm^2/s and 250 mm^2/s using conventional and CBN grinding wheels, respectively. Due to its higher thermal conductivity, CBN removes a larger fraction of heat in comparison to conventional

abrasives and reduces the grinding temperature by up to 50% over a wide range of depths of cut. Many studies have confirmed the advantages of using CBN grinding wheels, reporting much lower heat energy partition values ranging from 20% to 40% [96, 97].

In addition to analyzing the convective cooling effects of grinding fluids, a few numerical studies were also conducted to assess the feasibility of the constant thermal property assumption for the general solution presented by Jaeger. In general, the temperature gradients in the grinding zone are sufficiently high that the constant thermal property assumption may no longer be justifiable. A finite element analysis of the moving heat source problem with temperature-dependent thermal properties was carried out by Malkin and Isenberg [98] for a plain carbon steel workpiece, which shows that a decrease in the thermal conductivity and an increase in the specific heat with higher temperatures partially offset each other and that the linear constant property solution underestimates the actual grinding zone temperature by only 5% up to a maximum temperature of ~1000^{o}C. However, a finite element analysis of the moving heat source problem with temperature-dependent thermal properties conducted by Malkin and Kovach [99] for a nickel-based superalloy workpiece shows that the general constant property solution overestimates the grinding temperatures by up to 40%. These results confirm that grinding temperatures cannot always be predicted with absolute accuracy using analytical methods and suggest that the actual temperatures also depend on temperature-varying material properties and changes in the material microstructure. The measured temperatures may also deviate from predicted values due to other factors that are often neglected to simplify the heat transfer analysis such as elastic deflections of the grinding system and multiple heat source passes over the nominal contact area.

In the early analyses of heat transfer in grinding, it was confirmed that convective cooling and lubrication of the grinding contact zone by fluid application plays an important role in reducing process temperatures. At the wheel-workpiece contact interface, the grinding fluid performs several important functions, including (1) cooling of the workpiece bulk material, (2) lubrication of the tool-chip interface, (3) removal of grinding swarf from the wheel, and (4) protection of the newly created workpiece surface. In many of these early studies, it was also confirmed that the temperatures in the grinding process can usually be reduced by implementing one of several strategies, such as using softer grinding wheels with high surface porosity at reduced speeds, increasing the dressing frequency to always keep wheels sharp, or increasing the workpiece speed to minimize the duration of contact in the grinding zone and to minimize heat propagation into the workpiece subsurface. However, many of these approaches are counter-productive, resulting in longer production times and higher abrasive consumption costs. As manufacturers attempt to increase productivity with higher material removal rates that result in higher process temperatures and greater wheel wear, more attention has been devoted to optimizing fluid application settings to preserve part quality and improve process performance.

In conventional grinding operations with very small arc contact lengths of less than 1 mm, it has been shown that only about 5% of the total energy input is removed from the contact zone with the chips or by the grinding fluid. The remaining amount of heat energy (up to 95%) is distributed between the grinding wheel and the workpiece, where the exact partition ratio depends on the thermal properties of the two bodies in contact. If conventional abrasive wheels with low thermal conductivity are used, a great

majority of the generated heat will end up in the workpiece, which increases the likelihood of thermal damage. Many studies have been conducted on the effects of different fluid application factors on grinding performance, including fluid composition, fluid delivery parameters (i.e. flow rate, pressure, and temperature), and delivery system components (i.e. nozzle design and placement) to increase the heat removal effectiveness of fluids and avoid wasteful and inefficient fluid application that is still common in many industrial settings. The costs of grinding fluid use, maintenance, and disposal are very significant in machining operations, making up to 17% of the total process costs [100].

In order to improve the removal of heat in the process, a grinding fluid with superior cooling and lubricating properties must be selected for the operation. In most cases, the fluid selected for application is a straight cutting oil or a water-soluble oil. Straight cutting oils are based on derivates of petroleum, vegetable, and marine oil and they are generally known to provide good lubrication. However, cutting oils are poor conductors of heat and they provide very little cooling at the contact interface. In contrast to cutting oils, water-soluble oils are better as coolants but much less effective as lubricants. Despite their poor cooling properties, cutting oils are commonly used in low speed, shallow-cut grinding operations because of their relatively high fluid film boiling temperature and because they ensure a longer wheel life in comparison to soluble oils. Yoon and Krueger [101] confirmed the superiority of cutting oils in an investigation of grinding performance using 45 different types of metalworking fluids by showing that they can achieve up to 10 times higher G-ratios in comparison to water-soluble oils.

Although cutting oils offer several performance advantages, they are very costly to maintain and dispose, and stricter environmental regulations have motivated

researchers to explore different substances that can be used to reduce the quantity of oils in industrial applications. Paul and Chattopadhyay [102] showed that cryogenic cooling by liquid nitrogen lowers the forces and temperatures in grinding of steels more than flood cooling. Shaji and Radhakrishnan [103] and Gopal and Rao [104] showed that solid graphite lubricant can be used to lower the specific energy of the grinding process over a wide range of conditions. Babic et al. [105] showed that soap mist jet cooling can achieve a 20-25% reduction in grinding temperatures over flood cooling using a 5% emulsion. De Silva et al. [106] showed that minimum quantity lubrication (MQL) using an air-oil mixture delivered at a flow rate of 40 mL/h and a velocity of 30 m/s lowers the workpiece surface roughness and induces compressive stresses more than flooding at 8.4 L/min. In a similar MQL study, Shen et al. [107] demonstrated that the application of oils enriched with a high concentration of MoS_2 nanoparticles at 5 mL/min can reduce the grinding forces by up 27% and increase the G-ratio by up to 46% over flood cooling.

After the appropriate fluid has been selected, it must be delivered effectively and in a sufficient quantity to the grinding contact zone. In many grinding operations, machines are equipped with flood cooling systems that deliver large quantities of fluid (5-50 L/min) using bendable plastic nozzles. However, delivering larger quantities of fluid to the grinding zone at higher flow rates using low-pressure nozzles permits more aggressive material removal only up to a certain point before the thermal damage constraint is encountered as shown in the grinding burn limit chart in Figure 2.18 (Zone D). When this operating point is reached, workpiece burn will occur regardless of the quantity of fluid used and fluid application becomes very inefficient.

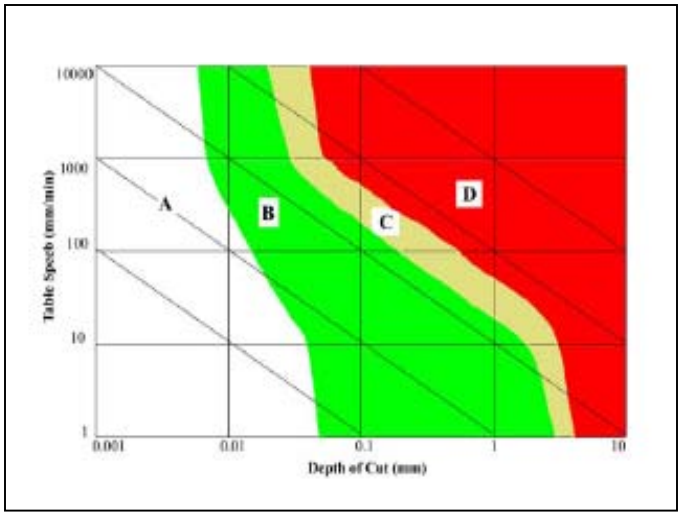

Figure 2.18: Limit chart for grinding burn [108]

(A) Dry (B) 2% emulsion at 11 L/min (C) 2% emulsion at 33 L/min

In many grinding operations using low pressure flood cooling, the useful flow rate of fluid that reaches the grinding zone is only 5-20% of the applied flow rate due to a combination of high fluid jet dispersion and non-coherence outside the contact zone and fluid film boiling inside the contact zone [109, 110]. Fluid jet dispersion outside the contact zone can be mainly attributed to a dense air boundary layer generated by the rotating grinding wheel that deflects the desired path of fluid flow (Figure 2.19).

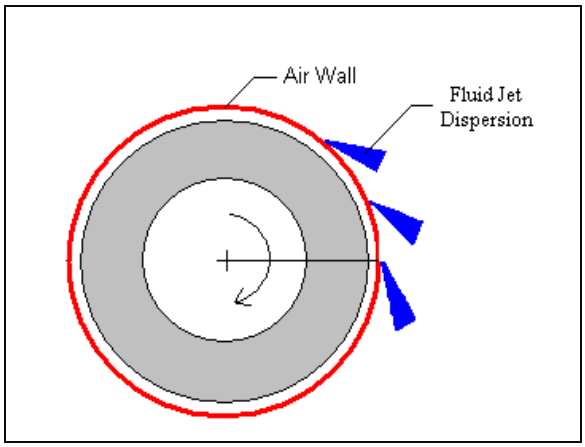

Figure 2.19: Air boundary layer generated by rotating grinding wheel

The velocity distribution of the air boundary layer surrounding the rotating grinding wheel has been characterized by many researchers using Pitot tubes, manometers, and laser doppler anemometry [111-114]. In these studies, it was shown that the boundary layer strength increases with increasing wheel speed and that the effectiveness of fluid delivery decreases as the nozzle is placed further away from the grinding contact zone. A typical tangential air velocity profile measured for the rotating grinding wheel is shown in Figure 2.20.

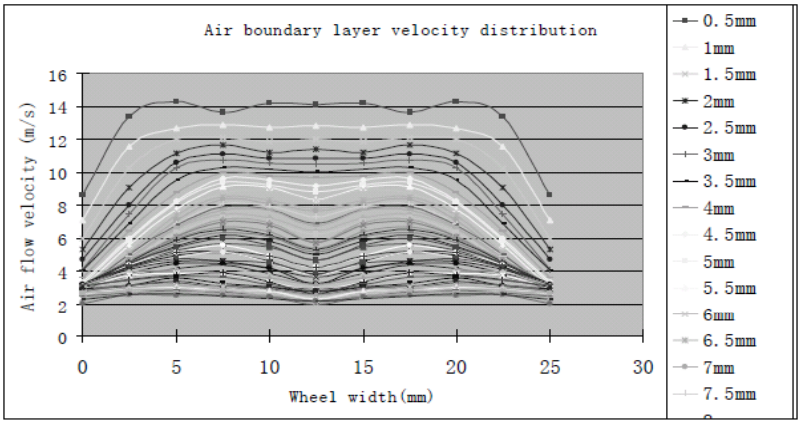

Figure 2.20: Tangential velocity distribution of rotating air boundary layer [114]

Based on the characterization of the air boundary layer surrounding the rotating grinding wheel, it was concluded that the kinetic energy of fluid flow at low jet speeds using conventional nozzles in flood cooling is not sufficient to penetrate the air boundary layer and allow the fluid to reach the grinding zone. Consequently, some researchers have explored different methods to overcome this negative effect. Aside from using higher jet pressures that require fluid pump or nozzle replacement, one practical solution

is to break up the air layer just ahead of the location where the fluid contacts the wheel surface using an air scraper as shown in Figure 2.21.

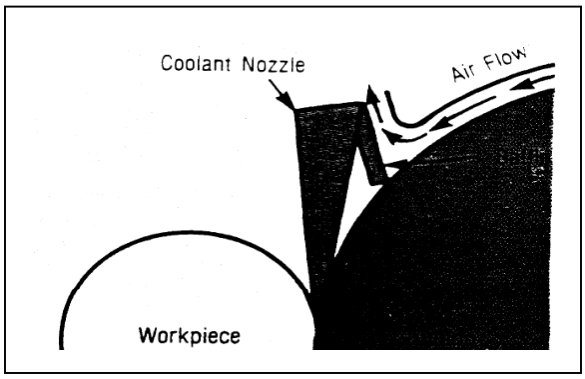

Figure 2.21: Scraper used to break up air boundary layer ahead of the grinding zone

Trmal and Kaliszer [115] and Campbell [116] showed that an air scraper placed very close to the wheel surface just ahead of the contact zone creates a pressure vacuum that is filled by the fluid before it is carried into the grinding zone, allowing the grinding wheel speed to be increased by 20% before the air layer becomes too strong (Figure 2.22).

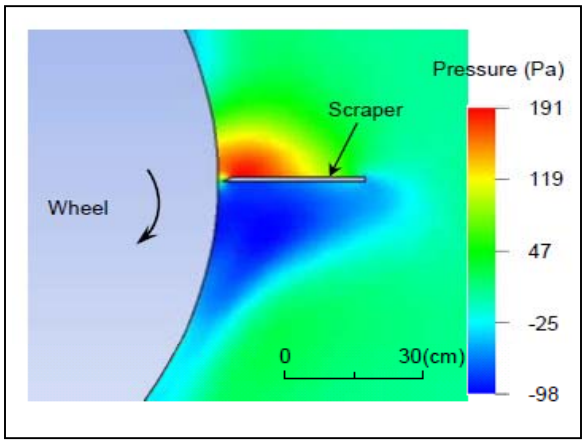

Figure 2.22: CFD simulation of air pressure field around scraper [117]

Based on these studies, Webster [118] suggested that the jet speed should match the wheel speed to ensure that the fluid reaches the contact zone. Also, some studies suggested that fluid delivery can be improved by replacing the click-and-fit plastic nozzles with smooth, straight section nozzles angled at 10-25^{o} with respect to the contact zone as shown in Figure 2.23 [119, 120].

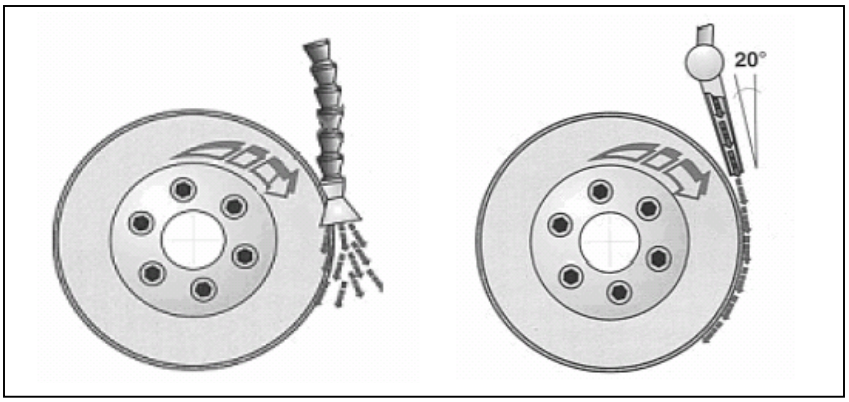

Figure 2.23: Nozzle position for minimum fluid jet dispersion and non-coherence [121]

Considering the aforementioned drawbacks of low pressure flood cooling and its overall inefficiency as method of fluid delivery especially at higher wheel speeds and material removal rates, many researchers have explored different combinations of fluid delivery parameters (i.e. flow rate and pressure) and delivery system components (i.e. nozzle design) to obtain more substantial improvements in process performance. In general, the fluid application methods evaluated in grinding studies as feasible substitutes to the traditional flood cooling consist of manual wheel coating, low-pressure spray misting, and high pressure jet cooling. The superior methods of fluid delivery resulting in lower grinding temperatures outlined by Brinksmeier et al. [122] consist of reduced

quantity lubrication (less than 2L/min) using shoe or spray nozzles and minimum quantity lubrication (50-500 mL/hr) using high pressure jet nozzles (Figure 2.24).

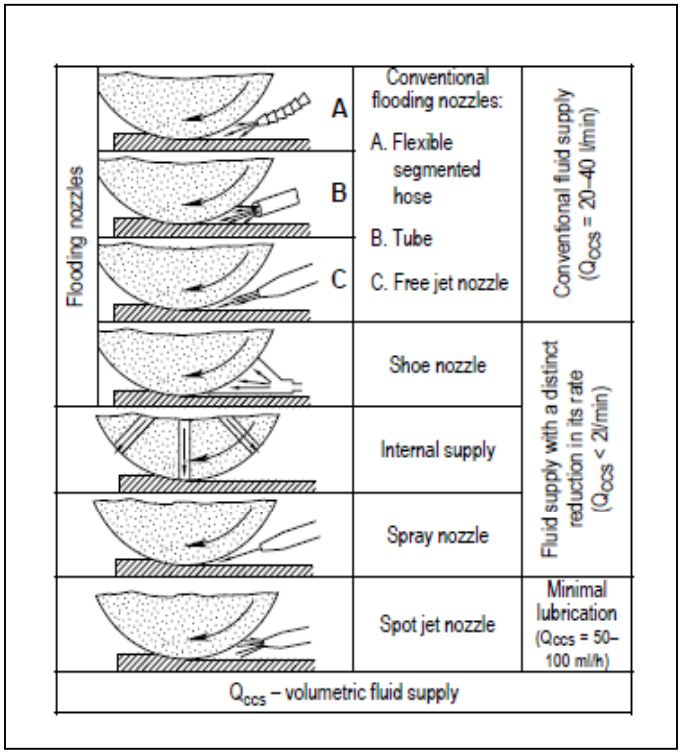

Figure 2.24: Basic methods of grinding fluid delivery [122]

Among all the fluid application methods, manual wheel coating with a brush or similar tool is the easiest and least expensive, but it is limited to small batch production. The disadvantages of this method are intermittent fluid application and poor chip removal. Reduced quantity lubrication using conventional spray or shoe nozzles is a much more effective technique for fluid delivery. A typical shoe nozzle shown in Figure 2.25 ensures a higher fluid velocity at lower pressure than the conventional low pressure jet nozzle due to its interior design features that allow the grinding wheel pores to pick up the fluid and accelerate it to its peripheral velocity before being delivered to the grinding

zone. In addition, the shoe nozzle acts as an air scraper that directs the layer of turbulent air away from the grinding wheel surface. Although shoe nozzles have showed promising results in some grinding operations using CBN wheels [123], they are generally not practical to use when wheel wear is significant [124].

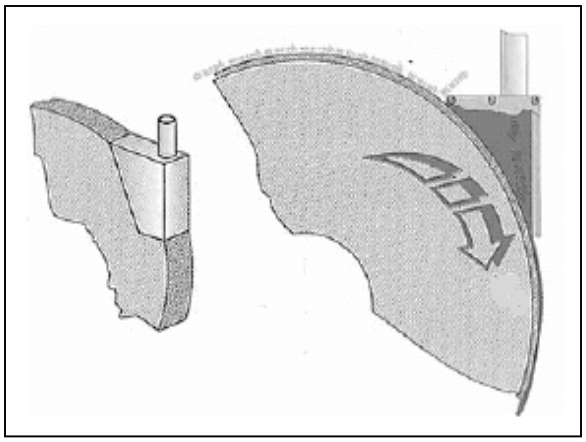

Figure 2.25: Shoe nozzle configuration [121]

A non-conventional technique used in reduced quantity lubrication that has shown promising results is intermittent fluid delivery using an internal supply of nozzles built inside the grinding wheel as shown in Figure 2.26. Some studies have shown that the use of slotted grinding wheels with internal fluid supply reduce the grinding forces by 20-35% and the grinding temperatures by 30-40% over conventional flood cooling [125, 126]. However, this method has not been implemented very frequently in practice due to the high cost of manufacturing slotted wheels and the fixture design that must be used to ensure stable operating conditions.

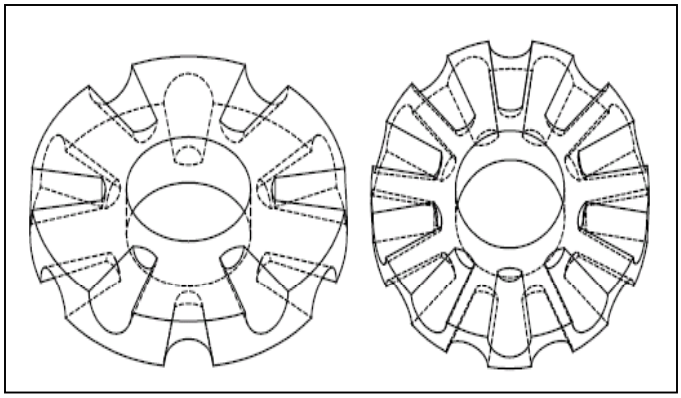

Figure 2.26: Slotted grinding wheels with built-in fluid injectors [121]

High pressure spray misting of vegetable oils and synthetic esters used in minimum quantity lubrication (MQL) demonstrates the best performance over other application methods in processes that use very high wheel speeds [127, 128]. However, one of the main disadvantages of mist application at high pressures (50-3000 psi) is the increased health risk posed to the machine operator by the inhalation of airborne fluid droplets. In typical spray mist applications, the spray droplet diameter varies between 100 and 500 μm. In MQL, the average spray droplet diameter is typically below 100 μm as found in aerosol sprays, but they are lighter and more prone to drifting when subjected to air currents. Therefore, it is very important to optimize nozzle design to ensure coherent, laminar jet flow and minimize the drift of fluid droplets away from the wheel periphery for best process performance [129]. In general, a nozzle should have smooth transitions, a converging geometry, and a fine interior surface finish. Sharp bends or breaks in the fluid supply line cause flow turbulence and poor jet coherence at the nozzle exit. In an extensive CFD study and simulation of the useful fluid flow rate delivered through the pores on the grinding wheel surface for different nozzle geometries shown in Figure 2-27, Morgan et al. [130] found that the converging Rouse design produces the

maximum coherent jet length. This recent study takes into account the findings of an earlier work which shows that the useful flow rate to the grinding zone does not only depend on the nozzle design and wheel speed but also on the surface topography of the grinding wheel [131].

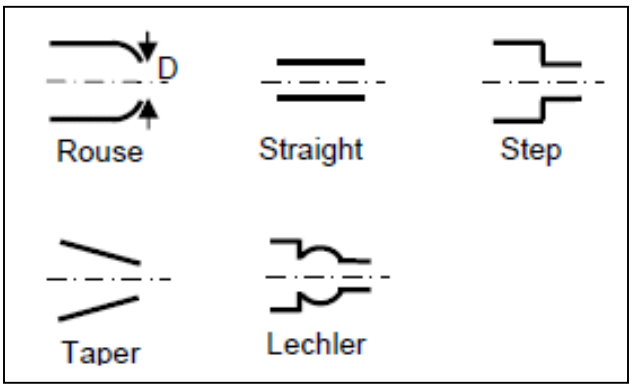

Figure 2.27: Common nozzle design geometries [130]

In summary, this section reviews some of the major works that have been conducted to model heat transfer in grinding and to and study the effects of different fluid application factors on grinding process performance. In this review, several types of fluids and delivery methods were identified as being superior to the traditional flood cooling method for heat removal in different grinding operations. In this thesis, an experimental investigation is conducted to evaluate whether or not the application of a graphite-nanoplatelet enhanced grinding fluid at a reduced flow rate can be used as a viable alternative to high-volume flood cooling to improve the productivity and reduce the costs of the centerless grinding operation for the difficult-to-machine Inconel 718 and Ti-6Al-4V superalloys.

2.5 Summary

Based on this literature review, it can be concluded that centerless grinding is a very complex operation characterized by the interaction of a very large number of variables. For this operation, it is very difficult to determine the effects of each parameter on a particular response and optimize the system settings without incurring large time and capital expenses. In this thesis, two methods for improving centerless grinding productivity are explored: (1) economic optimization of grinding parameters and (2) reduced quantity lubrication using a fluid enhanced with graphite additives.

For the centerless grinding operation, it is very difficult to achieve process control and optimization based on the mechanistic modeling approach. However, to achieve productivity gains, it is not necessary to have models that deliver very high accuracy because such accuracy is seldom reproducible in practice. Instead, the next best alternative is to develop a science-based but practical approach to optimization using a combination of presented optimization strategies. In Chapters 3 and 4, one such systematic approach is presented and carried out to determine the optimum parameters in centerless grinding of two aerospace superalloys.

For many shallow-cut grinding operations including centerless grinding, the traditional flood cooling method is adequate for bulk cooling of the workpiece material and for chip removal, but it is not an efficient or effective method for reducing the grinding zone temperatures. In Chapter 5, an investigation is conducted to assess the feasibility of reduced quantity lubrication centerless grinding using grinding fluids enhanced with graphite nanoplatelets as an alternative to the flood cooling method.

CHAPTER 3

CHARACTERIZATION OF PROCESS PARAMETER EFFECTS ON CENTERLESS GRINDING PERFORMANCE

3.1 Introduction

Inconel 718 and Ti-6Al-4V are desirable for their excellent creep-rupture strength and high corrosion and oxidation resistance in high temperature environments. However, in many traditional grinding operations used to shape these alloys, very limited progress has been made in achieving satisfactory material removal rates. In general, the difficulties encountered when machining these alloys can be attributed to their thermophysical properties as seen in Table 3.1.

Table 3.1: Thermophysical properties of Inconel 718 and Ti-6Al-4V alloys [132]

Material	Density (g/cm^3)	Specific Heat ($J/kg-^oC$)	Thermal Conductivity (W/m-K)	Melting Temperature (^oC)	Hardness (HRC)
Inconel 718	8.19	435	11.4	1260-1335	36
Ti-6Al-4V	4.42	560	7.2	1635-1665	41

As seen in Table 3.1, both alloys are very poor conductors of heat. The heat generated by the grinding action does not dissipate quickly, and as a result, most of the heat remains concentrated on the workpiece surface and produces a negative effect on its surface integrity and dimensional accuracy. Ti-6Al-4V in particular has a tendency to adhere to the grinding wheel and cause rapid wheel loading leading to part thermal damage, and

this effect is more prominent at higher operating temperatures [133]. In addition, the unique work-hardening behavior of these materials also limits higher material removal rates. Inconel 718 work hardens rapidly and makes it tougher for the abrasive grains to remove material efficiently, resulting in rapid wheel dulling. The parameters commonly used for these alloys in the fastener centerless grinding operation with conventional Al_2O_3 and SiC grinding wheels are shown in Table 3.2. For fastener diameters of 4.76-25.4 mm (3/16-1 in.) typically processed in this operation, the corresponding specific material removal rate Q_w' based on the parameters in Table 3.2 is 0.1-1 mm^2/s.

Table 3.2: Process parameters commonly used in centerless grinding of superalloy fasteners

Grinding Wheel Speed (m/s)	Workpiece Speed (m/s)	Feed Rate (μm/s)	Diameter Reduction per Pass (μm)
20-30	0.1-1	10-25	25-1000

For a fixed setup geometry, the final part quality and productivity of the fastener grinding operation (Figure 3.1) is determined by a group of controllable parameters that consist of the grinding wheel composition, dressing conditions, grinding wheel speed, regulating wheel speed, diameter reduction per pass, feed rate, and spark-out time.

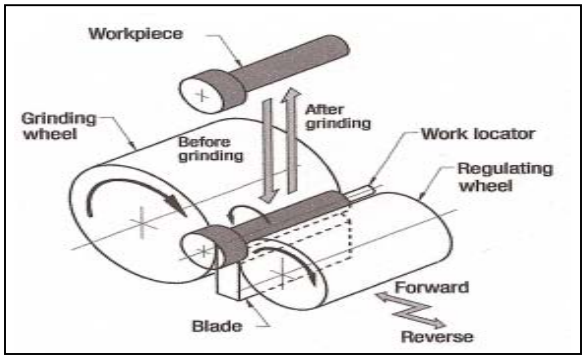

Figure 3.1: Schematic of fastener centerless grinding operation

This chapter presents the experimental studies conducted to characterize the effects of these key process parameters on the productivity and part quality levels in the centerless grinding of Inconel 718 and Ti-6Al-4V superalloy fasteners. The models generated from these experiments are subsequently used to define the process constraint boundaries and to develop an algorithm for finding the optimum grinding conditions (Chapter 4).

3.2 Experimental Procedure

Two sets of experiments (characterization and production run) were conducted to quantify the effects of the key process parameters on the performance of the centerless grinding operation. The full experimental procedure is presented in the ensuing sections.

3.2.1 Characterization Experiment

In order to quantify the effects of the controllable parameters on process performance and part quality characteristics and establish the process constraints, an 8-run orthogonal array characterization experiment was conducted using OA $(8, 2^3, 4^1)$ found in Appendix A with the experimental factors and levels as shown in Table 3.3. Factor interactions were not considered in this experiment. The process parameters of feed rate and spark-out time were not included as controllable experimental factors because they could not be set precisely on the manual feed centerless grinder used in this study. The order of experimental trials was randomized and each trial was performed twice to obtain 16 data points for each workpiece material. The grinding wheels were

redressed with a Vertex V2-O single point diamond for a rough pass operation before each trial using a dressing traverse rate of 4.23 mm/s and a depth of dress per pass of 25.4 μm maintain the same wheel surface condition. For all finish pass operations, the dressing traverse rate and depth of dress per pass were reduced by a factor of 2. The grinding fluid used in all the experiments was Castrol ALMACUT 7210 cutting oil and it was applied to the grinding zone using low pressure flooding at a flow rate of ~5 L/min. The setup parameters were selected according to the guidelines for workpiece stability presented earlier in Table 2.3 and held constant for all the experimental trials.

Table 3.3: *OA* ($8, 2^3, 4^1$) for characterization experiment

Trial	Grinding Wheel Speed (m/s)	Regulating Wheel Speed (m/min)	Diameter Reduction per Pass (μm)	Grinding Wheel Material (A or B)
1	19.1	13.4	152.4	A
2	19.1	24.5	76.2	B
3	23.9	13.4	152.4	B
4	23.9	24.5	76.2	A
5	28.7	13.4	76.2	A
6	28.7	24.5	152.4	B
7	33.5	13.4	76.2	B
8	33.5	24.5	152.4	A

In Table 3.3, wheel material A denotes the grinding wheels commonly used for Inconel 718 and Ti-6Al-4V, while material B denotes new grinding wheels selected for each workpiece material according to a literature survey and wheel manufacturer recommendations promising increased wheel life between dressings and higher material removal rates. The key properties of the wheels used in the experiment are shown in Table 3.4. The summary of grinding wheel recommendations is provided in Appendix B.

Table 3.4: Grinding wheel properties

Workpiece Material	Wheel Symbol	Abrasive Material	Wheel Dimensions (Diameter x Width)	Manufacturer Code
Inconel 718	A	Al_2O_3	609.6 mm x 63.5 mm	2A80-O4-V
Inconel 718	B	Al_2O_3 (SG)	609.6 mm x 63.5 mm	3SGP80-O6-VH
Ti-6Al-4V	A	SiC	609.6 mm x 63.5 mm	GC120-N+7-V
Ti-6Al-4V	B	SiC	609.6 mm x 63.5 mm	74C120-O6-VK

The grinding wheel speed values were selected not to exceed the maximum allowable wheel speed established by the wheel manufacturer (33.5 m/s) and the regulating wheel speed values were selected at two lower settings (13.4 m/min, 24.5 m/min) to minimize the risk of workpiece chatter (Table 2.3). The values of diameter reduction per pass were selected based on common practices in a rough pass and finish pass operation.

The responses measured in the experiment were the grinding power and the arithmetic average surface roughness for headed cylindrical blanks with a 7.94 mm (5/16 in.) diameter and 63.5 mm (2.5 in.) overall length. The key dimensional tolerances for the headed cylindrical blank (in.) used in the experiment are illustrated in Figure 3.2.

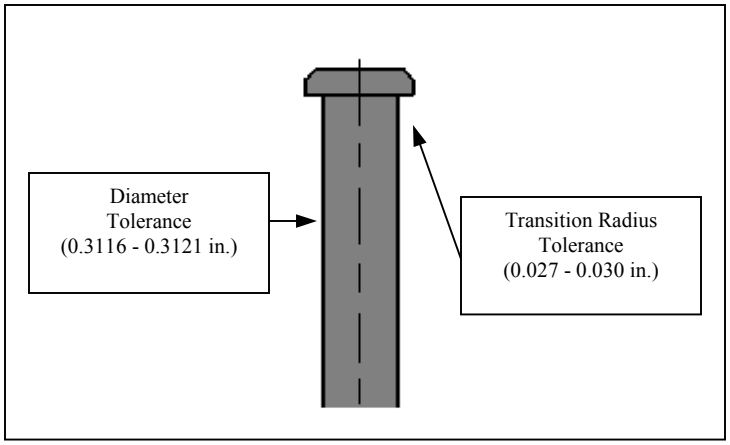

Figure 3.2: Dimensional tolerances for headed cylindrical blank

3.2.2 Production Run Experiment

To evaluate process trends, to compare grinding wheel performance, and to develop empirical wheel wear relations, a set of production runs was conducted for each workpiece material using various combinations of grinding parameters. The process responses of grinding power, surface roughness, and part dimensions were recorded in time as outlined in Figure 3.3.

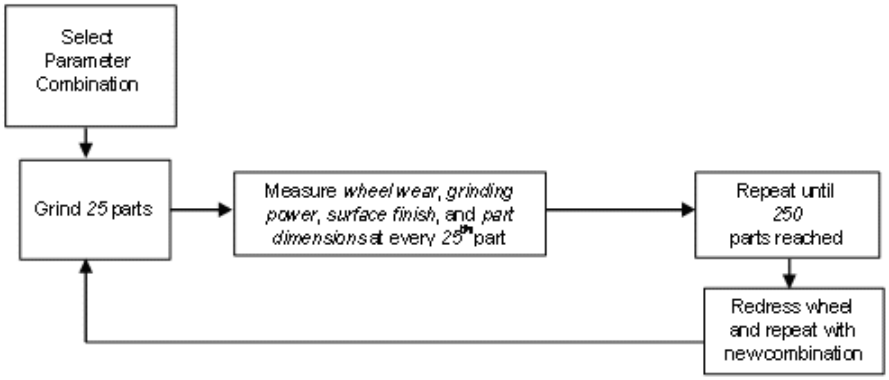

Figure 3.3: Flow chart of production run experiment

For the headed blank, a total of six production runs were conducted for each workpiece material. Each run was conducted using a different parameter combination consisting of the grinding wheel speed, stock removed per pass, feed rate, and wheel material shown in Tables 3.5 and 3.6 for Inconel 718 and Ti-6Al-4V, respectively. In Tables 3.5 and 3.6, the dressing overlap ratio is defined as the effective cutting width of the dressing diamond w_d (~1 mm) divided by the dressing lead s_d. Lower ratios (1-3) yield a rougher wheel surface while higher ratios (4-6) yield a smoother wheel surface during the dressing operation.

Table 3.5: Dressing and grinding parameters for Inconel 718 production runs

Production Run	Number of Parts	Dressing Overlap Ratio	Grinding Wheel Speed (m/s)	Stock Removed per Pass (μm)	Feed Rate (μm/s)	Wheel Material (A or B)
1-Rough	250	2.36	33.5	127	39.1	Cincinnati (A)
2-Rough	250	2.36	19.1	127	39.1	Cincinnati (A)
3-Finish	500	4.72	33.5	63.5	19.5	Cincinnati (A)
4-Rough	250	2.36	33.5	127	39.1	Norton SG (B)
5-Rough	250	2.36	19.1	127	39.1	Norton SG (B)
6-Finish	500	4.72	33.5	63.5	19.5	Norton SG (B)

Table 3.6: Dressing and grinding parameters for Ti-6Al-4V production runs

Production Run	Number of Parts	Dressing Overlap Ratio	Grinding Wheel Speed (m/s)	Stock Removed per Pass (μm)	Feed Rate (μm/s)	Wheel Material (A or B)
1-Rough	250	2.36	33.5	127	39.1	Kinik (A)
2-Rough	250	2.36	19.1	127	39.1	Kinik (A)
3-Finish	500	4.72	14.4	63.5	19.5	Kinik (A)
4-Rough	250	2.36	33.5	127	39.1	Norton (B)
5-Rough	250	2.36	19.1	127	39.1	Norton (B)
6-Finish	500	4.72	14.4	63.5	19.5	Norton (B)

The wheel wear characteristics measured during each production run were defined by the part diameter error (DE) and transition radius error (TRE). The error for each dimension (Figure 3.2) was quantified as the cumulative deviation from the target dimension after grinding a specified number of parts.

3.3 Experimental Setup and Measurements

The centerless grinder used in this study was the Cincinnati OM-2 model with a 15 hp (11.25 kW) grinding wheel spindle motor. The grinding cycle power was

measured by a Load Controls UPC model power meter connected to the wheel spindle motor to capture its voltage signal, which was relayed to a PC via a data acquisition board for analysis in LabView software as shown in Figure 3.4. A sample 10-Hz spindle motor voltage signal acquired over a 5-s period at a sampling rate of 2 kHz for a Ti-6Al-4V rough pass conducted using a grinding wheel speed of 19.1 m/s and regulating wheel speed of 13.4 m/min is shown in Figure 3.5.

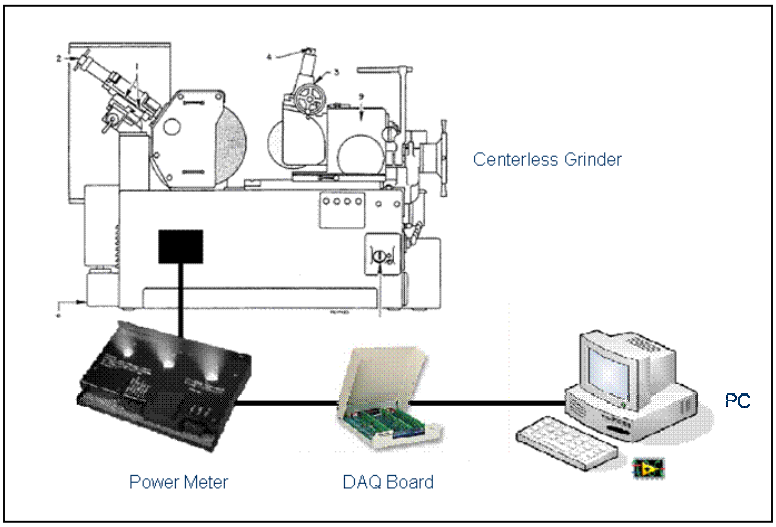

Figure 3.4: Schematic of experimental setup for measuring grinding power

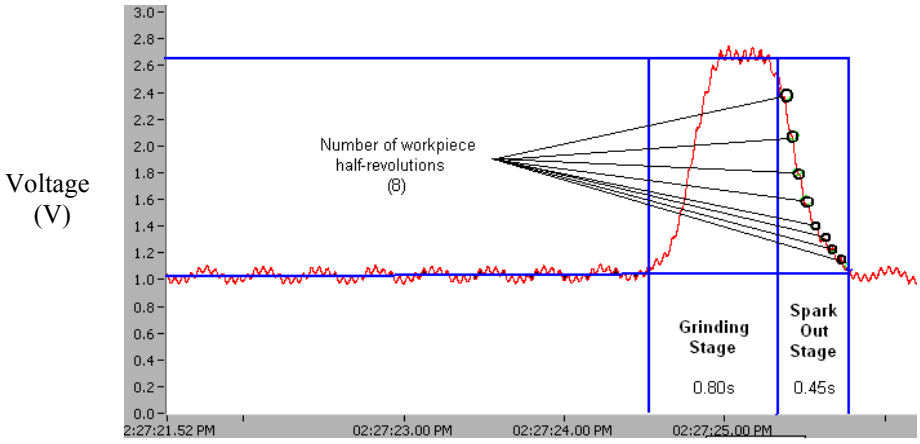

Figure 3.5: Sample grinding cycle voltage signal for Ti-6Al-4V grinding pass

The arithmetic average surface roughness for each part was measured using the Zygo New View 200 optical profilometer by rotating the part and taking 5 equidistant spot measurements along its ground length. The 5 measurements were averaged to obtain a representative surface roughness for the part. A sample image is shown in Figure 3.6.

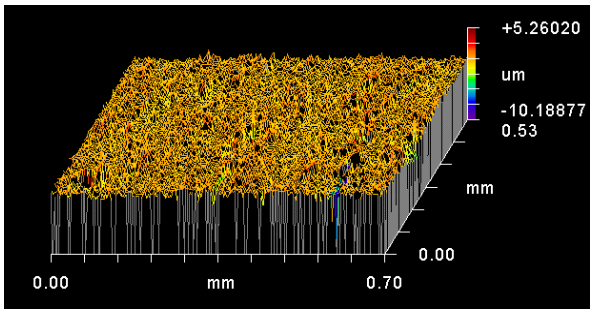

Figure 3.6: Sample image for surface roughness measurement

The dimensions measured for each part were the diameter and the transition radius. The diameter was measured using a micrometer and its deviation from the target dimension was monitored to quantify wheel radial wear. The transition radius was measured using the Mitutoyo toolmaker's microscope and its deviation from the target dimension was monitored to quantify wheel edge wear. A sample image for a transition radius measurement using the Mitutoyo toolmaker's microscope is shown in Figure 3.7.

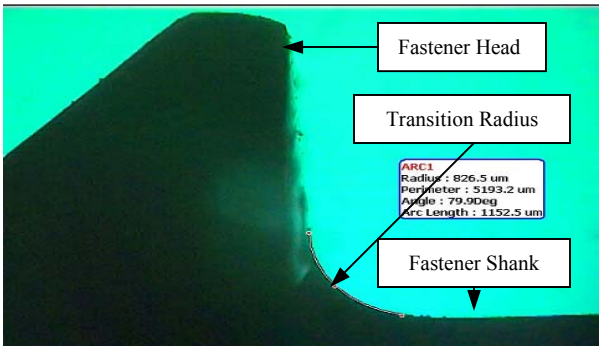

Figure 3.7: Sample image for transition radius measurement

After reviewing the scientific literature on the techniques used to measure grinding wheel topography, including acoustic emission, stylus profilometry, imprints, thermal pulsing, and scanning electron microscopy, the imprint technique was adopted due to its reasonable accuracy and ease of replication [134]. The selected imprint material was lead because it is relatively soft compared to other metals and sufficiently reflective for optical analysis. To prepare the imprint samples, 1.59 mm (1/16 in.) thin lead strips were polished successively using 300, 600, and 1200-grit silicon carbide paper for a high-quality finish. The wheel surface imprints were taken by manually pressing the polished lead strip across a section of the wheel periphery.

A sample image obtained using the Zygo New View 200 optical profilometer for the wheel surface imprinted on the lead sheet is illustrated in Figure 3.8a. This figure shows a top view of the imprinted abrasive grains for a 0.70 mm x 0.53 mm section of the Kinik Ti-6Al-4V grinding wheel surface. A similar SEM image of abrasive grains on the wheel surface provided in a manufacturer's catalogue is shown in Figure 3.8b. By comparison, it can be seen that the imprint technique provides a reasonably good representation of the wheel surface condition.

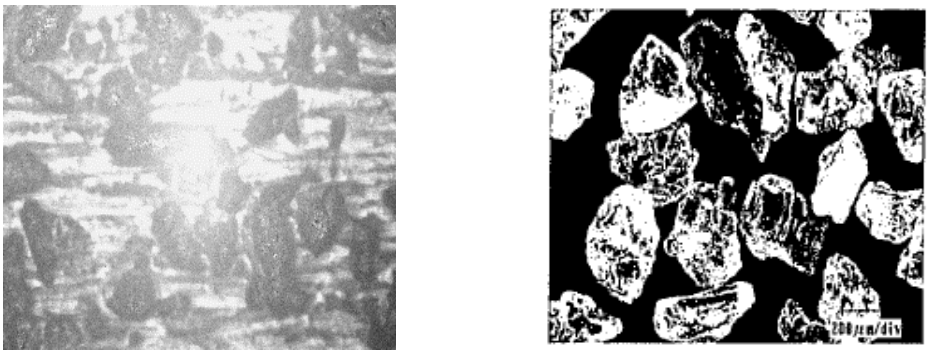

(a) Zygo 10x (Kinik 120-grit) (b) Manufacturer catalogue (Noritake 60-grit)

Figure 3.8: Sample grinding wheel surface images

3.4 Results and Discussion

3.4.1 Characterization Experiment – S/N Ratio Analysis

A detailed summary of the characterization experiment data is found in Appendix C. The data obtained for the two grinding passes conducted under each trial condition is shown in Tables 3.7 and 3.8 for Inconel 718 and Ti-6Al-4V, respectively.

Table 3.7: Characterization experiment data summary (Inconel 718)

Grinding Wheel Speed (m/s)	Regulating Wheel Speed (m/min)	Stock Removed per Pass (μm)	Grinding Wheel Material	Grinding Power (W)	Surface Roughness (μm)
19.1	13.4	152.4	A	1106, 1116	2.10, 2.03
23.9	24.5	76.2	A	1038, 846	1.97, 1.90
28.7	13.4	76.2	A	658, 721	1.37, 1.35
33.5	24.5	152.4	A	1586, 1545	2.45, 2.33
19.1	24.5	76.2	B	647, 667	1.84, 1.95
23.9	13.4	152.4	B	789, 802	1.70, 1.90
28.7	24.5	152.4	B	1477, 1131	2.67, 2.47
33.5	13.4	76.2	B	681, 631	1.42, 1.32

Table 3.8: Characterization experiment data summary (Ti-6Al-4V)

Grinding Wheel Speed (m/s)	Regulating Wheel Speed (m/min)	Stock Removed per Pass (μm)	Grinding Wheel Material	Grinding Power (W)	Surface Roughness (μm)
19.1	13.4	152.4	0	603, 1071	1.86, 2.08
23.9	24.5	76.2	0	588, 617	1.83, 1.75
28.7	13.4	76.2	0	857, 621	1.26, 1.35
33.5	24.5	152.4	0	1263, 1403	2.41, 2.45
19.1	24.5	76.2	1	659, 748	1.65, 1.79
23.9	13.4	152.4	1	952, 1032	1.55, 1.60
28.7	24.5	152.4	1	1430, 1335	2.27, 2.12
33.5	13.4	76.2	1	869, 829	1.22, 1.09

For this experiment, a statistical analysis of data was conducted using Taguchi's Signal-to-Noise (S/N) ratios to quantify the contribution of each factor to the measured responses of grinding power and surface roughness and to identify the optimum level for each factor that minimizes their value. In any grinding operation, it is desirable to minimize both the grinding power and surface roughness in order to reduce the risk of thermal damage and ensure a high-quality finish. The S/N ratio parameter η defined according to the-lower-the-better criterion is given by

$$\eta = -10\log\left[\frac{1}{n}\sum_{i=1}^{n} y_i^{\,2}\right] \tag{3.1}$$

where y_i is the observed data for the n^{th} trial and n is the number of trials. The experimental factors and levels are shown in Table 3.9. Factor interactions were not considered in the analysis of this experiment.

Table 3.9: Characterization experiment factors and their levels

Experimental Factor	Level 1	Level 2	Level 3	Level 4
Grinding Wheel Speed (m/s)	19.1	23.9	28.7	33.5
Regulating Wheel Speed (m/min)	13.4	24.5	---	---
Stock Removed per Pass (μm)	76.2	152.4	---	---
Grinding Wheel Material	A	B	---	---

The results of the S/N ratio analysis are tabulated in Appendix D and the corresponding main effect plots for the grinding power are shown in Figures 3.9 and 3.10 for Inconel 718 and Ti-6Al-4V, respectively.

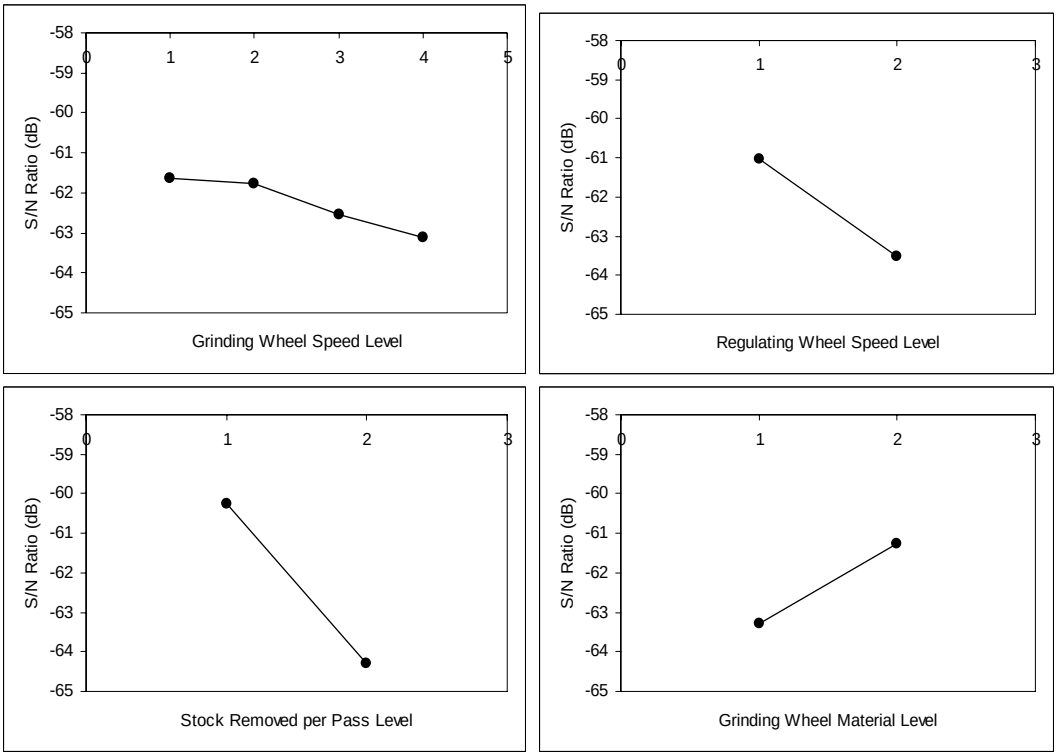

Figure 3.9: Effects of process parameters on grinding power response (Inconel 718)

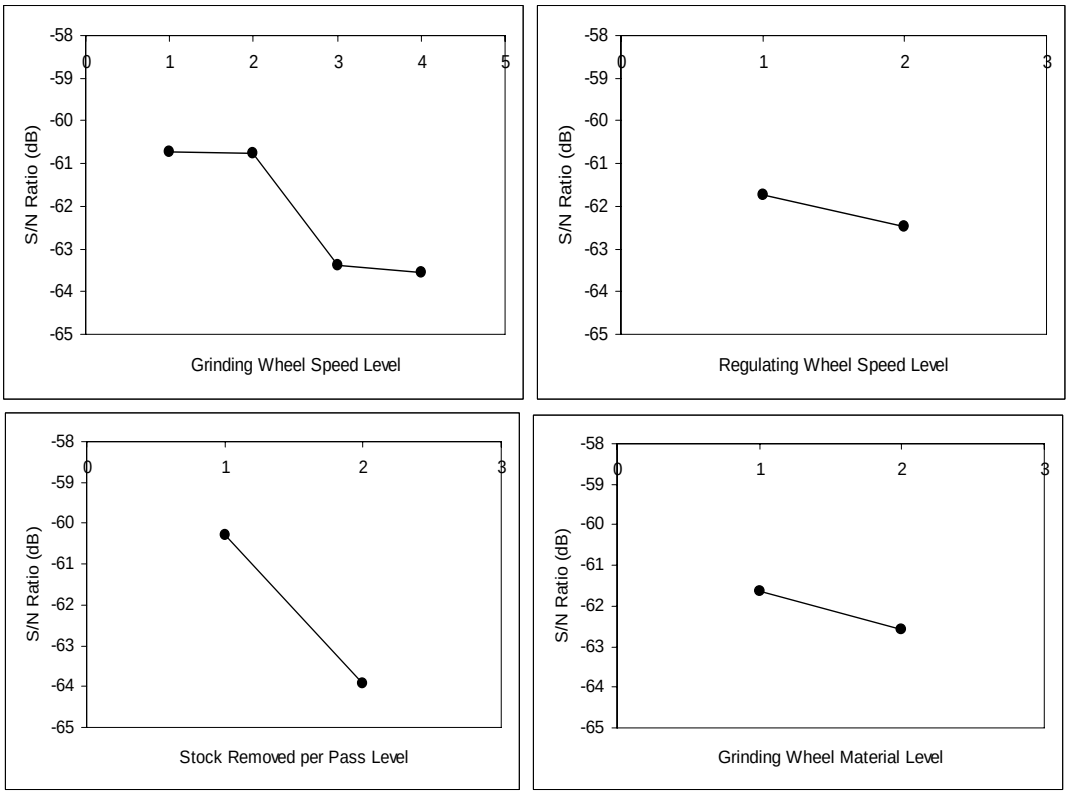

Figure 3.10: Effects of process parameters on grinding power response (Ti-6Al-4V)

From the S/N tables given in Appendix D, the contribution of each process parameter to the grinding power response is shown in Table 3.10 for each workpiece material.

Table 3.10: Contribution of process parameters to the grinding power response

Workpiece Material	Grinding Wheel Speed	Regulating Wheel Speed	Stock Removed per Pass	Grinding Wheel Material
Inconel 718	14.8%	24.9%	40.3%	20.0%
Ti-6Al-4V	34.7%	9.0%	44.7%	11.5%

For Inconel 718, the amount of stock removed per pass had the greatest effect on the grinding power, followed by the regulating wheel speed, the grinding wheel material, and the grinding wheel speed. For Ti-6Al-4V, the amount of stock removed per pass had the greatest effect on the grinding power, followed by the grinding wheel speed, the grinding wheel material, and the regulating wheel speed. In order to minimize the grinding power, the grinding parameters should be set according to the recommendations in Table 3.11.

Table 3.11: Optimum parameter settings for minimum grinding power

Workpiece Material	Grinding Wheel Speed (m/s)	Regulating Wheel Speed (m/min)	Stock Removed per Pass (μm)	Grinding Wheel Material
Inconel 718	19.1	13.4	76.2	B
Ti-6Al-4V	19.1	13.4	76.2	A

For Inconel 718, the results shown in Table 3.11 suggest that the highly friable ceramic sol-gel (SG) Norton grinding wheel (B) can remove material more efficiently than the Cincinnati fused aluminum oxide wheel (A). This conclusion is supported by the specific grinding energy (SGE) plot for Inconel 718 shown in Figure 3.11 for each

wheel used in the characterization experiment, which shows that the Norton SG wheel (B) consumes approximately 20-30% less energy at higher material removal rates.

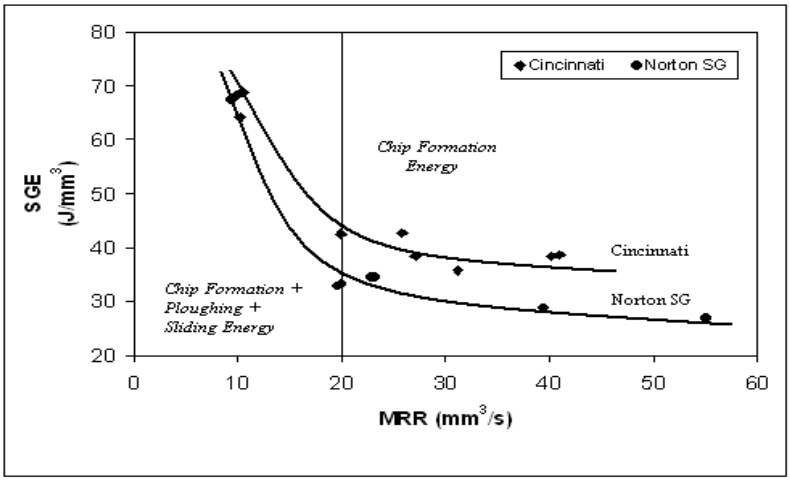

Figure 3.11: Specific grinding energy vs. material removal rate (Inconel 718)

The same specific grinding energy plot is shown for Ti-6Al-4V in Figure 3.12. For Ti-6Al-4V, the Norton and the Kinik wheels use comparable amounts of energy with the Kinik wheel acting a little softer under more aggressive cutting conditions.

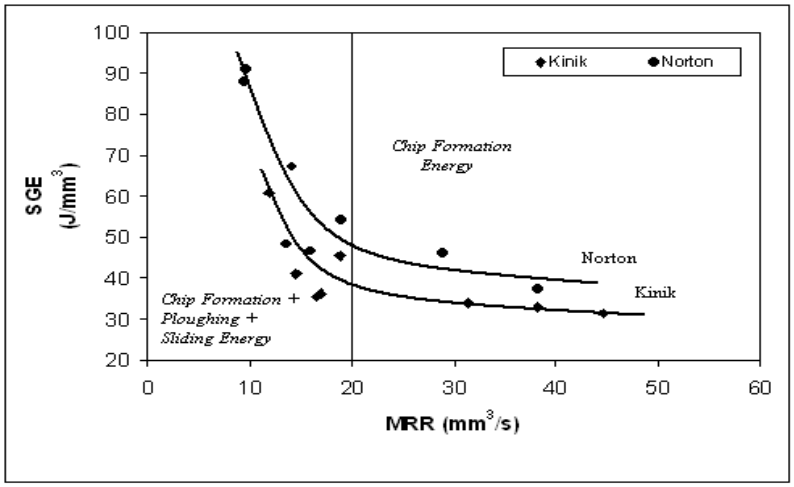

Figure 3.12: Specific grinding energy vs. material removal rate (Ti-6Al-4V)

The plots in Figures 3.12 and 3.13 also suggest that each rough grinding operation should be started at a material removal rate greater than ~20 mm^3/s for both materials using the wheels evaluated in the experiment to facilitate chip formation through shear and reduce the fraction of heat generated due to grain ploughing and sliding. The exact value to which the material removal rate can be increased beyond 20 mm^3/s to economically optimize the process depends on the wear rates of the grinding wheels along with other process constraints including thermal damage and workpiece chatter.

For the surface roughness response, the corresponding main effect plots using the S/N ratios are shown in Figures 3.13 and 3.14 for Inconel 718 and Ti-6Al-4V, respectively.

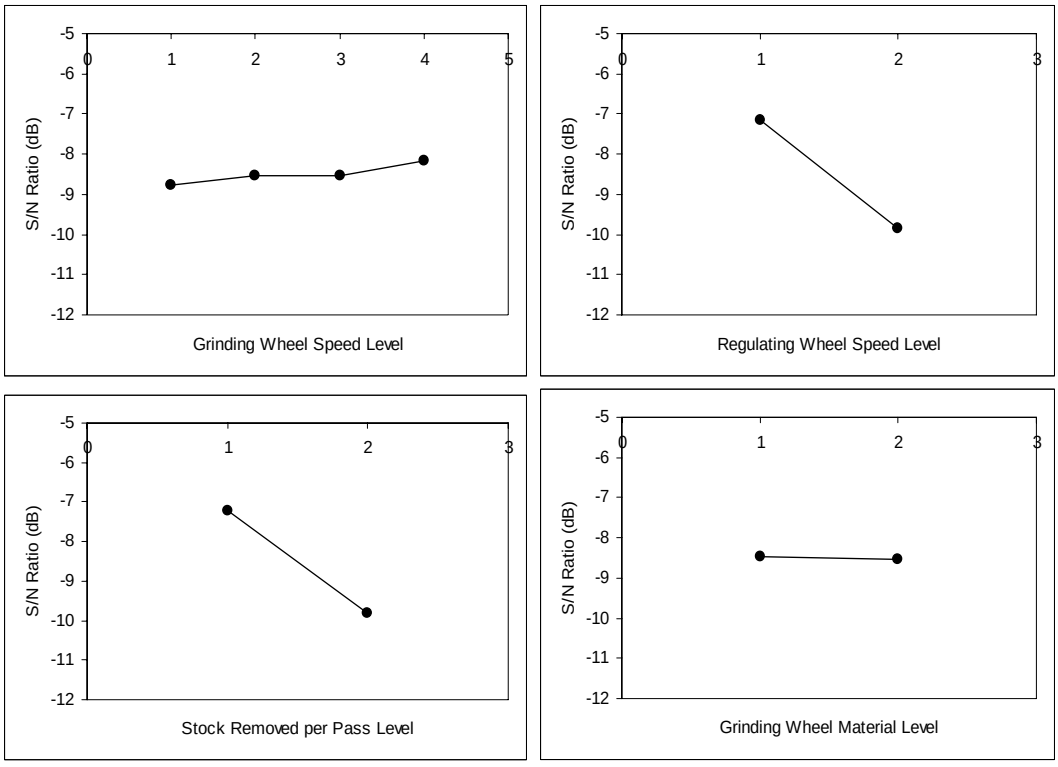

Figure 3.13. Effects of process parameters on surface roughness response (Inconel 718)

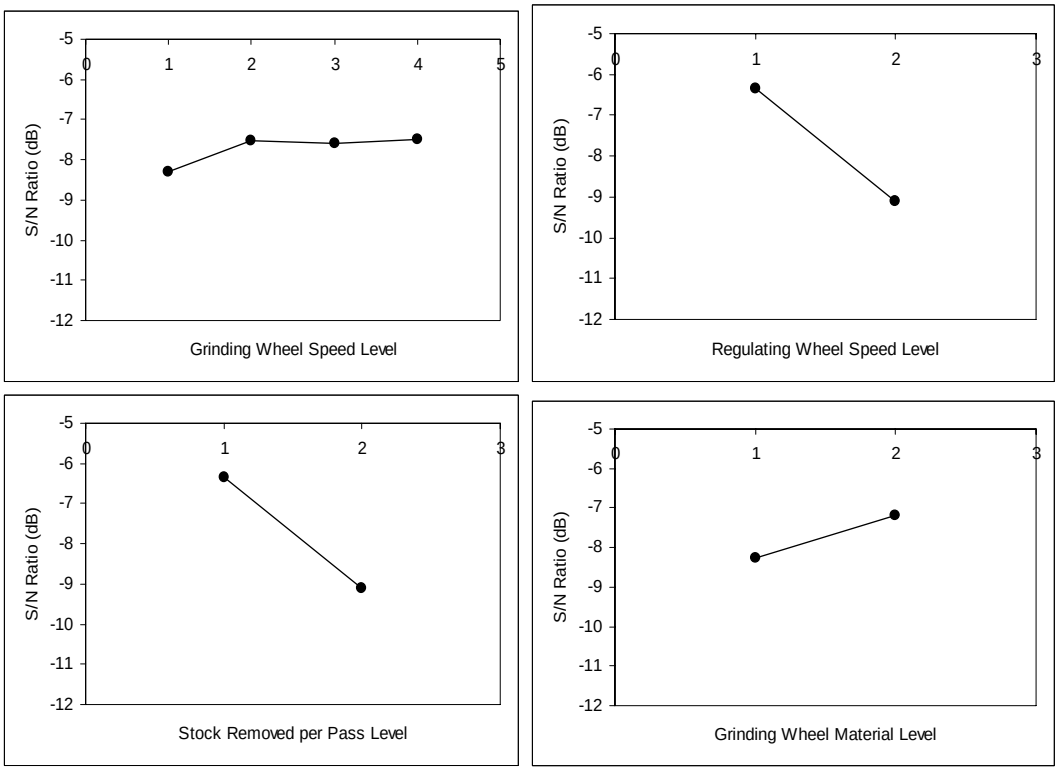

Figure 3.14: Effects of process parameters on surface roughness response (Ti-6Al-4V)

From the S/N tables given in Appendix D, the contribution of each experimental factor on the surface roughness response is shown in Table 3.12 for each workpiece material.

Table 3.12: Contribution of process parameters to the part surface roughness response

Workpiece Material	Grinding Wheel Speed	Regulating Wheel Speed	Stock Removed per Pass	Grinding Wheel Material
Inconel 718	10.3%	45.1%	43.5%	1.1%
Ti-6Al-4V	11.1%	37.0%	37.5%	14.4%

For Inconel 718, the regulating wheel speed had the greatest effect on the surface roughness, followed by the amount of stock removed per pass, the grinding wheel speed, and the grinding wheel material. For Ti-6Al-4V, the amount of stock removed per pass had the greatest effect on the surface roughness, followed by the regulating wheel speed,

the grinding wheel material, and the grinding wheel speed. In order to minimize the surface roughness, the grinding parameters should be set according to the recommendations in Table 3.13.

Table 3.13: Optimum parameter settings for minimum surface roughness

Workpiece Material	Grinding Wheel Speed (m/s)	Regulating Wheel Speed (m/min)	Stock Removed per Pass (μm)	Grinding Wheel Material
Inconel 718	33.5	13.4	76.2	A
Ti-6Al-4V	33.5	13.4	76.2	B

The Cincinnati wheel (A), with a grain packing density or structure number of 4, yields a better surface finish than the more open Norton SG wheel (B) with a structure number of 6 when grinding Inconel 718. The Norton wheel (B), with a hardness level of O and structure number of 6, yields a better surface finish than the softer and more open Kinik wheel (A) with a hardness level of N+ and structure number of 7 for Ti-6Al-4V.

The results of the S/N ratio analysis are valid assuming that no other experimental factors affect the measured responses besides the controllable factors that were included in the orthogonal array. However, during the trials, the process responses were also affected by parameters that could not be precisely controlled on a manual centerless grinder and included as experimental factors, including the feed rate and spark-out time. In particular, the large effects on the measured responses noted for the stock removal per pass parameter were likely overestimated because this parameter is highly correlated to the feed rate used to complete the pass before the part was ejected by the slotted regulating wheel. Therefore, the combined effect of all the parameters was determined using multiple regression as discussed in the next section.

3.4.2 Characterization Experiment – Regression Analysis

In order to account for the effects of parameters that were held constant or that could not be controlled precisely on a manual grinder when predicting the process responses, the data was analyzed using multiple regression. The key outputs of this analysis are the regression models for grinding power and surface roughness as a function of all the significant process parameters. The general form of the reduced multiple linear regression model constructed to predict a process response is given by

$$y = c_o + \sum_{i=1}^{n} c_i x_i + \varepsilon \tag{3.2}$$

where y is the predicted response value, x_i are the parameter variables, c_i are the regression model coefficients, and ε is the random error. For Inconel 718, the models are given by

$$P = 63.1U_d + 12.4V_g + 1102.3V_r + 3704.2d + 7118.8V_f - 183.5WM - 426.9 \tag{3.3}$$

$$R_a = -0.197U_d - 0.013V_g + 1.212V_r + 3.374d + 16.212V_f - 0.236t_s + 1.592 \tag{3.4}$$

where P is the grinding power in W, R_a is the arithmetic average surface roughness in μm, U_d is the dressing overlap ratio, V_g is the grinding wheel speed in m/s, V_r is the regulating wheel speed in m/s, d is the diameter reduction per pass in mm, V_f is the feed rate in mm/s, t_s is the spark-out time in s, and WM is the grinding wheel material (A=0, B=1). Similarly, the models for Ti-6Al-4V are given by

$$P = 125.4U_d + 20.0V_g + 459.0V_r + 3262.1d + 8015.8V_f + 150.3WM - 728.2 \tag{3.5}$$

$$R_a = -0.384U_d - 0.012V_g + 1.571V_r + 3.520d + 14.331V_f - 0.170WM - 0.143t_s + 1.84 \tag{3.6}$$

A detailed summary of the regression model statistics and a verification of the regression modeling assumptions for each response are provided in Appendix D. The final models, reduced to their final form by the backwards elimination technique, were significant at the 90% confidence level and provided a very good fit for the associated data set with R^2 values in the range of 0.915-0.987 without requiring any data transformations. In most applications, higher order models with interaction terms are usually preferred and more accurate for predicting any given process response over a wider range of process conditions, but the linear models obtained in this analysis were adequate over the range of parameter values used in the experiment.

Variable multicollinearity was also assessed by constructing a correlation coefficient matrix for the inclusive set of predictor variables as shown in Appendix D for the Inconel 718 grinding power response. When multicollinearity is present between any pair of predictor variables, the two variables are highly correlated and it is difficult to distinguish their individual effects on the response. Notably high correlation coefficients exceeding a value of 0.3 were identified between several process parameters, which could possibly be reduced by collecting additional experimental data, eliminating non-significant variables, or combining multiple correlated variables into a single variable. However, in this application, the presence of multicollinearity is not an issue since the regression models were only used to predict the process responses over the experimental range of parameter values.

The optimum parameters identified in the S/N ratio analysis and the regression models generated for the process responses are strictly valid for a static system without taking into account the effects of wheel wear on process performance. To analyze the

dynamic behavior of the system, a production run experiment previously outlined in Figure 3.3 was conducted for each workpiece material. During the experiment, the aforementioned process responses were monitored under different grinding conditions to develop empirical relations for wheel wear and to analyze wheel performance and material removal efficiency using standard metrics.

3.4.3 Production Run Experiment – Process Response Trends

A complete data summary of the process responses measured in time series for all the production runs is given in Appendix C. The grinding wheel, dressing parameters, and grinding parameters used for each Inconel 718 production run is summarized in Table 3.14.

Table 3-14. Process parameters for Inconel 718 production run experiment

Run	Number of Parts	Dressing Overlap Ratio	Grinding Wheel Speed (m/s)	Regulating Wheel Speed (m/min)	Stock Removed per Pass (μm)	Feed Rate (μm/s)	Grinding Wheel Material (A or B)
1-R	250	2.36	33.5	13.4	127	39.1	A
2-R	250	2.36	19.1	13.4	127	39.1	A
3-F	500	4.72	33.5	13.4	63.5	19.5	A
4-R	250	2.36	33.5	13.4	127	39.1	B
5-R	250	2.36	19.1	13.4	127	39.1	B
6-F	500	4.72	33.5	13.4	63.5	19.5	B

.

For each wheel material (A and B), two rough pass production runs (R) were conducted at different grinding wheel speeds (33.5 m/s or 1050 rpm and 19.1 m/s or 600 rpm) while holding the values of regulating wheel speed (13.4 m/min or 12 rpm), amount of stock

removed per pass (127 μm or 0.005 in.) and feed rate (39.1 μm/s or 0.092 in./min) constant. The grinding wheel speed was chosen as the variable parameter since it could be controlled precisely using the Power Flex 70 AC spindle drive interface available on the grinder.

The trends for the grinding power and diameter (OD) error measured during four rough pass Inconel 718 production runs of 250 parts each are shown in Figure 3.15.

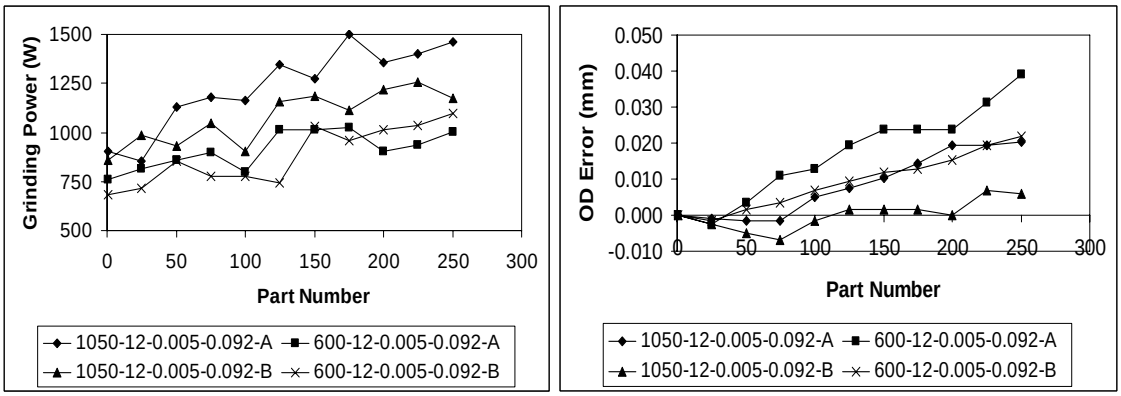

Figure 3.15: Process response trends for rough pass production runs (Inconel 718)

As seen in Figure 3.15, the grinding power increases with wheel wear in an approximately linear fashion for all grinding parameters and grinding wheel material combinations. The OD error, used to quantify radial wheel wear, increases in the positive direction indicating that the ground part is oversized. Figure 3.15 also shows that higher grinding wheel speeds result in higher values of grinding power over longer production runs but have a smaller effect on the accumulated diameter error. When comparing wheel wear performance as measured by the diameter error under the same grinding conditions, it can be seen that the Norton SG grinding wheel (B) wears at a slower rate

and thus allows the part to stay within the prescribed diameter tolerance range (± 12.7 μm or 0.0005 in.) longer than the Cincinnati wheel (A) over the same production period.

The trends for the grinding power and surface roughness measured during two finish pass production runs of 500 parts each for Inconel 718 are shown in Figure 3.16. One production run was conducted for each wheel material to compare wear performance in a 63.5 μm or 0.0025 in. stock removal pass under the wear-minimum grinding wheel speed identified from rough pass production runs. Similar to the rough pass production runs (Figure 3.15), the grinding power increases with wheel wear in a more or less linear fashion. The part surface roughness, an active part quality constraint in a finish pass production run, generally approaches a steady-state value with grinding wheel wear and abrasive grain dulling. Under constant dressing and grinding conditions, the properties of the grinding wheel determine the best achievable surface finish. Since the Cincinnati grinding wheel (A) has a lower structure number of 4 than the Norton SG wheel (B) with a structure number of 6, it yields a better surface finish as expected.

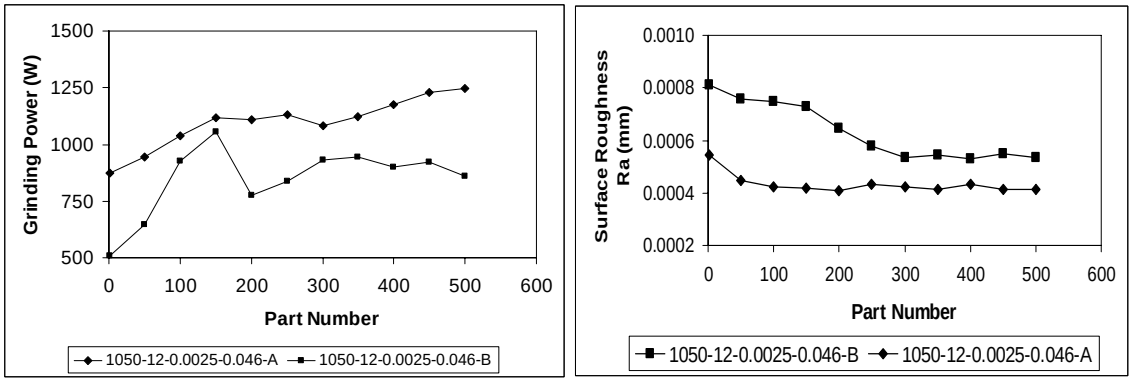

Figure 3.16: Process response trends for finish pass production runs (Inconel 718)

The combination of grinding wheel, dressing parameters, and grinding parameters used for each Ti-6Al-4V production run is summarized in Table 3.15.

Table 3.15: Process parameters for production run experiment (Ti-6Al-4V)

Run	Number of Parts	Dressing Overlap Ratio	Grinding Wheel Speed (m/s)	Regulating Wheel Speed (m/min)	Stock Removed per Pass (μm)	Feed Rate (μm/s)	Grinding Wheel Material
1-R	250	2.36	33.5	13.4	127	39.1	A
2-R	250	2.36	19.1	13.4	127	39.1	A
3-F	500	4.72	14.4	13.4	63.5	19.5	A
4-R	250	2.36	33.5	13.4	127	39.1	B
5-R	250	2.36	19.1	13.4	127	39.1	B
6-F	500	4.72	14.4	13.4	63.5	19.5	B

The trends for the grinding power and diameter (OD) error measured during 4 rough pass Ti-6Al-4V production runs of 250 parts each are shown in Figure 3.17. The same combination of rough pass parameters was used for Ti-6Al-4V as for the Inconel 718 trials.

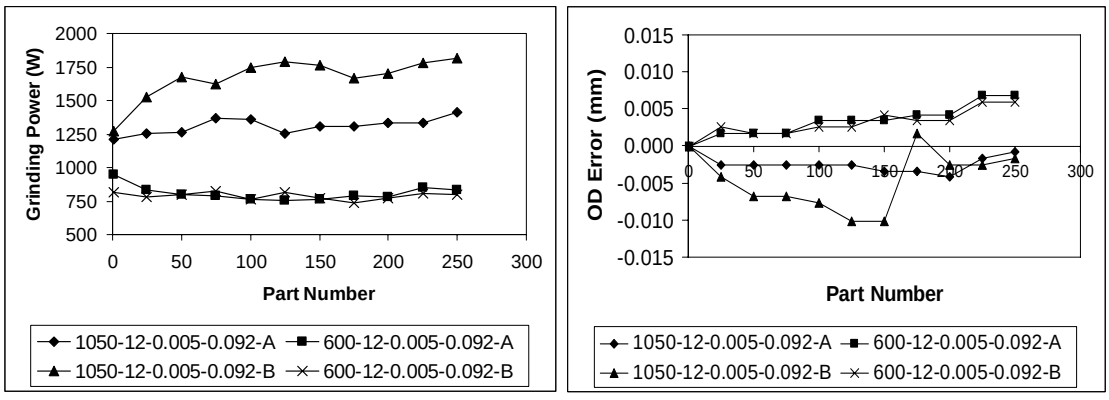

Figure 3.17: Process response trends for rough pass production runs (Ti-6Al-4V)

As seen in Figure 3.17, the grinding power increases with wheel wear at the high grinding wheel speed setting (33.5 m/s or 1050 rpm) and remains favorably constant under the low setting (19.1 m/s or 600 rpm). The diameter error increases in the positive direction for the low grinding wheel speed production runs, but for the runs conducted at high wheel speeds, it stays in the negative range indicating that the ground part is consistently undersized. The increase in power and the fluctuations in diameter error are particularly prominent for the Norton grinding wheel (B), which may suggest that its high hardness level and high grain packing density contribute to higher grinding temperatures and worsen the wheel loading effect, especially at higher wheel speeds. At elevated grinding temperatures, Ti-6Al-4V exhibits high chemical affinity to the wheel material and adheres to the grain tips. In turn, the enlarged grains have the ability to penetrate further into the part and remove more material than intended, especially if the part is also undergoing thermal expansion. In contrast, the process responses measured at the low wheel speed setting show more favorable trends. Since Ti-6Al-4V does not respond favorably to hard cutting action as Inconel 718, the grinding wheel speed should be set to the lower setting (19.1 m/s or 600 rpm). Alternatively, a softer wheel (hardness J-N) may be used for speeds exceeding 19.1 m/s.

The trends for the grinding power and surface roughness responses measured during 2 finish pass Ti-6Al-4V production runs of 500 parts each are shown in Figure 3.18. One production run was conducted for each wheel material to compare their performance in a 63.5 μm (0.0025 in.) stock removal pass at a low grinding wheel speed (14.4 m/s or 450 rpm).

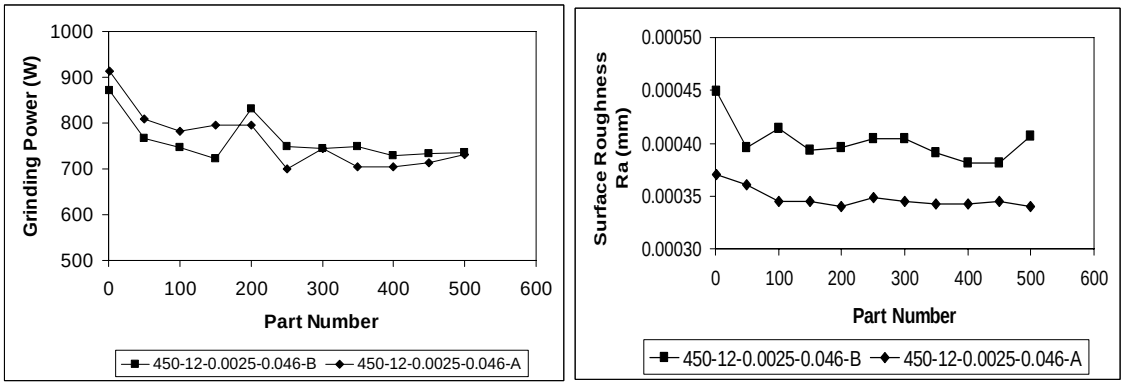

Figure 3.18: Process response trends for finish pass production runs (Ti-6Al-4V)

As seen in Figure 3.18, the grinding power and part surface roughness stay relatively constant over the period as a result of the softer wheel-cutting action at the lower wheel speed. In this case, since the Norton grinding wheel (B) has a lower structure number and a higher hardness level than the Kinik wheel (A), it produces a better surface finish as expected.

3.4.4 Production Run Experiment –Regression Analysis

The data for the critical part dimensions measured after grinding the 250th part in each production run was used to construct multiple regression models for the wheel wear indicator responses. The indicator of wheel radial wear was the diameter error (DE), which quantifies the cumulative deviation of the shank diameter from the target dimension. The indicator of wheel edge wear was the transition radius error (TRE), which quantifies the cumulative deviation of the transition radius from the target dimension. To maximize the predictive power of the regression models with a limited number of data points, the following predictor variables were used for the responses:

equivalent chip thickness h_{eq}, stock removed per pass d, and grinding wheel material WM. The equivalent chip thickness is a quantitative measure of the depth of penetration of abrasive grains into the workpiece material and it varies with many wheel surface parameters. Empirical studies of grinding behavior using the equivalent chip thickness parameter confirm that there is a direct relationship between chip thickness and the G-ratio, where lower values of chip thickness typically result in less wheel wear [135]. For plunge centerless grinding, the equivalent chip thickness h_{eq} is given by

$$h_{eq} = a\left(\frac{V_w}{V_g}\right) = \frac{1}{2}\pi D_w\left(\frac{V_f}{V_g}\right) \tag{3.7}$$

where a is the depth of cut per workpiece revolution, D_w is the workpiece diameter, V_w is the workpiece speed, V_f is the feed rate, and V_g is the grinding wheel speed. For Inconel 718, the models for the accumulated amount of wheel wear after grinding 250 parts based on the critical part dimensions are given by

$$DE = 1.505\ h_{eq} - 0.0113 WM \tag{3.8}$$

$$TRE = 7.264\ h_{eq} - 0.0491 WM \tag{3.9}$$

where DE is the diameter error in mm, TRE is the transition radius error in mm, h_{eq} is the equivalent chip thickness in μm, and WM is the grinding wheel material (A=0, B=1). Similarly, the Ti-6Al-4V models are given by

$$DE = 0.457\ h_{eq} - 0.0054 \tag{3.10}$$

$$TRE = 11.446\ h_{eq} \tag{3.11}$$

In Equations 3.10 and 3.11, it should be noted that the grinding wheel material WM did not have a significant effect on the dimensional errors over the experimental range of parameters for Ti-6Al-4V. The final models, reduced to their final form by the backward elimination technique, were statistically significant at the 90% confidence level with R^2

values in the range of 0.613-0.941. The diameter error was used as the primary wear indicator in the ensuing optimization analysis because it is less sensitive to changes in setup parameters relative to the transition radius error.

No representative models were generated for the surface roughness since the value of spark-out time, an important predictor variable, was held approximately constant in the production run experiments and its contribution could not be measured. However, since the part surface roughness decreased with wheel wear within the range of experimental dressing conditions considered in this study, the regression model for surface roughness generated in the characterization experiment can still be applied to safely satisfy the surface finish requirement. For the grinding power, an upper limit of ~1 kW can be added to the power prediction for the sharp wheel to represent the prediction for the worn wheel after grinding 250 parts under any set of grinding parameters as supported by the trend plots in Figures 3.15 and 3.17.

3.4.5 Production Run Experiment – Wheel Performance and Grinding Efficiency

The metric used to compare the wear performance of grinding wheels in the production run experiment was the G-ratio, which is defined as the ratio of volume of material removed to the volume of wheel wear. The volume of material removed is defined as the product of the volume of material removed per pass and the total number of grinding passes. For plunge centerless grinding, the accumulated volume of radial wheel wear ΔV_g is given by

$$\Delta V_g = \pi \bar{D}_g \, \Delta r_g b \tag{3.12}$$

where $\bar{D}_g$ is the mean of the wheel diameters before and after the production run, Δr_g is the decrease in wheel radius according to the measured diameter error, and *b* is the grinding width.

The G-ratios obtained for Inconel 718 for all the production runs conducted with each grinding wheel are shown in Table 3.16 in increasing order of equivalent chip thickness.

Table 3.16: G-ratio summary for Inconel 718 grinding wheels

Production Runs	Operation	Equivalent Chip Thickness (μm)	Cincinnati Wheel (A) G-Ratio	Norton SG Wheel (B) G-Ratio
3, 6	Finish Pass	0.0073	49.0	97.9
1, 4	Rough Pass	0.0145	20.4	70.2
2, 5	Rough Pass	0.0254	10.7	18.9

As seen in Table 3.16, the G-ratios for the Norton SG grinding wheel (B) were 2-4 times higher than for the Cincinnati wheel (A) over the range of experimental parameters. Also, it is very important to note that the G-ratio obtained with the Norton SG wheel (B) at the equivalent chip thickness value of 0.0254 μm was approximately the same as the G-ratio obtained with the Cincinnati wheel (A) at the value of 0.0145 μm. This suggests that the Norton SG wheel (B) can be used in place of the Cincinnati wheel (A) to reduce the grinding cycle time with higher feed rates without incurring any losses in wear performance.

The G-ratios obtained for Ti-6Al-4V for all the production runs conducted with each grinding wheel are shown in Table 3.17 in increasing order of equivalent chip thickness.

Table 3.17: G-ratio summary for Ti-6Al-4V grinding wheels

Production Runs	Operation	Equivalent Chip Thickness (μm)	Kinik Wheel (A) G-Ratio	Norton Wheel (B) G-Ratio
1, 4	Rough Pass	0.0145	N/A	N/A
3, 6	Finish Pass	0.0170	98.7	98.7
2, 5	Rough Pass	0.0254	61.8	70.8

As seen in Table 3.17, the G-ratios for the Norton grinding wheel (B) were very similar to the Kinik grinding wheel (A) over the range of experimental parameters. The G-ratios for the rough pass production runs conducted at the high wheel speed setting (33.5 m/s or 1050 rpm) could not be obtained based on the negative value of the diameter error measured at the end of the production runs. Comparing the G-ratios for both workpiece materials, it can be seen that Inconel 718 is typically more difficult to grind than Ti-6Al-4V since it will consume a greater number of grinding wheels over a production period.

The metric used to compare material removal performance under different grinding conditions for each wheel in the production run experiment was the grinding efficiency. The grinding efficiency is found by dividing the G-ratio by the specific grinding energy [15], where higher efficiencies are desirable in order to maximize productivity. For plunge centerless grinding, the specific grinding energy e is the grinding power divided by the material removal rate as given by

$$e = \frac{P}{Q_w} = \frac{2P}{\pi D_w V_f b} \tag{3.13}$$

where P is the grinding power, Q_w is the volumetric material removal rate, D_w is the workpiece diameter, V_f is the feed rate, and b is the grinding width. The grinding efficiencies obtained for the Inconel 718 production runs are summarized in Table 3.18.

Table 3.18: Grinding efficiency summary for Inconel 718 grinding wheels

Production Runs	Operation	Equivalent Chip Thickness (μm)	Cincinnati Wheel (A) Efficiency ($mm^3/W/s$)	Norton SG Wheel (B) Efficiency ($mm^3/W/s$)
3, 6	Finish Pass	0.0073	0.60	1.75
1, 4	Rough Pass	0.0145	0.44	1.86
2, 5	Rough Pass	0.0254	0.34	0.53

As seen in Table 3.18, the Inconel 718 grinding efficiency of the Norton SG wheel (B) was up to 5 times higher than the efficiency of the Cincinnati wheel (A) over the range of experimental parameters. The efficiency for grinding Inconel 718 did not change significantly as the equivalent chip thickness was increased from a value of 0.0073 μm in the finish pass operation (Q_w = 15.4 mm^3/s) to a value 0.0145 μm in the rough pass operation (Q_w = 30.9 mm^3/s) by maintaining the high wheel speed setting (33.5 m/s or 1050 rpm) and doubling the feed rate, which provides further evidence that the operation should be conducted at material removal rates exceeding 20 mm^3/s to increase process efficiency. The results also suggest that increasing the feed rate in proportion to an increase in the depth of cut may reduce the grinding cycle time without significant losses in wheel wear performance or large increases in specific grinding energy, although more trials are needed with larger stock removal passes to identify the exact point at which the optimum chip thickness value is exceeded using this approach. Also, when the grinding wheel speed was reduced to 600 rpm (h_{eq} = 0.0254 μm) under otherwise constant conditions, the grinding efficiency decreased for both wheels and more significantly for the Norton SG wheel (B). Thus, the Inconel 718 grinding wheels should be operated at the higher speed setting (33.5 m/s or 1050 rpm) to maximize their material removal efficiency.

The grinding efficiencies obtained for all the Ti-6Al-4V production runs are summarized in Table 3.19.

Table 3.19: Grinding efficiency summary for Ti-6Al-4V grinding wheels

Production Runs	Operation	Equivalent Chip Thickness (μm)	Kinik Wheel (A) Efficiency ($mm^3/W/s$)	Norton Wheel (B) Efficiency ($mm^3/W/s$)
1, 4	Rough Pass	0.0145	N/A	N/A
3, 6	Finish Pass	0.0170	2.19	1.84
2, 5	Rough Pass	0.0254	2.31	2.74

As seen in Table 3.19, the Ti-6Al-4V grinding efficiency of the Kinik (A) and Norton (B) wheels were not considerably different. The grinding efficiency increased for both wheels when the speed was reduced to 600 rpm (h_{eq} = 0.0254 μm) under otherwise constant conditions, which maintained the specific grinding energy at relatively constant levels throughout the production run. This suggests that the Ti-6Al-4V wheels should be operated at the lower speed setting (19.1 m/s or 600 rpm) to reduce wheel loading, which is more pronounced at higher wheel speeds.

3.4.6 Production Run Experiment – Grinding Wheel Surface Topography Evolution

From the beginning to the end of a production run, the efficiency of the grinding operation changes due to the stochastic evolution of the grinding wheel surface topography. As the wheel progresses through its stages of wear, the changing condition of the surface constantly alters the cutting action for each individual grinding pass. Although it is beyond the scope of this study to model grinding wheel topography,

several important parameters defined for characterizing the grinding wheel surface condition, namely the percentage of active cutting grains, the percentage of wear flat area, and the percentage of grain pullouts, were monitored using the imprint technique outlined earlier to provide insight into the wear characteristics of each grinding wheel. The evaluation of wheel topography using the defined parameters was only conducted for the Inconel 718 wheels in order to analyze why the Norton SG wheel (B) outperformed the Cincinnati wheel (A) in terms of grinding efficiency in the rough pass production runs. A summary of the wheel topography imprint data is provided in Appendix D.

In order to characterize the wheel surface condition, the accuracy of the imprint method was first verified by measuring the average diameter of an imprinted abrasive grain to see how it compares to published values. The imprint method leads to some variation in the maximum depth of penetration of the lead surface as the human hand cannot replicate the same imprinting force during each trial. The histogram in Figure 3.19 shows the typical grain diameter distribution for the grains exposed after rough dressing of the 80-grit size Norton SG wheel for Inconel 718, which was obtained by an optical profilometer analysis of 5 imprints taken randomly across the wheel surface.

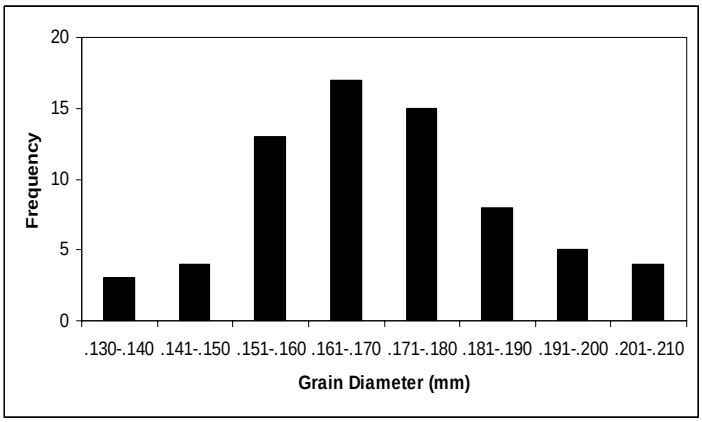

Figure 3.19: Grain diameter distribution for Norton SG grinding wheel (3SGP80-O6-VH)

The distribution of the grain diameter is approximately normal as confirmed by earlier experimental studies by Hou and Komanduri [136]. For the 80-grit size wheel, the average grain diameter was determined to be approximately 170 μm, which is within the range of 147-190 μm as estimated from published relations [137]. Therefore, the imprint method yields sufficiently accurate results.

In addition, using the Zygo optical profilometer to analyze the imprints, it is possible to obtain information about the cross-sectional geometry, orientation, and spatial distribution of the abrasive grains in any direction along the surface. The typical grain protrusion height, defined as the distance between the top grain cutting edge and the baseline surface of the bond matrix material, was found to be in the range of 5-15 μm after dressing the grinding wheel for a finish pass as suggested by the grain profile trace in Figure 3.20. Under rough dressing conditions, this value was found to be in the range of 15-30 μm for all the wheels used in the experiment. Different authors have reported grain protrusion height values of 23-48 μm [138, 139].

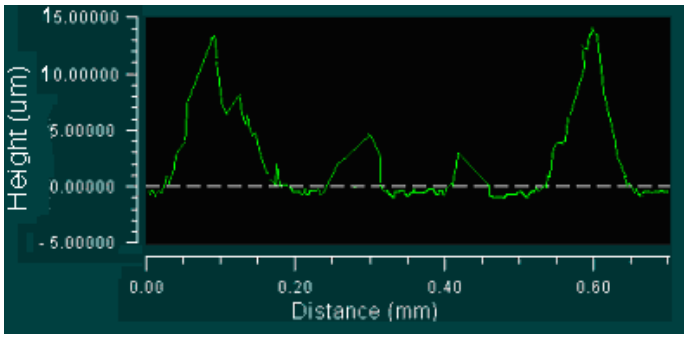

Figure 3.20: Sample grain cross-sectional profile trace after wheel dressing

The condition of each Inconel 718 wheel was characterized during 2 rough pass production runs with the corresponding process parameters as shown in Table 3.20.

Table 3.20: Dressing and grinding parameters for Inconel 718 rough pass production runs

Production Run	Dressing Overlap Ratio	Grinding Wheel Speed (m/s)	Regulating Wheel Speed (m/min)	Stock Removed per Pass (μm)	Feed Rate (μm/s)	Grinding Wheel Material
A1	2.36	33.5	13.4	127	39.1	A
A2	2.36	19.1	13.4	127	39.1	A
B1	2.36	33.5	13.4	127	39.1	B
B2	2.36	19.1	13.4	127	39.1	B

One of the topological parameters used to assess the condition of the grinding wheel surface in the rough pass production runs was the percentage of active cutting grains or the percentage of total grains available on the surface that engage with the workpiece material during the grinding pass. Figure 3.21 shows a plot of the percentage of active cutting grains for each production run. This parameter was determined by dividing the number of grains with wear flat regions by the total number of grains in a fixed viewing area for 5 random imprints.

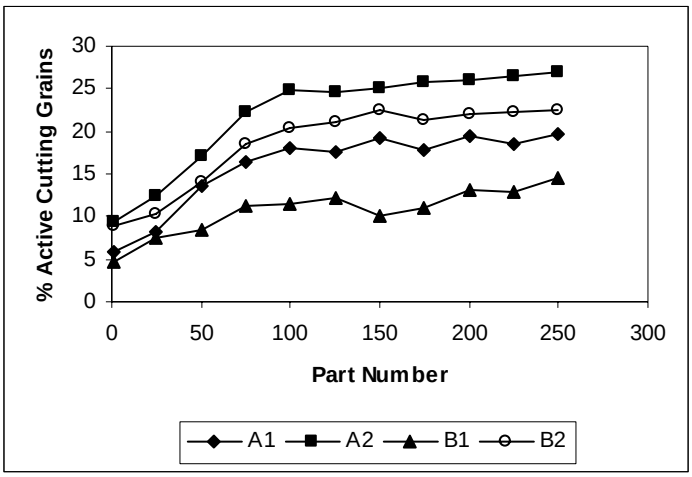

Figure 3.21: Percentage of active cutting grains (Inconel 718 grinding wheels)
A: Cincinnati B: Norton SG

The wear flat regions on the grains can be identified by the clear, shiny spots reflected on the imprints as shown in Figure 3.22.

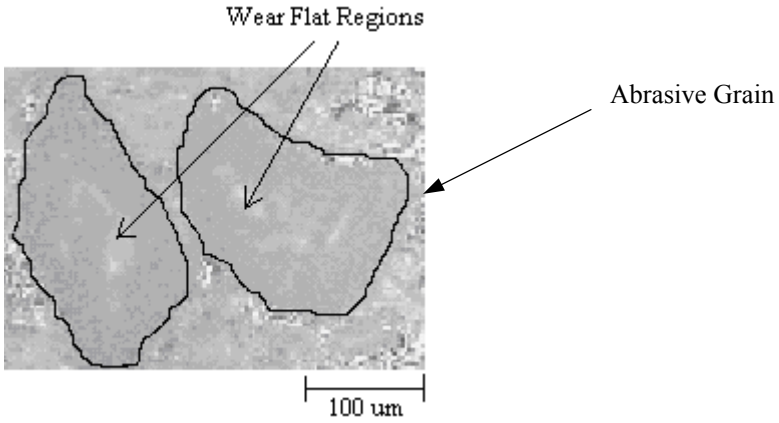

Figure 3.22: Sample image of grain wear flat regions (3SGP80-O6-VH)

Several observations can be made from Figure 3.21. As the wheel progresses through its wear stages (grain fracture → attritious wear → bond fracture), the percentage of active cutting grains increases as expected. The increase in the percentage of active cutting grains is more rapid in the early stages of the production run, but after grinding roughly 100 parts, the wheel enters the attritious wear stage and the rate of increase becomes much lower. For both wheels, the grain self-sharpening ability is enhanced at the lower wheel speed setting. The percentage of active grains is consistently lower for the Norton SG wheel (B) than for the Cincinnati wheel (A), which may be attributed to its finer grain fracture behavior. Finer grain fracture is preferred over coarser grain fracture in order to maximize the utility of each grain exposed after dressing.

A second topological parameter used to assess the condition of the grinding wheel surface was the grain wear flat area, which serves as a quantitative measure of abrasive grain dullness as the wheel progresses through its wear stages. Figure 3.23 shows a plot

of the percentage of grain wear flat area for each production run, which was determined with the aid of a fine grid superimposed on the top view of the optical profilometer images. The percentage of wear flat area is defined as the fraction of the total viewing area consisting of wear flat regions.

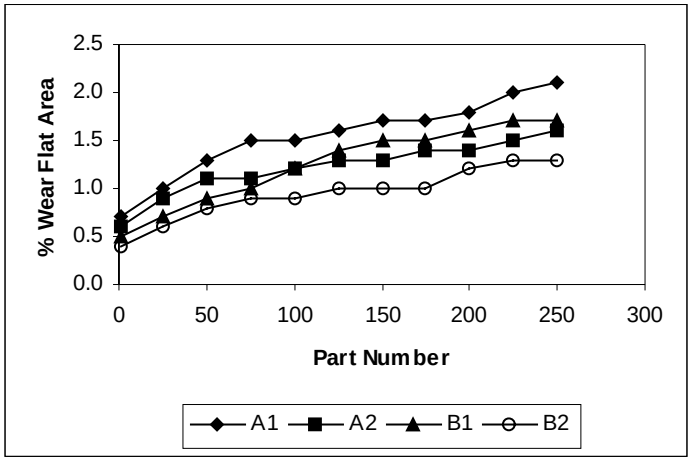

Figure 3.23: Percentage of wear flat area (Inconel 718 grinding wheels)
A: Cincinnati B: Norton SG

Several observations can be made from Figure 3.23. As the wheel progresses through its wear stages, the percentage of wear flat area increases as expected. Both wheels demonstrate better self-sharpening ability at the lower wheel speed setting (19.1 m/s or 600 rpm) than at the high setting (33.5 m/s or 1050 rpm). However, the percentage of wear flat area for the Norton SG wheel (B) stays lower throughout the production run than for the Cincinnati wheel (A), which can be attributed to its superior micro-fracturing characteristics. A lower percentage of wear flat area results in less rubbing, lower grinding forces, and a lower chance of grain pullout.

A third topological parameter used to assess the condition of the wheel surface was the percentage of grain pullouts. Figure 3.24 shows a plot of the percentage of grain

pullouts for each production run, which was determined by dividing the static density of grains after dressing the wheel by the static density of grains at different points during the production run.

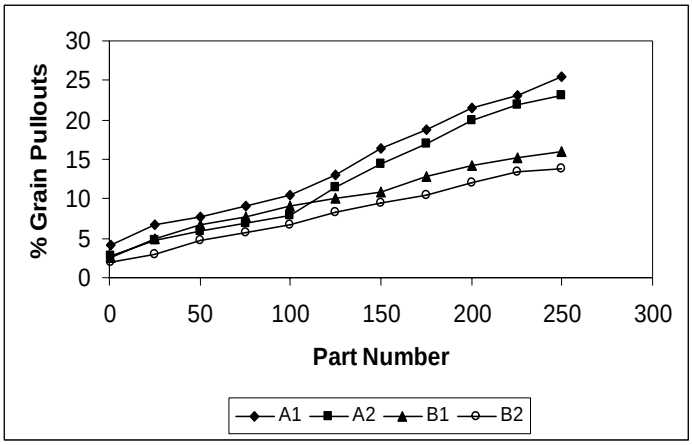

Figure 3.24: Percentage of grain pullouts (Inconel 718 grinding wheels)
A: Cincinnati B: Norton SG

Several observations can be made from Figure 3.24. As the wheel progresses through its wear stages, the percentage of grain pullouts increases as expected. For both wheels, the grain pullout effect is more prominent at the higher wheel speed setting (33 m/s or 1050 rpm) where the cutting action is harder and the grain self-sharpening ability is more restricted. The increase in the percentage of grain pullouts is expected to continue even after grinding 250 parts as the percentage of active cutting edges and wear flat area continue to increase with wheel wear. A lower percentage of grain pullouts is observed for the Norton SG wheel (B) due to its finer fracturing behavior, which keeps the grains sharper for a longer time and reduces the forces exerted on each grain to delay the onset of bond fracture.

In summary, the plots shown in the previous figures highlight some of the wear characteristics of the Inconel 718 grinding wheels in the rough pass production runs and confirm the advantages of the Norton SG wheel over the current Cincinnati wheel that were highlighted previously by a comparison of their G-ratios and grinding efficiencies.

3.5 Conclusions

In this chapter, two data analysis methods (Taguchi's S/N ratios and regression analysis) were utilized to characterize the relationships among the key grinding parameters and process responses. The S/N ratio analysis was conducted to identify the optimum combination of controllable parameters in the experimental range that can be selected to minimize the risk of part quality constraint violations. During the experimental trials, the process responses were also affected by parameters that could not be controlled precisely on a manual feed centerless grinder and included as experimental factors, including the feed rate and spark-out time. The combined effect of all the parameters on the measured responses was determined using multiple regression. In a subsequent production run experiment, the response trends were monitored to analyze the effects of wheel wear and to determine the most efficient conditions for material removal.

The following key conclusions can be made based on the results of this study:

- For both workpiece materials, the grinding power is minimized by using the lowest grinding and regulating wheel speed settings and removing smaller amounts of stock per pass in combination with using lower feed rates. These

results are generally in agreement with earlier studies conducted to establish the material removal rate limits in centerless grinding [71].

- For both workpiece materials, the surface roughness is minimized by using the highest grinding wheel speed setting and lowest regulating wheel speed setting in addition to removing smaller amounts of stock per pass in combination with using lower feed rates. These results are in agreement with the grain depth of engagement theory presented in grinding textbooks [15].
- For the Inconel 718 and Ti-6Al-4V grinding wheels used in the experiments, results show that material removal rates less than ~20 mm^3/s are in the inefficient grinding regime, which is dominated by rubbing and ploughing of the work material instead of shearing. The operation should be performed at material removal rates greater than 20 mm^3/s in order to improve the process efficiency and productivity.

In the next chapter, the regression models generated in the characterization and production run experiments are used in combination with mechanistic models developed for centerless grinding to establish the feasible operating region bounded by process constraints and to find the optimum grinding conditions under the economic objective of minimum cost per part.

CHAPTER 4

METHODOLOGY FOR ECONOMIC OPTIMIZATION OF CENTERLESS GRINDING PARAMETERS

4.1 Introduction

In industrial grinding operations, process parameters have historically been selected according to machining data handbooks or operator experience. Such practices are still common in the manufacturing plant today, where overly conservative parameters are used in order to avoid machine tool failure and meet part quality specifications. In order to avoid such practices leading to suboptimal cycle times, it is necessary to develop a systematic methodology for optimizing the grinding parameters that can be replicated in a production setting to improve the process performance.

As discussed in Chapter 2, the primary approaches currently used to optimize the productivity of grinding operations are off-line optimization by design of experiments (Figure 4.1) and on-line optimization by adaptive control.

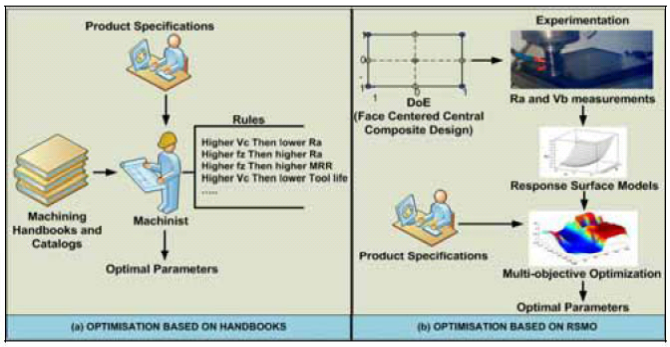

Figure 4.1: Off-line optimization approach based on design of experiments [140]

Off-line parameter optimization consists of conducting experiments to generate models for the process constraints and creating objective functions for total cost per part or production time per part that can be solved using a suitable optimization algorithm. On-line optimization, a more robust alternative to any off-line approach that accounts for stochastic process variations, consists of continuously adjusting parameters according to data that describes the actual state of the process to maintain a measured response such as normal force or grinding power at a prescribed value while maximizing the material removal rate. Despite its advantages, the on-line optimization approach has yet to be implemented for centerless grinding as machine tool designers are still looking for ways to develop and integrate adaptive controllers into CNC machines to remove the operator out of the process control loop. One major drawback is the lack of cost-effective, accurate, and reliable sensors for simultaneous monitoring of process responses. Considering the current technological limitations of on-line optimization, an off-line strategy was developed for the centerless grinding operation analyzed in this study.

4.2 Solution Approach

In Chapter 2, several off-line techniques were presented for optimizing the process parameters in different grinding operations. These techniques include analytical methods such as classical machining economics and design of experiments (DOE) and iterative mathematical search methods such as linear programming (LP), non-linear programming (NLP), and dynamic programming (DP). Among these methods, classical machining economics is one of the most frequently used techniques in the optimization of

traditional machining operations. However, for the optimization of inherently stochastic grinding processes, the application of this deterministic technique has been rather limited. One of the major limitations is the lack of reliable tool life relationships that account for the effect of all the relevant process parameters. In addition, the derived optimum conditions are often impossible to implement as they violate machine tool or part quality constraints. In order to utilize this method, it is therefore necessary to include process constraint identification as an intermediate step in the solution approach.

In this chapter, a scientific and practical methodology is outlined and carried out to determine the optimum operating conditions in the centerless grinding of Inconel 718 and Ti-6Al-4V superalloy fasteners under the objective of minimum cost per part (Figure 4.2). This method combines experimental design techniques with classical machining economics theory to find the best solution. To overcome some of the aforementioned limitations of using classical machining economics as an optimization tool, the empirical regression models developed in Chapter 3 are used to construct the feasible operating region bounded by process constraint boundaries as discussed in the ensuing sections.

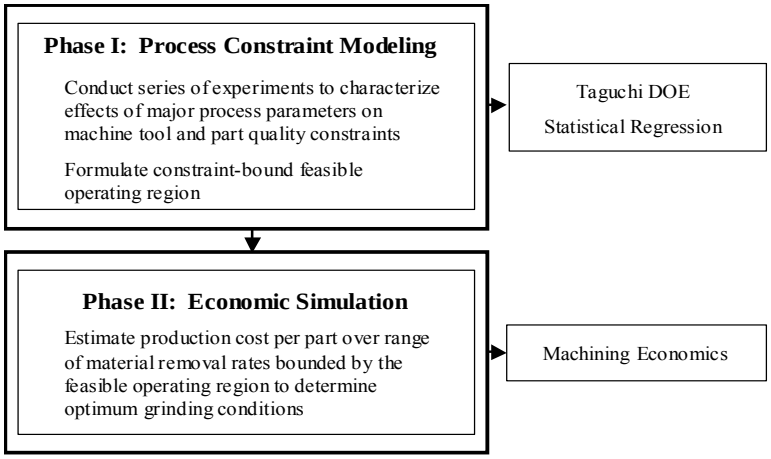

Figure 4.2: Flow chart of solution approach

4.3 Modeling of Process Constraints

In order to identify the feasible operating region where the grinding operation can be performed without violating the imposed part quality characteristics, the regression models for grinding power, surface roughness, and wheel wear generated in the characterization and production run experiments discussed in Chapter 3 were used in combination with mechanistic models for thermal damage and diameter dimension error presented in the ensuing sections to formulate the constraint boundaries for the process and determine whether or not they are active. In the rough grinding operation, the material removal rate can be increased up to the process constraints of machine spindle power, part thermal damage, and workpiece chatter. In the finish grinding operation, the active constraints are the part surface finish and dimensional accuracy as prescribed by the tolerance ranges for the fastener outer diameter, taper, transition angles and radii, and roundness. The ensuing sections present the models used to formulate the feasible operating region where the grinding parameters can be selected to safely meet the machine tool and part quality constraints.

4.3.1 Machine Tool Spindle Power

The centerless grinder used in this study was the OM-2 model manufactured by Cincinnati with a maximum spindle power of 15 hp (11.25 kW). The grinding power available on this machine tool in any operation for a given part diameter and length is a function of the grinding wheel speed and size according to the data shown in Table 4.1.

Table 4.1: Power capacity per unit width of wheel used as a function of wheel diameter and speed [141]

Wheel Speed/Diameter	350 mm	450 mm	600 mm
33 m/s	30 W/mm	60 W/mm	90 W/mm
43 m/s	50 W/mm	100 W/mm	150 W/mm
60 m/s	100 W/mm	150 W/mm	200 W/mm

According to Table 4.1, the machine tool spindle power constraint would be active when the grinding power exceeds 3-4 kW using a wheel speed of ~20 m/s and when the grinding power exceeds 5-6 kW using a wheel speed of ~33 m/s for a grinding wheel diameter of 609.6 mm (24 in.) and grinding width of 63.5 mm (2.5 in.) used in this study.

As supported by experimental evidence and the data shown in Table 4.1, the machine tool power constraint is not active for the 7.94 mm (5/16 in.) diameter part over the range of grinding parameter values used in the characterization experiment. Under the most severe grinding conditions corresponding to the highest grinding wheel speed setting (33.5 m/s) and the largest reduction in workpiece diameter (127 μm), the grinding power typically does not exceed 1.5 kW as predicted by the empirical regression generated in Chapter 3 over the range of feed rates and workpiece speeds used in the experimental trials (Table 4.2).

Table 4.2: Grinding power as a function of feed rate and workpiece speed (Inconel 718)

Feed Rate / Workpiece Speed	10 μm/s	20 μm/s	30 μm/s	40 μm/s	50 μm/s
200 mm/s	908	980	1051	1122	1193
250 mm/s	963	1035	1106	1177	1248
300 mm/s	1019	1090	1161	1232	1303
350 mm/s	1074	1145	1216	1287	1358
400 mm/s	1129	1200	1271	1342	1414

The data shown in Table 4.1 was validated experimentally by performing a grinding pass under the conditions used in the characterization experiment using a very low grinding wheel speed (8 m/s or 250 rpm). For a grinding pass conducted using a wheel speed of 8 m/s and a grinding width equal to the part length of 63.5 mm (2.5 in.), the spindle power limit would be exceeded when the grinding power exceeds ~1-1.5 kW according to the predictions in Table 4.1. In an actual trial, this prediction was proven to be accurate as the spindle torque was insufficient to perform material removal over the experimental range of feed rates and workpiece speeds (Table 4.2). Although the spindle power constraint was not active over the experimental range of process parameters for the size of the parts used in this study, the above analysis can be extended to predict the grinding power limit for any combination of wheel and workpiece.

4.3.2 Workpiece Thermal Damage

There is no widely accepted model for part thermal damage in centerless grinding, but two practical models can be used to monitor the onset of grinding burn. In a model proposed by Malkin [15], the critical specific grinding energy e_c for workpiece burn is given by

$$e_c = \frac{\kappa_w D_e^{1/4} T_c}{1.06 V_w^{1/2} a^{3/4} \alpha_w^{1/2} R_w} \tag{4.1}$$

where κ_w is the thermal conductivity of the workpiece material, D_e is the equivalent diameter, V_w is the workpiece surface speed, a is the depth of cut per workpiece revolution, T_c is the contact zone temperature resulting in grinding burn of the workpiece

material, α_w is the thermal diffusivity of the workpiece material, and R_w is the experimental heat partition ratio or the fraction of grinding energy entering the workpiece through the contact zone as heat. In Equation 4.1, the equivalent diameter D_e for an external cylindrical grinding operation is given by

$$D_e = \frac{D_g D_w}{D_g + D_w} \tag{4.2}$$

where D_g and D_w are the diameters of the grinding wheel and workpiece, respectively. The depth of cut per workpiece revolution a is defined for centerless grinding as given by

$$a = \frac{V_f}{2N_w} \tag{4.3}$$

where V_f is the feed rate and N_w is the workpiece rotational speed. A similar expression of the model in Equation 4.1 is proposed and verified by Rowe et al. [142] for a cast iron centerless grinding operation, where the critical specific grinding energy for workpiece burn e_c is given by

$$e_c = \left(\frac{K_t (\kappa\rho c)_w^{1/2} T_c}{a R_w} \right) \left(\frac{l_g}{V_w} \right)^{1/2} \tag{4.4}$$

where $(\kappa\rho c)_w$ is the workpiece material thermal coefficient defined as the product of the workpiece material thermal conductivity κ_w, density ρ_w, and specific heat c_w and K_t is the heat flux distribution coefficient with all other variables are as previously defined. In Equation 4.4, a triangular shape for the heat flux distribution can be assumed for most conventional grinding operations corresponding to a coefficient K_t of 0.93 [76]. If a square law or uniform heat flux distribution is assumed for the process, the corresponding heat flux distribution coefficients are 0.83 and 0.89, respectively. In Equation 4.4, the

parameter l_g is defined as the wheel-workpiece geometric contact length, and for an external cylindrical grinding operation it is given by

$$l_g = \sqrt{aD_e} = \sqrt{a\left(\frac{D_g D_w}{D_g + D_w}\right)} \tag{4.5}$$

where a is the depth of cut per workpiece revolution and D_e is the equivalent diameter as defined in Equation 4.2.

The experimental heat partition ratio to the workpiece R_w can be estimated based on theoretical heat partition ratio R_t defined by one of several relations presented in the scientific literature. In dry grinding, Hahn [83] estimates the theoretical heat partition ratio as given by

$$R_t = \frac{R_w}{R_w + R_g} = \left(1 + \frac{\kappa_g}{\sqrt{r_o V_g (\kappa\rho c)_w}}\right)^{-1} \tag{4.6}$$

where κ_g is the thermal conductivity of the abrasive grain material, r_o is the grain contact radius, and R_w and R_g are the fraction of heat conducted to the workpiece and grinding wheel, respectively, with all other variables as previously defined. The grain contact radius is a function of the abrasive grain size and wear flat area and it increases with wheel wear. Average values of the grain contact radius for grinding wheels with a grain size of 46-200 are typically in the range of 10-50 μm. However, it may not always be feasible to accurately measure the grain contact radius in practice. Rowe et al. [89] estimate the theoretical heat partition ratio to the workpiece as given by

$$R_t = \frac{R_w}{R_w + R_g} = \left(1 + \left(\left(\frac{V_w}{V_g}\right)\left(\frac{(\kappa\rho c)_w}{(\kappa\rho c)_g}\right)\right)^{1/2}\right)^{-1} \tag{4.7}$$

where $(\kappa\rho c)_g$ is the grinding wheel material thermal coefficient defined as the product of the abrasive grain thermal conductivity κ_g, density ρ_g, and specific heat c_g with all other variables as previously defined. It should be noted that the models for the theoretical heat partition ratio are conservative as they do not account for the fraction of heat energy removed by the chips and the grinding fluid.

In the grinding process, the total heat generated in the wheel-workpiece contact zone is partitioned among the workpiece, the grinding wheel, the chips, and the grinding fluid. The heat partition among these four heat sinks is given by

$$R_w + R_g + R_c + R_f = 1 \tag{4.8}$$

where R_w, R_g, R_c, and R_f are the fraction of heat conducted to the workpiece, grinding wheel, chips, and fluid, respectively. For shallow-cut grinding with very small wheel-workpiece geometric contact lengths, the effects of convective cooling on the temperatures in the grinding contact zone by the application of grinding fluid at low pressures are negligible ($R_f = 0$) [142]. In addition, it can be shown that the fraction of heat removed by the chips depends on the specific grinding energy levels in the process. The fraction of heat energy removed by the chips R_c is given by

$$R_c = \frac{e_{ch}}{e} \tag{4.9}$$

where e_{ch} is the specific energy for chip formation and e is the process specific energy. The specific energy for chip formation can be approximated as the energy required to melt the workpiece material [143] as given by

$$e_{ch} = \rho_w c_w T_m \tag{4.10}$$

where ρ_w and c_w are the density and specific heat of the workpiece material at room temperature, respectively, and T_m is its melting temperature. For the heat resistant superalloys Inconel 718 and Ti-6Al-4V, the specific energy for chip formation is 4-5 J/mm^3 and it is lower than the melting energy for many types of steels (6-8 J/mm^3). The maximum fraction of heat energy removed by the chips can be estimated by

$$R_c = \frac{\rho_w c_w T_m}{e} \tag{4.11}$$

where all the variables are as previously defined. In centerless grinding of Inconel 718 and Ti-6Al-4V alloys where the specific grinding energy levels are relatively high (20-100 J/mm^3), the fraction of heat energy conducted away by the chips is 0.05-0.25. Consequently, the great majority of the heat energy is partitioned between the workpiece and grinding wheel material. Combining Equations 4.7 and 4.11, the final expression for the experimental heat partition ratio R_w or fraction of heat energy conducted to the workpiece becomes

$$R_w = R_t\left(1 - \frac{\rho_w c_w T_m}{e}\right) \tag{4.12}$$

where all variables are as previously defined. As suggested by Equation 4.12, the fraction of heat energy removed by the chips is only significant at very low specific grinding energy levels.

For the thermal models presented in Equations 4.1 and 4.4, it has been documented that the grinding zone temperature T_c at the onset of burn is 950^{o}C for nickel-based alloys [144, 145] and 640^{o}C for Ti-6Al-4V [146]. For a more conservative prediction of the critical specific grinding energy, the fluid film boiling temperature

(~130^{o}C for water-soluble emulsions and ~300^{o}C for cutting oils) can be used as the limiting temperature for the occurrence of workpiece grinding burn.

In this analysis, the model developed by Rowe et al. [142] (Equation 4.4) is used to predict the occurrence of grinding burn for the Inconel 718 and Ti-6Al-4V workpieces and identify the burn-free operating region. To use this model, it is necessary to calibrate the fraction of heat energy entering the workpiece over the experimental range of process parameters. First, the theoretical heat partition ratio in dry grinding is found using Equation 4.7 over the range of parameters used in the experiments based on the thermal properties of the workpiece and abrasive grain materials. Typical results are shown in Tables 4.3 and 4.4 for the Inconel 718 and Ti-6Al-4V workpieces used in this study.

Table 4.3: Theoretical heat partition ratio to the workpiece in dry grinding (Inconel 718)

Grinding Wheel Speed / Workpiece Speed	20 m/s	25 m/s	30 m/s
200 mm/s	.916	.925	.931
300 mm/s	.899	.909	.916
400 mm/s	.886	.896	.905

Table 4.4: Theoretical heat partition ratio to the workpiece in dry grinding (Ti-6Al-4V)

Grinding Wheel Speed / Workpiece Speed	20 m/s	25 m/s	30 m/s
200 mm/s	.952	.957	.961
300 mm/s	.942	.948	.952
400 mm/s	.934	.940	.945

Taking into account the fraction of heat energy removed by the chips and the grinding fluid based on the grinding power measured in the process, the experimental heat partition ratio to the workpiece is estimated using Equation 4.12. Calculating the

representative chip formation energy to be ~5 J/mm^3 for the superalloys analyzed this study based on their thermophysical properties at room temperature (Table 3.1), the experimental heat partition ratios obtained for a subset of characterization experiment trials are shown in Tables 4.5 and 4.6 for Inconel 718 and Ti-6Al-4V, respectively.

Table 4.5: Experimental heat partition ratio for subset of characterization experiment trials (Inconel 718)

Grinding Wheel Speed (m/s)	Regulating Wheel Speed (m/min)	Stock Removed per Pass (μm)	Feed Rate (μm/s)	Grinding Wheel Material	Specific Grinding Energy (J/mm^3)	Exp. Heat Partition Ratio
19.1	13.4	152.4	31.6	A	42.8	0.804
19.1	13.4	152.4	38.1	A	35.8	0.783
23.9	24.5	76.2	33.1	A	38.3	0.776
23.9	24.5	76.2	24.4	A	42.4	0.788
28.7	13.4	76.2	12.6	A	64.0	0.854
28.7	13.4	76.2	12.8	A	68.8	0.859
33.5	24.5	152.4	50.1	A	38.7	0.791
33.5	24.5	152.4	49.2	A	38.5	0.790

Table 4.6: Experimental heat partition ratio for subset of characterization experiment trials (Ti-6Al-4V)

Grinding Wheel Speed (m/s)	Regulating Wheel Speed (m/min)	Stock Removed per Pass (μm)	Feed Rate (μm/s)	Grinding Wheel Material	Specific Grinding Energy (J/mm^3)	Exp. Heat Partition Ratio
19.1	13.4	152.4	18.8	A	41.2	0.834
19.1	13.4	152.4	40.3	A	34.1	0.810
23.9	24.5	76.2	21.3	A	35.5	0.806
23.9	24.5	76.2	21.8	A	36.4	0.809
28.7	13.4	76.2	24.3	A	45.3	0.852
28.7	13.4	76.2	15.2	A	60.7	0.879
33.5	24.5	152.4	49.2	A	33.0	0.804
33.5	24.5	152.4	57.3	A	31.4	0.796

As seen in Tables 4.5 and 4.6, the experimental heat partition ratio is approximately 10-15% lower than the theoretical heat partition ratio over the experimental range of grinding conditions.

To determine whether the grinding burn constraint boundary is active under the conditions shown in Tables 4.5 and 4.6, the specific grinding energy for burn (Equation 4.4) can be compared to the process energy to see if they are equal. As shown in Figure 4.3, the burn constraint is not active over the range of parameters used in the characterization experiment for the 7.94 mm (5/16 in.) diameter parts for a sharp grinding wheel and burn will not occur.

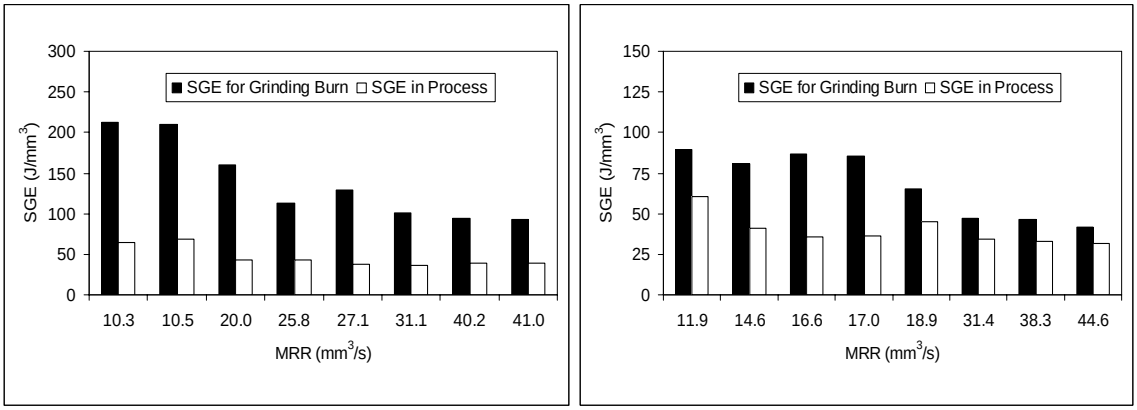

(a) Inconel 718 (WM: 2A80-O4-V) (b) Ti-6Al-4V (WM: GC120-N+-7V)

Figure 4.3: Specific grinding energy in the process and at the burn limit

The grinding power for a worn wheel after conducting 250 passes was observed to be ~1 kW greater than the power at the beginning of the production run. The corresponding value of specific grinding energy after 250 grinding passes also does not exceed the specific grinding energy for burn established by the model in Equation 4.4 under the same grinding conditions. After grinding 250 parts, the process specific energy increases

by a factor of ~1.5 from the specific energy at the beginning of the production run for both workpiece materials. However, as seen in Figure 4.3, the specific grinding energy can increase by up to 3-4 times for Inconel 718 and 1.5-2 times for Ti-6Al-4V before encountering the grinding burn constraint.

To verify the predictions of the theoretical model for workpiece burn, the workpiece surface quality can be inspected for thermal damage both visually and in the metrology lab after the grinding operation by measuring the workpiece surface hardness or conducting metallurgical examinations of the workpiece cross-section. However, even though the model may predict the occurrence of grinding burn during the material removal stage for a particular combination of parameters, thermal damage may still not occur in practice since the depth of the burn layer is often removed during spark-out where the elastic deflections of the machine tool system are recovered and where the depth of cut per workpiece revolution diminishes to a very small value approaching zero (stationary system). Alternatively, the occurrence of thermal damage may also be verified by measuring the transient workpiece temperature field during the process to see if the temperatures for the onset of burn are reached using high-speed IR imaging. For all the experimental trials conducted in this study, no grinding burns marks were visually detected on the workpiece surface and no notable changes in the surface hardness were measured from the original condition after the operation. These results are not surprising considering that the contact time of the abrasive grains with the workpiece during the material removal stage and the cooling time during spark-out are very short in this shallow-cut grinding operation.

4.3.3 Dimensional Tolerances and Surface Finish

In the finish grinding operation, the active process constraints are the part surface finish requirement of 0.81 μm (32 μin.) along with the final dimensional accuracy as prescribed by the typical tolerance ranges shown in Table 4.7 for the fastener diameter, taper, transition radii, and roundness.

Table 4.7: Typical dimensional tolerance constraints for fastener grinding operation

Dimensional Characteristic	Tolerance Range
Diameter	$\pm$ 6.35 μm ($\pm$ 0.00025 in.)
Out-of-Roundness	5.08 μm (0.00020 in.)
Head-to-Shank Transition Radius	76.2 μm (0.003 in.)
Grip-to-Thread Transition Radius	25.4 μm (0.001 in.)
Head Angle	$\pm 0.5^{o}$
Taper	$\pm$ 6.35 μm ($\pm$ 0.00025 in.)

Most of the dimensional characteristics in Table 4.7, including out-of-roundness and taper, cannot be constrained by a practical deterministic model as they depend on a complex combination of machine setup parameters, dressing parameters, and random variations in workpiece and regulating wheel geometry prior to the grinding operation.

The only dimensional characteristic that was constrained by a deterministic model is the part diameter, and its size deviation from the target dimension was quantified by the diameter error (DE). Under stable grinding conditions with a sharp grinding wheel that has not undergone any radial wear, the final diameter error is determined by how quickly the machine tool system recovers elastically during the spark-out stage from the cutting forces applied during the grinding stage to reduce the magnitude of the

accumulated workpiece radial deflection and complete the intended grinding pass. According to Rowe [141], the depth of cut at the end of the spark-out stage is related to the depth of cut at the beginning of the spark-out stage as given by

$$a_f = a_i (1 - K)^n \tag{4.13}$$

where a_f is the final depth of cut at the end of spark-out, a_i is the initial depth of cut at the beginning of spark-out, K is the machining elasticity parameter, and n is the number of workpiece half-revolutions completed during spark-out. The number of full workpiece revolutions N completed during spark-out is a function of the workpiece speed V_w, spark-out time t_s, and workpiece diameter D_w as given by

$$N = \frac{1}{2} n = \frac{V_w t_s}{\pi D_w} \tag{4.14}$$

Substituting Equation 4.14 into 4.13 and rearranging the resulting expression, the time required to achieve a specified final depth of cut during spark-out becomes

$$t_s = \frac{1}{2 N_r} \left(\frac{D_w}{D_r} \right) \left(\frac{\ln\left(\frac{a_f}{a_i} \right)}{\ln(1 - K)} \right) \tag{4.15}$$

where t_s is the spark-out time, D_w is the workpiece diameter, N_r is the regulating wheel rotational speed in rev/min or rev/s, D_r is the regulating wheel diameter and all other parameters are as previously defined. The machining elasticity parameter K, defined as the ratio of the actual depth of cut at the end of the grinding stage to the applied or set depth of cut at the beginning of the grinding stage, is unique for each combination of machine tool and workpiece material and can be estimated by an analysis of the infeed or spark-out signal using a power meter according to the method described by Rowe [141],

where typical values range from 0.1 to 0.4. When grinding Inconel 718 and Ti-6Al-4V on the machine tool used in this study, the range of values obtained for the elasticity parameter according to Rowe's method was 0.05-0.20. This range of values is not surprising, especially for Ti-6Al-4V which has a relatively low modulus of elasticity. Equation 4.15 can be used to impose a constraint on the diameter dimension under stable grinding conditions and optimize the value of spark-out time, which is a very significant fraction of the overall cycle time in shallow-cut centerless grinding.

4.4 Feasible Operating Region Mapping

From the analysis presented in the previous section, it is evident that the machine tool spindle power and workpiece grinding burn constraints are not active over the range of grinding parameters used in the characterization experiment in Chapter 3. Consequently, the only active process constraint boundaries that should be mapped to identify the feasible operating region are those defining the surface roughness and dimensional tolerance requirements. However, in many grinding operations, most or all of the aforementioned process constraints can be simultaneously active. In this section, a numerical example is carried out to demonstrate how the map of the feasible operating region can be generated under the assumption that all of the relevant process constraints are active.

In this numerical example, it is assumed that the active constraints for an Inconel 718 grinding operation are a grinding burn power limit of 5 kW, part surface roughness limit of 0.81 μm (32 μin), and a diameter error (DE) of 2.54 μm (0.0001 in) for a machine

tool system with an elasticity parameter K of 0.2. Placing a strict limit on the final diameter error as is the case in this example can be done to also meet the workpiece roundness requirement (Table 4.7). Under stable grinding conditions with a perfectly round workpiece profile, the final theoretical out-of-roundness should be equal to the depth of cut per workpiece revolution at the end of the spark-out stage. To define the feasible operating region, the constraint boundaries are plotted in the x-y plane defined by the depth of cut per workpiece revolution a and workpiece speed V_w over the experimental range of grinding parameter values using the models presented in the previous section. A summary of the parameters that are held constant when mapping the feasible operating region for the 7.94 mm (5/16 in.) diameter Inconel 718 part is shown in Table 4.8.

Table 4.8: Process parameters for mapping the active constraint boundaries

Dressing Overlap Ratio	Grinding Wheel Speed (m/s)	Stock Removed per Pass (μm)	Grinding Wheel Material	Spark-Out Time (s)	Machining Elasticity Parameter
2.36	31.9	127	A	0.5, 1.0, 1.5	0.2

The feasible operating region bounded by process constraints where the grinding parameters can be selected to meet the imposed requirements is shaded in Figure 4.4 under the assumption that the surface roughness constraint is not active for a rough grinding operation.

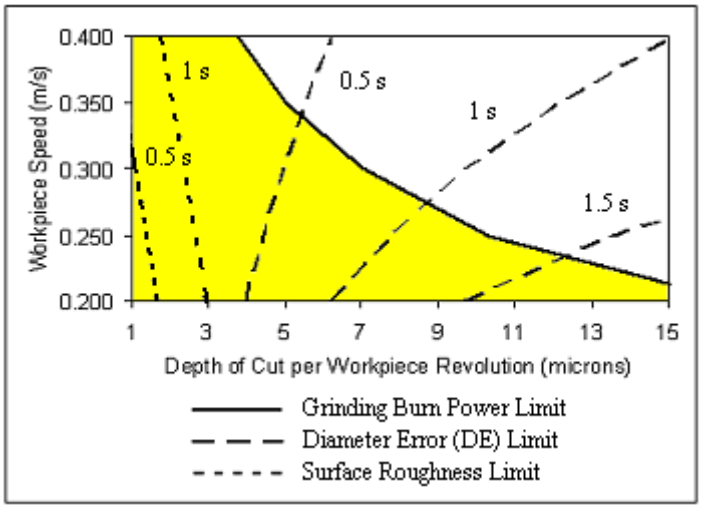

Figure 4.4: Feasible operating region defined in depth of cut vs. workpiece speed plane

As seen in Figure 4.4, several possible combinations of workpiece speed V_w and depth of cut per workpiece revolution a can be selected within the feasible operating region to produce a part that meets the imposed quality requirements. The optimum combination of parameters to be identified in the region is the one that yields the lowest grinding operation costs.

4.5 Economic Simulation Algorithm

In any machining optimization problem, the primary objective is to find the combination of parameters that maximizes the production output or minimizes the production cost per part in the operation. In this section, an algorithm is developed to find the cost-optimum parameters when taking into account the effects of wheel wear and other time factors encountered in the production environment. The minimum cost per

part is found by identifying the cost-optimum material removal rate when all the cost components in the process are taken into account as shown in Figure 4.5.

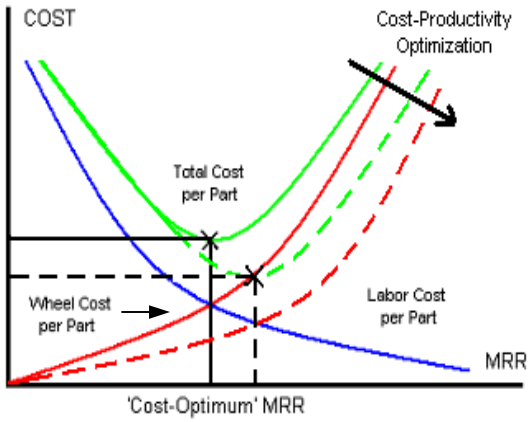

Figure 4.5: Grinding process optimization strategy

As seen in Figure 4.5, the total cost per part in grinding is the sum of the wheel cost and labor cost per part. If a production run is conducted at a very low value of material removal rate, the labor cost per part will be too high due to excessively high grinding cycle times. Conversely, if a production run is conducted at a very high material removal rate, wheel cost per part will be too high due to excessive wheel consumption by wear and subsequent dressing. Consequently, there exists an optimum operating point where the wheel cost and labor cost per part are both minimized, defined as the 'cost-optimum' material removal rate. Figure 4.5 illustrates how the cost-optimum point is shifted to a higher value of material removal rate to increase productivity by the selection of a superior grinding wheel. A grinding wheel with improved wear characteristics is expected to process a higher number parts between dressings and require a lower dressing frequency, which will reduce the wheel cost per part.

In order to minimize the total cost per part in production grinding, it is necessary to minimize the individual cost components attributed to both the wheel cost and labor cost per part. The wheel cost and labor cost per part can be derived based on the different grinding production cycle time parameters as summarized in Table 4.9.

Table 4.9: Typical components of wheel cost and labor cost per part in production

Labor Cost per Part	Wheel Cost per Part
Part transfer time	Unit wheel cost
Machine setup time	Number of wheels required
Wheel dressing time	Number of parts per dress
Part loading time	
Grinding time	
Part unloading time	
Part inspection time	
Break time	
Log recording time	

The simulation algorithm developed using machining economics theory to find the cost-optimum operating point in the feasible operation region is shown in the flow chart in Figure 4.6.

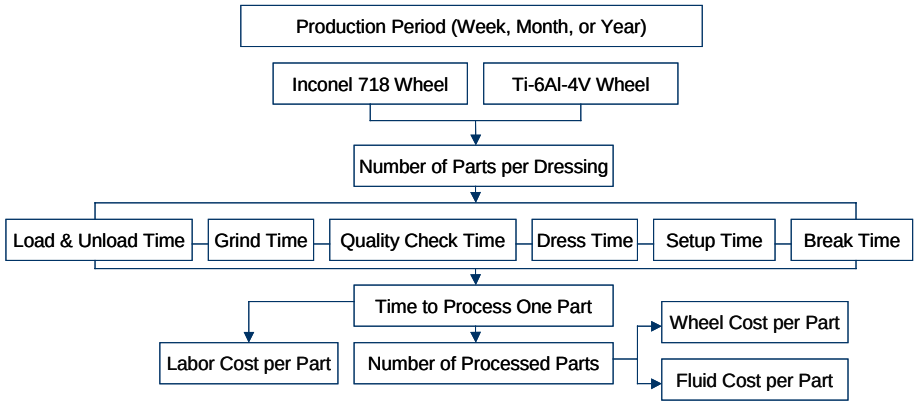

Figure 4.6: Flow chart of economic simulation algorithm

To identify the cost-optimum operating point in the feasible operating region for any production run, the simulation algorithm shown in Figure 4.6 requires two sets of inputs. These inputs are the time data recorded for a typical grinding production cycle sequence and the regression models for wheel wear obtained in the production run experiment for the data extracted at the 250^{th} grinding pass (Chapter 3). The simulation begins by entering information about the workpiece (i.e. material, part dimensions), grinding wheel (i.e. unit cost), dressing parameters (i.e. dressing overlap ratio) and machining parameters (i.e. grinding wheel speed, regulating wheel speed). The next step is to enter the time data for the typical production stages conducted in sequence, including part transfer time, machine setup time, initial wheel dressing time, loading time, unloading time, and part inspection time. The data is used to compute the time to process one part, which can then be used to estimate the number of parts processed over the specified production period and find the wheel and labor cost incurred for each part. For this analysis, it is necessary to specify the production period along with the batch size (250 parts) to perform the repeated batch production simulation. The diameter error (DE) was used as the primary wear indicator because it is less sensitive to changes in setup parameters relative to the transition radius error. The standard equations used for the economic simulation are summarized in Appendix E.

A sample simulation was carried out using the cycle time inputs summarized in Table 4.10 to compute the total cost per part over the entire range of material removal rates bounded by the feasible operating region shown earlier in Figure 4.4. The results of the simulation are illustrated for material removal rates ranging from 10 mm^3/s to 80 mm^3/s in Figure 4.7.

Table 4.10: Grinding process data for economic simulation

Workpiece Material	Inconel 718
Part Diameter and Length	7.94 mm (5/16 in.), 63.5 mm (2.5 in.)
Batch Size	250 parts
Production Period	1 week
Grinding Wheel Cost	$400/unit
Grinding Fluid Cost	$20/gallon
Grinding Wheel Speed	31.9 m/s
Regulating Wheel Speed	13.4 m/min
Part Diameter Reduction	127 μm (0.005 in.)
Part Transfer Time	10 min
Machine Setup Time	60 min
Initial Wheel Dressing Time	15 min
Loading Time per Part	5 s
Spark-Out Time per Part	3 s
Unloading Time per Part	5 s
Part Inspection Frequency	Once every 10 parts (5 min per part)
Break Time	15 min
Data Recording Time	15 min

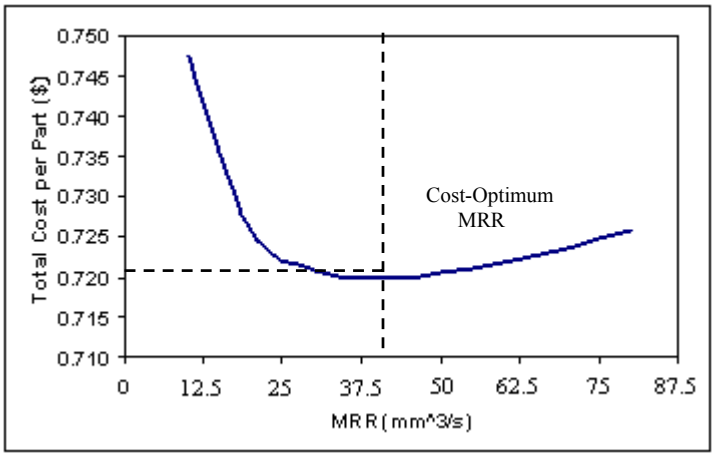

Figure 4.7: Sample plot for identifying cost-optimum material removal rate

From Figure 4.7, it is evident that the production run should be conducted at a material removal rate of ~42 mm^3/s in order to minimize the total cost per part. For the constant values of grinding wheel speed (31.9 m/s) and regulating wheel speed (13.4

m/min) selected to maximize the cutting speed ratio and thus minimize the rate of wheel wear, the optimum operating point corresponds to a feed rate of ~52 μm/s (~0.124 in./min). The simulation in Figure 4.4 may be repeated for different production cycle time data values in order to investigate other potential ways to reduce total cost per part in addition to operating at the optimum material removal rate.

The proposed methodology, which focuses only on the major controllable process parameters, can be used to benefit grinding process productivity in many ways. First, it can be used as a practical and cost-effective alternative to more data-intensive optimization approaches. Centerless grinding is inherently a stochastic process where a large number of variables affect process performance, and more complex optimization approaches do not guarantee reproducible solutions in practice. In addition, it is relatively simple to evaluate the significance of each cost factor in the operation using the methodology outlined in this study in order to facilitate and guide decision making for future optimization efforts at the system level.

4.6 Verification of Optimum Parameters on CNC Centerless Grinder

The productivity under the optimum parameters identified by the simulation was evaluated for several trial runs on a CNC grinder. The CNC grinder offers greater capability for grinding cycle optimization than the manual grinder since it allows the operator to set the feed rate and regulating wheel speed for each of the 3 separate material removal stages (rough, semi-finish, finish) in the grinding cycle illustrated in Figure 4.8. Having control of these parameters over each stage, the operator can simultaneously meet

multiple part quality requirements and eliminate the need for separate rough and finish passes. On a CNC grinder, the grinding cycle is defined by three material removal stages (roughing, semi-finishing, finishing) and two dwell or spark-out stages where the infeed motion is stopped and where material removal continues at a decreasing rate until the machine tool system returns to its original position.

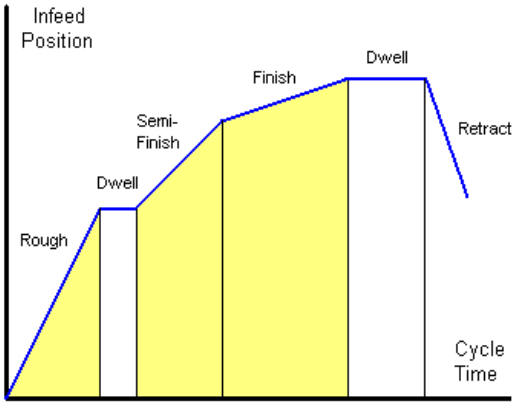

Figure 4.8: CNC grinding cycle stage sequence

In order to minimize the grinding cycle time and maximize part output for any grinding pass, the operator can follow the general feed control strategy outlined in Table 4.11, taking into consideration the grinding behavior of each material. For Inconel 718, which responds more favorably to high feed rates relative to Ti-6Al-4V, the first step is to complete 70-85% of the stock removal in the first roughing stage at a high feed rate that does not violate the spindle power or part thermal damage constraints. In case the thermal damage limit is exceeded in the first roughing stage, the second step is to select softer machining parameters for the intermediate semi-finish stage that will remove the grinding burn layer (i.e. lower feed rate, lower grinding wheel speed, etc.). The last step

is to complete the remaining 5-10% of stock removal at a low feed rate (~25% of high feed rate value) to meet the dimensional tolerance, roundness, and surface roughness requirements. Completing the last stock removal stage at a sufficiently low feed rate will ensure that little or no spark-out time is needed at the end of the cycle, which will have a positive impact on the overall cycle time. For Ti-6Al-4V, the stock removal should be distributed more evenly with more uniform and less aggressive feed rates across the stages, since material adhesion to the grinding wheel is more pronounced at high cutting temperatures. In turn, more effective control of cutting temperatures will minimize dimensional inaccuracies associated with grinding wheel loading as encountered in the production run experiment (Chapter 3).

Table 4.11: General feed control strategy for grinding cycle optimization [42]

Stage	Active Constraint(s)	Inconel 718	Ti-6Al-4V
Rough	machine spindle power, part thermal damage	70-85% stock removed, high feed rate	40-55% stock removed, medium feed rate
Semi-Finish	corrective step for rough stage violations	10-20% stock removed, medium feed rate	30-40% stock removed, medium feed rate
Finish	surface finish, tolerances, roundness	5-10% stock removed, medium feed rate	15-20% stock removed, medium feed rate

The optimum material removal rates identified for the single-stage manual grinder by the simulation for different part sizes were converted to corresponding feed rates and used for the roughing stage on the multi-stage CNC grinder. The feed rates for the remaining stages were selected according to the recommendations in Table 4.11 if the corresponding material removal rate value for that stage did not fall in the low-efficiency material removal rate range (less than 20 mm^3/s) identified in Chapter 3. Otherwise, they

were kept the same as in the roughing stage. The grinding wheel and regulating wheel speeds were set at the maximum (31.9 m/s) and minimum value (13.4 m/min) respectively, for the roughing and semi-finishing stages to minimize the value of equivalent chip thickness, which reduces the rate of wheel wear and prolongs the dressing interval as seen by the production run trends analyzed in Chapter 3. The regulating wheel speed was increased for the finishing stage to minimize the final spark-out time according to the diameter error model presented earlier in Equation 4.15. A summary of the grinding productivity under the optimum parameters identified in the simulation for several production runs on the CNC grinders is shown Table 4.12.

Table 4.12: CNC grinding productivity under the cost-optimum process parameters

Material	Part Length (in.)	Part Diameter (in.)	Stock Removed per Pass (in.)	Cycle Time (s)	Parts per Dress	Feed Rates (in./min)
Inco 718	2.8060	0.4440	0.0060	12.1	130	.200/.100/.050
Inco 718	2.7560	0.5060	0.0063	11.8	200	.225/.125/.040
Inco 718	2.7430	0.4410	0.0049	11.5	110	.210/.110/.035
Inco 718	2.8060	0.7665	0.0125	12.7	100	.250/.150/.100
Ti-6Al-4V	1.9540	0.6320	0.0080	13.0	850	.130/.130/.080
Ti-6Al-4V	1.3080	0.5430	0.0380	18.2	50	.250/.150/.075
Ti-6Al-4V	1.7230	0.3250	0.0120	12.2	175	.160/.160/.060
Ti-6Al-4V	1.4750	0.3855	0.0084	11.9	750	.130/.090/.090

Prior to implementing the optimum parameters, the typical average cycle time per part for four different Inconel 718 and Ti-6Al-4V obtained in typical rough pass production runs was 15.1 s and 15.8 s, respectively. Using the optimum process parameters in Table 4.12, the average cycle time per part for the same Inconel 718 and Ti-6Al-4V rough pass production runs was 12.0 s and 13.8 s, which corresponds to a time reduction of 21% and 13%, respectively. In most cases, no losses in wheel performance

were observed using the more aggressive feed rates as indicated by the number of parts processed between dressings. The gains were typically greater for Inconel 718 because it responded more favorably to higher feed rates than Ti-6Al-4V, but in general, the wheel performance was not satisfactory for large diameter parts for either workpiece material. This suggests that a wheel with different specifications would be better suited for higher volumes of stock removal. The regression models for wheel wear developed in Chapter 3 worked reasonably well over the range of experimental values considering the fact that they cannot accurately quantify wheel wear for each stage on a CNC grinder and predict which dimensional tolerance will first diverge outside the prescribed range. In production, the variance of any particular tolerance is best monitored and analyzed using statistical methods since each individual part dimension varies with a very large number of setup parameters and random part non-uniformities inherited from previous stages of the manufacturing process.

4.7 Conclusions

In this chapter, a methodology was developed and illustrated using numerical examples to find the optimum grinding parameters in a plunge centerless grinding operation. The key step in this methodology is the application of a model-based strategy to identify the feasible operating region where the grinding parameters can be selected without violating machine tool or part quality constraints. After identifying the parameters bounded by the feasible operating region, a simulation algorithm was developed using machining economics theory to find the corresponding optimum

operating conditions. The simulation can be repeated for different production cycle time data inputs, and it highlights all the important cost factors for any grinding operation to facilitate decision making for future optimization planning.

The following key conclusions can be made based on the results of this study:

- For Inconel 718 and Ti-6Al-4V workpieces with diameters ranging from 7.94 mm (5/16 in.) to 25.4 mm (1 in.), the cost-optimum material removal rate in rough grinding using the wheels evaluated in this study was determined to be in the range of ~40-100 mm^3/s corresponding to a specific material removal rate of 0.6-1.6 mm^2/s.
- Grinding Inconel 718 and Ti-6Al-4V at the optimum parameters is expected to reduce the total cost per part by up to $0.05 for the grinding wheels used in this study under the conditions assumed in the simulation analysis.

One of the key cost factors not explicitly accounted for in the simulation study is the cost of grinding fluid use, which typically makes up a significant fraction of the overall cost of the grinding operation. In the next chapter, the application of a grinding fluid enhanced with graphite nanoplatelets is evaluated as another potential method for improving the productivity and reducing the costs of the superalloy centerless grinding operation.

CHAPTER 5

PERFORMANCE OF GRAPHITE NANOPLATELET-ENHANCED FLUIDS IN REDUCED QUANTITY LUBRICATION CENTERLESS GRINDING

5.1 Introduction

Centerless grinding of Inconel 718 and Ti-6Al-4V superalloys is a very inefficiently conducted operation that generates a very significant amount of energy (20-100 J/mm^3) during the material removal process. The great majority of this material removal energy is transmitted to the workpiece as heat, which can have an adverse effect on its surface integrity and final dimensional accuracy. In order to minimize the risk of part thermal damage, it is necessary to reduce the grinding temperatures, which can generally be accomplished by (1) reducing the amount of heat generation using a softer grinding wheel at reduced speeds, (2) dressing the wheel more frequently to maintain the sharpness of the grains and to prevent wheel loading, and (3) enhancing heat removal with more effective grinding fluid application. Among these solutions, the optimization of fluid application parameters is the only feasible method to increase productivity without incurring higher abrasive consumption costs and longer cycle times.

In many industrial grinding operations, the most common method of fluid application is low-pressure flood cooling (5-50 L/min) using cutting or water-soluble oils. Although this fluid application method provides satisfactory workpiece bulk material cooling and chip removal, it is generally ineffective at reducing temperatures in the

wheel-workpiece contact zone in most conventional grinding processes. First, low pressure flood cooling is ineffective because only a small fraction of the applied flow (5-20%) reaches the wheel-workpiece contact interface due to the non-coherence of fluid flow leaving the nozzle and the dispersion of the fluid jet by the dense air boundary layer surrounding the rotating grinding wheel [147]. Second, even the small quantity of fluid that reaches the contact zone does not have a significant effect on the grinding temperatures, especially under more aggressive operating conditions where the fluid may be squeezed out by the greater contact loads and where fluid film boiling is more likely to occur. In addition to being ineffective, high-volume flood cooling using cutting or water-soluble oils also raises major environmental concerns and is an uneconomical method of fluid application due to high fluid maintenance and disposal costs [109].

Several fluid types and application methods were shown to be superior to flood cooling using oils in improving the performance of grinding processes, including cryogenic cooling using liquid nitrogen [102], soap mist jet cooling [105], and minimum quantity lubrication (MQL) using air-oil mixtures delivered to the grinding zone using high-pressure nozzles at flow rates of 50-500 mL/hr [148-150]. MQL in particular has also shown promising results in many traditional machining operations, including milling, drilling, and turning [151-153].

In addition to MQL, some researchers have also tried to use solid lubricants in grinding processes. The solid lubricants that have been used most frequently in high-temperature grinding operations include graphite [103, 104, 154] and molybdenum disulfide [107, 155]. In most cases, they are used in the form of nano-sized particles and dispersed as additives in a carrier fluid by ultrasonication or milling. They can also be

used in powder or paste form to manually coat the surface of the grinding wheel, but this application method is inconsistent and it does not ensure adequate cleaning of the wheel surface. Other solid compounds that have been tried in different machining operations include boron nitride, polytetrafluoroethylene (PTFE), calcium fluoride, and tungsten disulfide [155]. However, to date, no studies have been reported on the use of solid lubricants such as graphite nanoplatelets in centerless grinding. It is generally more difficult to achieve effective fluid application in shallow-cut plunge centerless grinding in comparison to more conventional operations such as surface grinding due to the smaller length of the wheel-workpiece contact arc and the unconstrained rounding motion of the workpiece that can disrupt the fluid film continuity in the grinding gap.

The effectiveness of graphite lubricant can be attributed to its layered structure shown in Figure 5.1, which consists of a hexagonal arrangement of carbon atoms that form stable planar lattices held by strong covalent bonds that provide resistance to plastic deformation against normal forces. The parallel planes in the structure are held together by weak Van der Waals bonds that are easily broken by the tangential force parallel to the film layer, causing interlayer slipping with a very low coefficient of friction [156].

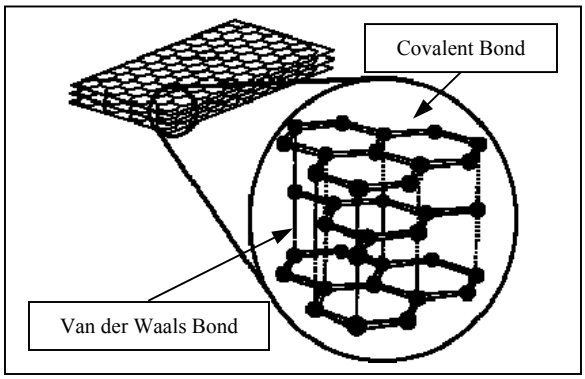

Figure 5.1: Crystalline structure of graphite nanoplatelets [156]

In the grinding process, the lubrication performance of fluids containing a solid lubricant is affected by many other factors in addition to the particle morphology. This chapter discusses an experimental investigation conducted to quantify the effects of graphite nanoplatelet diameter and concentration dispersed in an industrial cutting oil on the specific grinding energy in reduced quantity lubrication (RQL) centerless grinding of Inconel 718 and Ti-6Al-4V superalloys. The parameter combination corresponding to the best lubrication condition is selected to compare wheel wear performance to the flood cooling method.

5.2 Experimental Procedure

In this work, the performance metrics used to compare the effectiveness of fluid application are the specific grinding energy and the wheel wear rate (quantified by the grinding ratio or G-ratio). In the first part of the study, an experiment was conducted to evaluate the performance of a graphite nanoplatelet-enhanced fluid in reduced quantity lubrication (100 mL/min) using the specific grinding energy as an indicator of material removal efficiency. In this experiment, the effects of graphite platelet diameter and graphite concentration by weight on the specific grinding energy levels were investigated at three different material removal rates in plunge centerless grinding of 7.94 mm (5/16 in.) diameter Inconel 718 and Ti-6Al-4V workpieces. The experimental results were compared to the results obtained using the same grinding fluid without any solid lubricant additive under flood cooling (5 L/min) and dry grinding conditions.

For all experimental trials, the grinding parameters were held constant as summarized in Table 5.1. A 609.6 mm (24 in.) diameter ceramic sol-gel (SG) grinding wheel (3SGP80-O6-VH) and a silicon carbide wheel (74C120-O6-VK) utilized in previous experiments (Chapter 3) were selected to grind the Inconel 718 and Ti-6Al-4V workpieces, respectively.

Table 5.1: Summary of grinding conditions

Process Parameter	Setting
Grinding Wheel Speed	33.5 m/s
Regulating Wheel Speed	13.4 m/min
Diameter Reduction per Pass	127 μm
Feed Rate(s)	19.5 μm/s, 39.1 μm/s, 78.2 μm/s

The low, medium, and high feed rate settings in Table 5.1 used to reduce the diameter of the original 7.94 mm (5/16 in.) part by 127 μm in a single rough grinding pass correspond to volumetric material removal rates of 15.4, 30.9, and 61.9 mm^3/s, respectively. For a grinding width equal to the part length of 63.5 mm (2.5 in.), the corresponding specific material removal rates are 0.243, 0.487, and 0.975 mm^2/s.

The carrier fluid selected for dispersion and transport of the graphite nanoplatelets was Castrol ALMACUT 7210 cutting oil, a water-insoluble cutting oil with a density of 0.985 g/cm^3, kinematic viscosity of 60 mm^2/s (60 cSt) at 40°C, and boiling temperature of ~300°C. Graphite nanoplatelets with the trade name xGnP™ (XG Sciences, East Lansing, Michigan) were used as the solid lubricant additive in this study. They are made from synthetic, acid intercalated graphite based on the microwave exfoliation method. The xGnP-1 and xGnP-15 graphite nanoplatelets used in the experiments have an average diameter of 1 μm and 15 μm, respectively, as shown in Figure 5.2a. The

average thickness of a platelet consisting of 10-15 sheets is approximately 5-10 nm as shown in the SEM images in Figure 5.2b. The platelets have a large surface area of ~60 m^2/g and they retain their properties at temperatures of up to 450-500^oC.

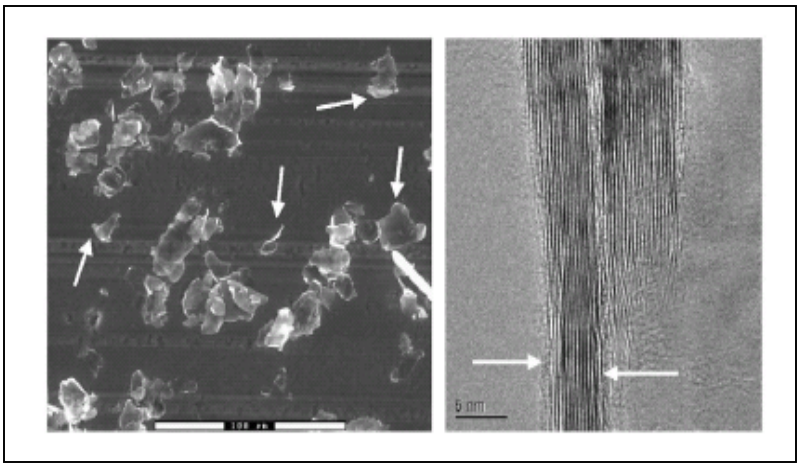

Figure 5.2: SEM micrographs of (a) xGnP-15 graphite nanoplatelets (scale bar: 100 μm) and (b) xGnP-1 graphite nanoplatelets (scale bar: 5 nm) [157]

The first experiment conducted to evaluate the performance of a graphite nanoplatelet-enhanced fluid in reduced quantity lubrication (100 mL/min) based on specific grinding energy metric consisted of 4 randomized runs for each workpiece material. Two graphite platelet diameters (1 μm and 15 μm) and concentrations (1% and 2% by weight) were used as the experimental parameters. The graphite concentration was selected outside the lower end of the range of values recommended by the graphite supplier (5-40%) when using grease as the transport medium. The sequence of experimental trials is summarized in Table 5.2. Each trial was repeated twice at three different feed rates while holding all other parameters constant as shown in Table 5.1. The grinding wheel was redressed between trials with a Vertex V2-O single point diamond using a dresser traverse rate of

4.23 mm/s (10 in./min) and a dressing depth per pass of 25.4 μm (0.001 in.) to maintain the same wheel surface condition for each pass. The results were averaged to obtain a representative value of the measured response.

Table 5.2: Summary of experimental parameters

Experimental Trial	Platelet Diameter	Concentration by Weight
1	1 μm	1%
2	1 μm	2%
3	15 μm	1%
4	15 μm	2%

In the second part of this study, the best combination of parameters identified from the first experiment was selected to perform a short production run and compare wheel wear performance as quantified by the G-ratio for reduced quantity lubrication using the cutting oil enhanced with graphite nanoplatelets to the wear performance obtained using the same fluid without graphite in flood cooling. The production run was performed for each workpiece material at the medium feed rate setting of 39.1 μm/s, and the wheel speed was set to 19.1 m/s for softer cutting action in order to increase the rate of radial wheel wear, thus making it easier to measure. All other process parameters were held constant as shown in Table 5.1.

5.3 Experimental Setup and Measurements

The dispersion of graphite nanoplatelets in the oil was carried out using a Misonix Sonicator S-4000 with a probe diameter of 12.7 mm (0.5 in.). After determining the

appropriate concentration, the graphite was added to the fluid and the solution was mixed for 45 minutes at an amplitude of 35% (55-65 W) to increase the energy of the system to ~100-150 kJ. The mixture was used for the trials immediately after the dispersion procedure in order to avoid agglomeration and precipitation of the graphite platelets. The grinding tests were carried out on a Cincinnati OM-2 centerless grinder with a 15-hp grinding wheel spindle motor. The grinding fluids were applied by manually spraying the wheel-workpiece contact zone using a common industrial mist spray bottle calibrated to a flow rate of 100 mL/min. During the experimental trials, the nozzle of the spray bottle was positioned approximately 50.8 mm (2 in.) from the grinding zone as illustrated in Figure 5.3.

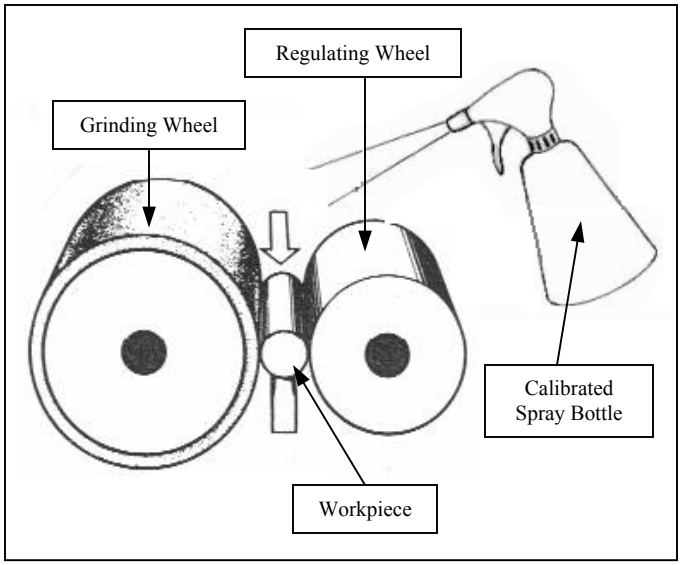

Figure 5.3: Schematic of experimental setup for fluid application

The process responses measured during the experiments were the grinding power and the part diameter. The grinding cycle power was measured using a Load Controls UPC model power meter connected to the wheel spindle motor as described in Chapter 3

(Figure 3.4). The measured grinding power was divided by the material removal rate to determine the specific grinding energy in the process. The critical part dimension (diameter) was measured using a 2.54 μm (0.0001 in.) resolution micrometer. The deviation of the part diameter from the original target dimension was recorded to monitor the wheel wear trend and the final value recorded after the 250th grinding pass was used to quantify the accumulated volume of wheel radial wear for the entire production run.

5.4 Results and Discussion

5.4.1 Comparison of Specific Grinding Energy Levels

The average specific grinding energy (SGE) obtained for each trial with graphite nanoplatelet additives over the experimental range of material removal rates are given in Appendix C and summarized in Tables 5.3 and 5.4 for Inconel 718 and Ti-6Al-4V, respectively. These tables also contain the results obtained in dry grinding and flood cooling conditions (5 L/min) using the same fluid without the graphite additive.

Table 5.3: Specific grinding energy levels under different lubrication conditions (Inconel 718)

Parameter Combination	SGE at 15.4 mm^3/s (J/mm^3)	SGE at 30.9 mm^3/s (J/mm^3)	SGE at 61.9 mm^3/s (J/mm^3)
1 μm, 1 wt%	59.1± 3.0	39 ± 3.4	21.7 ± 4.0
1 μm, 2 wt%	59 ± 3.1	38 ± 3.2	20.4 ± 3.2
15 μm, 1 wt%	54.5 ± 2.9	35.8 ± 3.0	20.4 ± 3.2
15 μm, 2 wt%	50.2 ± 2.4	32.5 ± 2.5	20.2 ± 3.5
Flood	61.7 ± 1.5	39.5 ± 3.0	21.9 ± 3.3
Dry	80.7 ± 2.2	47.3 ± 3.8	25.6 ± 4.2

Table 5.4: Specific grinding energy levels under different lubrication conditions (Ti-6Al-4V)

Parameter Combination	SGE at 15.4 mm^3/s (J/mm^3)	SGE at 30.9 mm^3/s (J/mm^3)	SGE at 61.9 mm^3/s (J/mm^3)
1 μm, 1 wt%	69.9 ± 2.5	44.9 ± 2.6	25.2 ± 2.2
1 μm, 2 wt%	68.8 ± 2.4	44.5 ± 2.3	25.0 ± 2.2
15 μm, 1 wt%	63.7 ± 2.4	42.7 ± 2.2	24.3 ± 2.0
15 μm, 2 wt%	61.2 ± 2.5	41.3 ± 2.3	24.1 ± 2.1
Flood	71.9 ± 2.8	46.7 ± 3.5	25.5 ± 3.8
Dry	90.0 ± 3.5	52.6 ± 4.2	28.0 ± 5.0

The results presented in Tables 5.3 and 5.4 are illustrated in Figures 5.4 and 5.5 for Inconel 718 and Ti-6Al-4V, respectively, which compare the specific grinding energy values obtained under each condition. In these figures, the error bars represent the range of deviation from the average specific grinding energy obtained for the two grinding passes carried out using each combination of parameters.

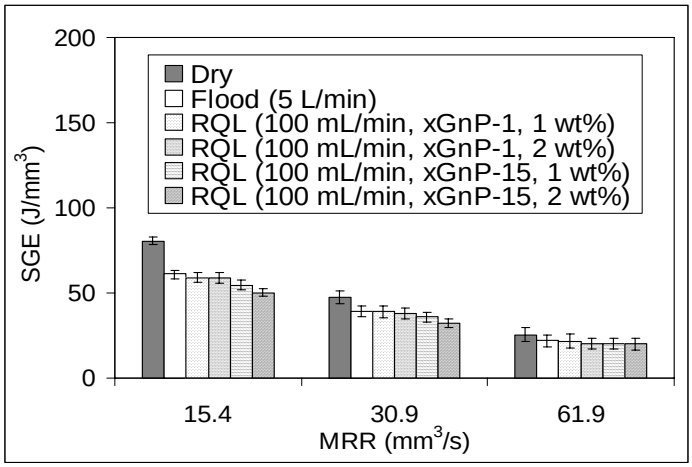

Figure 5.4: SGE levels in dry grinding, flood cooling, and graphite nanoplatelet-enhanced RQL conditions (Inconel 718)

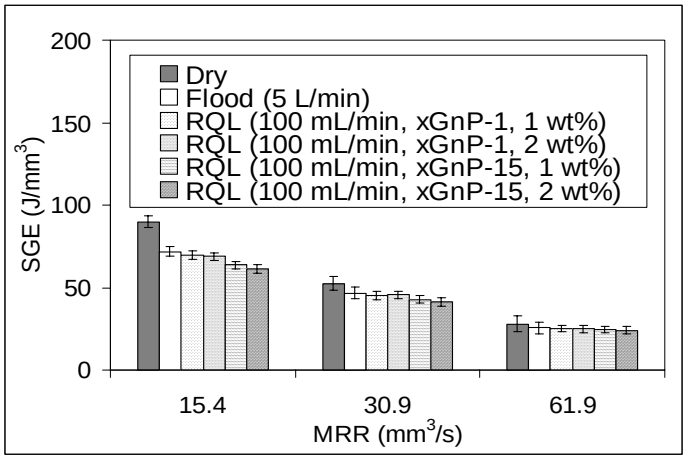

Figure 5.5: SGE levels in dry grinding, flood cooling, and graphite nanoplatelet-enhanced RQL conditions (Ti-6Al-4V)

Comparing the results in Figures 5.4 and 5.5, it can be seen that the application of a graphite nanoplatelet-enhanced cutting oil at a reduced flow rate (100 mL/min) was more effective at reducing the specific grinding energy than flood cooling (5 L/min) using the same fluid without graphite additives. Specifically, reduced quantity lubrication using the cutting oil enhanced with 15 μm graphite nanoplatelets at a 2% concentration by weight reduced the specific grinding energy by 19% at the lowest material removal rate and by 8% at the highest material removal rate over flood cooling for Inconel 718. The corresponding reductions in specific grinding energy for Ti-6Al-4V were 15% and 5% at the lowest and highest material removal rates, respectively. For both workpiece materials, the lowest specific grinding energy corresponding to the best lubrication condition was achieved using the larger platelet diameter (15 μm) in combination with the higher graphite concentration (2 wt%).

As seen in Tables 5.3 and 5.4, the lubrication performance improves with a larger graphite nanoplatelet diameter as noted by the more significant reductions in specific

grinding energy when using the 15-μm diameter platelet. It can also be seen that the nanoplatelet diameter had a greater effect on the specific grinding energy than the additive concentration. Larger platelets have a greater surface area to cover the asperities of the surfaces in contact and they yield better lubrication performance for coarser surfaces, while smaller platelets are better suited for lubricating smoother surfaces moving at higher speeds. Another potential benefit of using platelets with a larger surface area over smaller platelets is their greater flexibility, which permits bending under higher contact pressures exerted by higher feed rates. Even though the specific grinding energy is reduced more effectively when using a larger particle diameter and concentration, it is generally more difficult to disperse larger particles in higher concentrations into carrier fluids without increasing the rate of particle agglomeration. Consequently, an optimum platelet size exists as a compromise between lubrication performance and suspension stability. As seen in Tables 5.3 and 5.4, the lubrication performance also increases with a higher graphite concentration. However, the reduction in specific grinding energy achieved by increasing the concentration from 1% to 2% using either nanoplatelet diameter was only 1-8%. Consequently, a higher concentration may increase the cost of fluid application without offering major improvements in lubrication performance.

Another important trend can also be observed from the results shown in Figures 5.4 and 5.5 that is unique for this grinding operation. At the lowest feed rate, low pressure flooding of the grinding contact zone at 5 L/min without solid lubricant additives reduced the specific grinding energy by ~20-25% over dry grinding for both workpiece materials. However, the lubrication performance tends to decrease

asymptotically at higher material removal rates for both the flood cooling method without additive and for the spray mist method using any parameter combination. This trend suggests that the effectiveness of fluid application could still be improved by selecting a different fluid delivery method or using an alternative combination of graphite lubrication parameters, especially at higher material removal rates where the fluid film is more likely to be squeezed out of the arc of cut by higher contact pressures and where film boiling is more likely to occur due to higher grinding zone temperatures. To improve fluid application under more aggressive grinding conditions, a larger platelet diameter could be used in combination with a higher additive concentration to form a thicker film that is less susceptible to deformation by the applied loads.

5.4.2 Characterization of Wheel Wear Performance

In the second part of this study, the combination of parameters resulting in the best graphite lubrication performance (15 μm platelet diameter, 2% concentration) was selected to perform a production run (250 parts) at a material removal rate of 30.9 mm^3/s and compare wheel wear performance in reduced quantity lubrication to the wear performance obtained using the same fluid without graphite additive in flood cooling. The deviation of the part diameter from the original target dimension (diameter error) was measured after every 25^{th} grinding pass to monitor the wheel wear trend, and the results are shown in Figure 5.6.

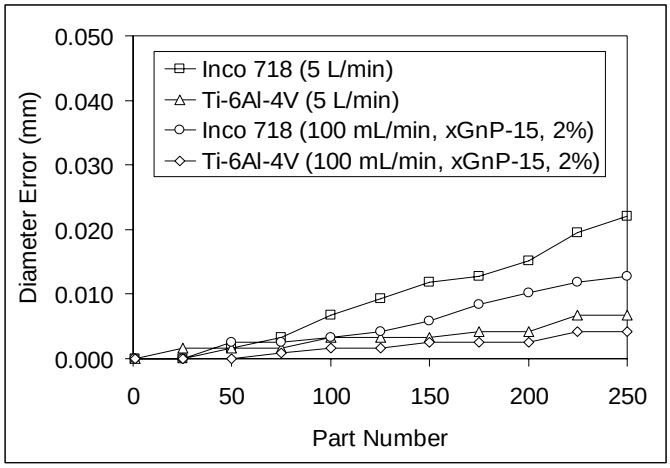

Figure 5.6: Wheel wear trends for flood cooling and best RQL condition with graphite nanoplatelets

The diameter error measured after grinding the 250th part was used to quantify the final volume of radial wheel wear and calculate the G-ratios shown in Figure 5.7. These results are comparable to the G-ratio values of 60-120 obtained when evaluating several types of cutting oils in a 4150 steel (HRC 48-57) cylindrical grinding operation using feed rates of 17.7-35.3 μm/s [101].

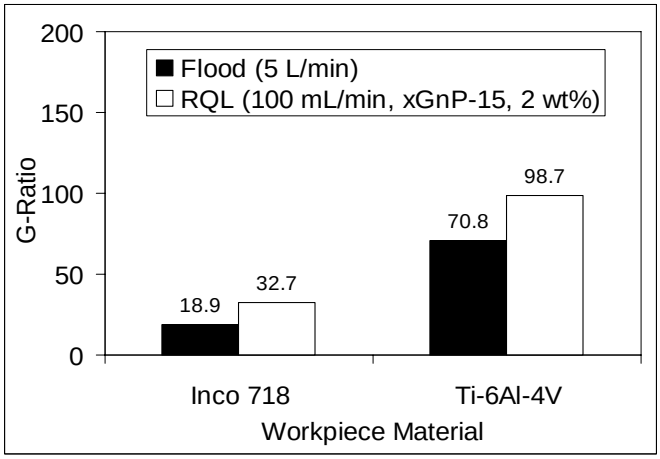

Figure 5.7: G-ratio summary for flood cooling and best RQL condition with graphite nanoplatelets

As seen in Figure 5.7, reduced quantity lubrication (100 mL/min) using an oil enhanced with 15 μm graphite nanoplatelets at a 2% concentration by weight increased the G-ratio by 73% for Inconel 718 and by 39% for Ti-6Al-4V over flood cooling (5 L/min) for a material removal rate of 30.9 mm^3/s. These positive results can be attributed to the good lubricating capacity of the graphite nanoplatelets, which reduce the frictional forces at the wheel-workpiece contact interface. In turn, the grains are able to maintain their sharpness for longer periods of time and undergo finer fracture behavior, which reduces their volumetric wear rate between dressing operations.

The promising results of this experiment can be used to further investigate the potential of improving process performance with the application of graphite nanoparticle-enhanced grinding fluids. Many other carrier fluid types, particle sizes, and additive concentrations can be explored to achieve more significant improvements. Based on the results, it is also evident that several options can still be explored to improve the effectiveness of fluid application for the centerless grinding operation. Since the geometric length of the wheel-workpiece contact arc is very small (less than 1 mm), it is difficult to achieve effective fluid delivery without the use of a very precise nozzle. However, the use of a high-pressure nozzle may affect the self-centering stability of the workpiece and have a negative impact on its dimensional accuracy, so new methods of fluid application should be evaluated. Other issues that need to be addressed in order to make the use of graphite nanoplatelet-enhanced grinding fluids more feasible in practice include the stabilization of graphite suspensions, chip removal from the grinding wheel surface, and sump cleaning and disposal.

5.5 Conclusions

This chapter presents the results of an experimental investigation conducted to assess the potential of reduced quantity lubrication centerless grinding of Inconel 718 and Ti-6Al-4V alloys using a graphite nanoplatelet-enhanced grinding fluid. The results confirm several advantages of graphite nanoplatelet-enhanced fluid application that can lead to a reduction in abrasive consumption and grinding fluid costs and an increase in the process productivity levels.

The following key conclusions can be made based on the results of this study:

- Reduced quantity lubrication (100 mL/min) using a cutting oil enhanced with a low concentration of graphite nanoplatelets (2%) reduced the specific grinding energy levels by up to 19% and 15% for Inconel 718 and Ti-6Al-4V, respectively, relative to flood cooling (5 L/min) over the experimental range of material removal rates. Consequently, the application of a graphite-nanoplatelet enhanced fluid may enable more aggressive material removal without incurring part thermal damage.
- Reduced quantity lubrication (100 mL/min) using a cutting oil enhanced with a low concentration of graphite nanoplatelets (2%) increased the G-ratio by up to 73% and 39% for Inconel 718 and Ti-6Al-4V, respectively, over flood cooling (5 L/min). Higher G-ratios lead to a reduction in the dressing frequency and a higher part output.

CHAPTER 6

CONCLUSIONS AND FUTURE STUDIES

6.1 Summary

In this thesis, two different methods are investigated for improving process performance in the plunge centerless grinding of Inconel 718 and Ti-6Al-4V superalloy fasteners: (i) economic optimization of grinding parameters and (ii) reduced quantity lubrication using a grinding fluid enhanced with graphite nanoplatelet additives. In the first part of the thesis (Chapters 3 and 4), a methodology is developed and carried out using Taguchi's Design of Experiments (DOE) method and machining economics theory to find the optimum grinding conditions in two stages: (i) modeling of process and part quality constraints (ii) determination of optimum grinding conditions in the feasible operating region. In the second part of the thesis (Chapter 5), an experimental study is conducted to evaluate centerless grinding performance using graphite nanoplatelet-enhanced fluids in reduced quantity lubrication and assess its potential as a cost-effective and ecologically-friendly alternative to the traditional flood cooling method.

6.2 Conclusions

Based on the findings of this thesis study, several key conclusions can be made about the optimization of centerless grinding performance for the Inconel 718 and Ti-6Al-4V alloys analyzed in this study.

6.2.1 Characterization of Process Parameter Effects on Centerless Grinding Performance

Chapter 3 presents the experimental studies conducted to characterize the effects of the major process parameters on different grinding performance responses in centerless grinding of Inconel 718 and Ti-6Al-4V alloys. The following key conclusions can be made from the results of this study:

6.2.1.1 Effects of Process Parameters on Measured Responses

- In rough grinding of Inconel 718, the amount of stock removed per pass that was directly correlated to the feed rate used in the experiments had the largest effect on the grinding power response (40.3%), followed by the regulating wheel speed (24.9%), grinding wheel material (20.0%), and grinding wheel speed (14.8%). In rough grinding of Ti-6Al-4V, the amount of stock removed per pass which was directly correlated to the feed rate used in the experiments had the largest effect on the grinding power response (44.7%), followed by the grinding wheel speed (34.7%), grinding wheel material (11.5%), and regulating wheel speed (9.0%). To minimize power consumption, the grinding parameters should be set to the minimum levels as predicted by theory for most conventional grinding operations.
- In rough grinding of Inconel 718, the regulating wheel speed had the largest effect on the surface roughness response (45.1%), followed by the amount of stock removed per pass (43.5%), grinding wheel speed (10.3%), and grinding

wheel material (1.1%). In rough grinding of Ti-6Al-4V, the amount of stock removed per pass had the largest effect on the grinding power response (37.5%), followed by the regulating wheel speed (37.0%), grinding wheel material (14.4%), and grinding wheel speed (11.1%). To minimize the surface roughness response, the grinding wheel speed should be set to the maximum allowable level and all other parameters should be set to the minimum level, which agrees with the theory for conventional grinding operations.

- Results show that material removal rates commonly used in rough grinding of Inconel 718 and Ti-6Al-4V fasteners (less than or equal to ~20 mm^3/s) are in the inefficient grinding regime, which is dominated by rubbing and ploughing of the work material instead of shearing. For the Inconel 718 and Ti-6Al-4V grinding wheels used in the experiments, the grinding operation should be performed at material removal rates greater than ~20 mm^3/s in order to increase the process efficiency and productivity.

6.2.1.2 Process Trends with Grinding Wheel Wear

- In the rough pass production runs of Inconel 718 and Ti-6Al-4V, the increase in grinding energy consumption with grinding wheel wear was minimized using lower wheel speeds. In particular, when grinding Ti-6Al-4V, the grinding wheel speed should be set to approximately 1/2 to 2/3 of the wheel

speed used for Inconel 718 (33.5 m/s) to minimize wheel loading leading to dimensional inaccuracies.

- In the Inconel 718 and Ti-6Al-4V production runs, a better surface finish was sustained using higher grinding wheel speeds in combination with lower feed rates and depths of cut as predicted by conventional grinding theory.

6.2.1.3 Grinding Wheel Performance and Material Removal Efficiency

- For Inconel 718, the 100% ceramic sol-gel (SG) grinding wheel (3SGP80-O6-VH) achieved a 2-4 times higher G-ratio and a 2-5 times higher grinding efficiency than the regular aluminum oxide wheel (2A80-O4-V) commonly used in the operation. These gains can be attributed to the finer grain fracture behavior of the sol-gel grinding wheel, which allows the grains to maintain their sharpness for longer periods of time during production. Finer grain fracture is also preferred over coarser grains fracture in order to maximize the utility of each grain exposed after dressing.
- For Ti-6Al-4V, the wheels compared in this study achieved similar G-ratios and grinding efficiencies over the experimental range of grinding conditions.

6.2.2 Economic Optimization of Centerless Grinding Parameters

Chapter 4 presents the methodology to find the optimum grinding conditions in centerless grinding, which is carried out using a simulation algorithm for the Inconel 718

and Ti-6Al-4V workpieces used in this study under the economic objective of minimum production cost per part. The following conclusions can be made from the analysis of the simulation results:

- For Inconel 718 and Ti-6Al-4V workpieces with diameters ranging from 7.94 mm (5/16 in.) to 25.4 mm (1 in.) with a 63.5 mm (2.5 in.) length, the cost-optimum material removal rate in rough grinding using the wheels evaluated in this study was verified to be ~40-100 mm^3/s corresponding to a specific material removal rate of 0.6-1.6 mm^2/s. The optimum results identified for the difficult-to-grind aerospace alloys are on the lower end of the specific material removal rate range recommended by different authors for centerless grinding (1-6 mm^2/s) with grinding wheel speeds of up to 45 m/s [70, 72].
- Grinding Inconel 718 and Ti-6Al-4V at the optimum parameters is expected to reduce the total cost per part by up to $0.05 for the grinding wheels used in this study under the conditions assumed in the simulation analysis.
- Further significant reductions in cost per part are expected with reductions in machine setup time, part loading and unloading time, part inspection time, and grinding fluid.

6.2.3 Performance of Graphite-Nanoplatelet Enhanced Fluids in Reduced Quantity Lubrication Centerless Grinding

Chapter 5 presents the experiments conducted to assess the potential of graphite nanoplatelet-enhanced fluids in reduced quantity lubrication centerless grinding of

Inconel 718 and Ti-6Al-4V alloys. The following key conclusions can be made from the results of this study:

- The effectiveness of grinding fluid application by low-pressure flooding decreases asymptotically with higher material removal rates as greater contact pressures squeeze the fluid film out of the grinding gap. The deflection of the fluid flow path by the dense air boundary layer surrounding the rotating grinding wheel generally makes flood cooling highly inefficient.
- The lubrication performance of the grinding fluids evaluated in this study improved with the dispersion of graphite nanoplatelets. The greatest reduction in specific grinding energy levels was achieved using a larger platelet diameter (15 μm) and a higher additive concentration (2%).
- Reduced quantity lubrication (100 mL/min) using a cutting oil enhanced with a 2% concentration of 15 μm graphite nanoplatelets reduced the specific grinding energy levels by 19% at a low material removal rate and by 8% at a high material removal rate over flood cooling (5 L/min) when grinding Inconel 718. The corresponding reduction in specific grinding energy levels for Ti-6Al-4V was 15% at a low material removal rate and 5% at a high material removal rate.
- Reduced quantity lubrication (100 mL/min) using a cutting oil enhanced with a 2% concentration of 15 μm graphite nanoparticles increased the G-ratio by 73% for Inconel 718 and by 39% for Ti-6Al-4V over conventional flood cooling (5 L/min).

6.3 Recommendations for Future Studies

In view of the system level approach to grinding process optimization presented in Chapter 1, additional research is recommended in several different areas to develop more effective optimization strategies for increasing the productivity and reducing the costs of this operation for different materials and workpiece geometries found in practice.

6.3.1 Optimization of Geometric Setup Parameters

Over the years, researchers have identified that the following key aspects of the centerless grinding process limit the productivity and part quality of the operation: (1) workpiece rounding instability, (2) dynamic system instability, and (3) workpiece rotation instability. As discussed in Chapter 2, many studies have been conducted to model the effects of the major geometric setup parameters on workpiece accuracy and identify the range of parameters for stable workpiece rounding motion. However, no attempts have been made so far to optimize these settings with the objective of minimizing wheel wear for the different part geometries, which could be accomplished with the help of advanced statistical methods such as stream of variation (SoV) theory.

6.3.2 Modeling of Centerless Grinding Machine Structural Effects

A majority of the scientific literature on the centerless grinding process has been concerned with the accuracy of the operation rather than its potential for higher material

removal rates. It has been shown that higher output may be obtained using higher feed rates in combination with higher wheel speeds up to the constraints of workpiece motion instability. In order to increase productivity without incurring a loss in part quality levels, it is necessary to increase the dynamic stiffness of the machine tool. The machine tool is a very important element of the entire system and its structural quality usually constrains the levels of productivity that can be achieved in practice. Although machine tool structures have been studied for many machining processes using FEA, the research conducted for modeling the stresses in structural components of centerless grinders still needs further development and validation. Fundamental redesign of the machine tool structure for higher dynamic stiffness based on the modeling results could lead to an appreciable improvement in the accuracy and productivity of the operation.

6.3.3 Modeling of Heat Transfer in Centerless Grinding

Grinding is a highly temperature-dependent machining process that can result in several problems when performed incorrectly, including workpiece thermal damage and ineffective cooling by fluid application. No comprehensive thermal model has yet been developed for the plunge centerless grinding operation that takes into account the complex workpiece rounding mechanics, elastic system deflections, and multiple heat source passes over the nominal contact area. The understanding of heat generation in the contact zone and how it affects the temperature field in the workpiece subsurface will be very useful in controlling thermal damage and comparing the effectiveness of different fluid application methods in this process.

6.3.4 Optimization of Fluid Application Parameters

In the centerless grinding of Inconel 718 and Ti-6Al-4V alloys, it was observed that reduced quantity lubrication (100 mL/min) using a cutting oil enhanced with a small concentration of graphite nanoplatelets reduces specific grinding energy levels and wheel wear rates more significantly than flood cooling (5 L/min) using the same fluid without graphite additives. However, many different fluid application settings can still be explored to improve the cooling and lubrication effectiveness of fluids in centerless grinding where the wheel-workpiece contact arc is very small compared to more conventional grinding operations. In conventional operations such as surface and cylindrical grinding, precise high-pressure nozzles can be used to achieve more effective fluid delivery at reduced flow rates, but in centerless grinding this may not be a practical solution since high-speed air jets may affect the self-centering motion of the workpiece and have a negative impact on its final dimensional accuracy. Other topics that also need to be addressed in future studies to enable the use of graphite nanoplatelet-enhanced grinding fluids in a production setting include the stabilization of graphite suspensions, chip removal from the grinding wheel surface, and sump cleaning and disposal.

APPENDIX A: Design of Experiments

Table A.1: *OA* $(8, 2^3, 4^1)$ for characterization experiment

Trial	Grinding Wheel Speed	Regulating Wheel Speed	Stock Removed per Pass	Grinding Wheel Material
1	1	1	2	2
2	1	2	1	1
3	2	1	2	1
4	2	2	1	2
5	3	1	1	2
6	3	2	2	1
7	4	1	1	1
8	4	2	2	2

Table A.2: *OA* $(4, 2^2)$ for graphite lubrication experiment

Trial	Platelet Diameter	Concentration
1	1	1
2	1	2
3	2	1
4	2	2

APPENDIX B: Grinding Wheel Recommendations

Table B.1: Inconel 718 grinding wheel recommendations

Reference	Abrasive Material	Grain Size	Hardness Range	Structure Number Range	Bond Type
Manufacturers	Al_2O_3	80-120	K-T	6-11	V
Lit. Survey	Al_2O_3	60-150	J-T	4-9	V

Table B.2: Ti-6Al-4V grinding wheel recommendations

Reference	Abrasive Material	Grain Size	Hardness Range	Structure Number Range	Bond Type
Manufacturers	SiC	120-150	L-R	6-12	V
Lit. Survey	SiC	60-150	J-T	6-12	V

APPENDIX C: Experimental Data

Characterization Experiment

Table C.1: Characterization experiment data (Inconel 718)

Dressing Overlap Ratio	Grinding Wheel Speed (m/s)	Regulating Wheel Speed (m/min)	Stock Removed per Pass (mm)	Feed Rate (mm/s)	Spark Out Time (s)	Wheel (0=A) (1=B)	Grind Power (W)	Surface Roughness (um)
2.36	19.1	13.4	0.1524	0.0316	1.09	0	1106	2.10
2.36	19.1	13.4	0.1524	0.0381	1.50	0	1116	2.03
2.36	23.9	24.5	0.0762	0.0331	0.75	0	1038	1.97
2.36	23.9	24.5	0.0762	0.0244	0.34	0	846	1.90
2.36	28.7	13.4	0.0762	0.0126	0.47	0	658	1.37
2.36	28.7	13.4	0.0762	0.0128	0.53	0	721	1.35
2.36	33.5	24.5	0.1524	0.0501	0.38	0	1586	2.45
2.36	33.5	24.5	0.1524	0.0492	0.35	0	1545	2.33
2.36	*33.5*	*13.4*	*0.127*	*0.0391*	*1.52*	*0*	**952*	**1.65*
2.36	*19.1*	*13.4*	*0.127*	*0.0391*	*1.47*	*0*	**911*	**1.85*
4.72	*33.5*	*13.4*	*0.0635*	*0.0195*	*1.50*	*0*	**872*	**0.54*
2.36	19.1	24.5	0.0762	0.0241	0.32	1	647	1.84
2.36	19.1	24.5	0.0762	0.0246	0.35	1	667	1.95
2.36	23.9	13.4	0.1524	0.0280	0.78	1	789	1.70
2.36	23.9	13.4	0.1524	0.0284	0.82	1	802	1.90
2.36	28.7	24.5	0.1524	0.0674	0.67	1	1477	2.67
2.36	28.7	24.5	0.1524	0.0482	0.32	1	1131	2.47
2.36	33.5	13.4	0.0762	0.0122	0.38	1	681	1.42
2.36	33.5	13.4	0.0762	0.0115	0.18	1	631	1.32
2.36	*33.5*	*13.4*	*0.127*	*0.0391*	*1.51*	*1*	**911*	**1.67*
2.36	*19.1*	*13.4*	*0.127*	*0.0391*	*1.48*	*1*	**785*	**1.83*
4.72	*33.5*	*13.4*	*0.0635*	*0.0195*	*1.50*	*1*	**758*	**0.81*

* Data obtained in production run experiment for 1st part (sharp grinding wheel)

Table C.2: Characterization experiment data (Ti-6Al-4V)

Dressing Overlap Ratio	Grinding Wheel Speed (m/s)	Regulating Wheel Speed (m/min)	Stock Removed per Pass (mm)	Feed Rate (mm/s)	Spark Out Time (s)	Wheel (0=A) (1=B)	Grind Power (W)	Surface Roughness (μm)
2.36	19.1	13.4	0.1524	0.0188	0.19	0	603	1.86
2.36	19.1	13.4	0.1524	0.0403	1.61	0	1071	2.08
2.36	23.9	24.5	0.0762	0.0213	0.12	0	588	1.83
2.36	23.9	24.5	0.0762	0.0218	0.16	0	617	1.75
2.36	28.7	13.4	0.0762	0.0243	1.93	0	857	1.26
2.36	28.7	13.4	0.0762	0.0152	1.00	0	621	1.35
2.36	33.5	24.5	0.1524	0.0492	0.36	0	1263	2.41
2.36	33.5	24.5	0.1524	0.0573	0.58	0	1403	2.45
2.36	*33.5*	*13.4*	*0.127*	*0.0391*	*1.53*	*0*	**1008*	**1.61*
2.36	*19.1*	*13.4*	*0.127*	*0.0391*	*1.47*	*0*	**716*	**1.82*
4.72	*14.4*	*13.4*	*0.0635*	*0.0195*	*1.49*	*0*	**613*	**0.45*
2.36	19.1	24.5	0.0762	0.0175	0.14	1	659	1.65
2.36	19.1	24.5	0.0762	0.0206	0.06	1	748	1.79
2.36	23.9	13.4	0.1524	0.0182	0.07	1	952	1.55
2.36	23.9	13.4	0.1524	0.0243	0.37	1	1032	1.60
2.36	28.7	24.5	0.1524	0.0492	0.36	1	1430	2.27
2.36	28.7	24.5	0.1524	0.0372	0.27	1	1335	2.12
2.36	33.5	13.4	0.0762	0.0123	0.40	1	869	1.22
2.36	33.5	13.4	0.0762	0.0121	0.35	1	829	1.09
2.36	*33.5*	*13.4*	*0.127*	*0.0391*	*1.52*	*1*	**1118*	**1.44*
2.36	*19.1*	*13.4*	*0.127*	*0.0391*	*1.48*	*1*	**814*	**1.65*
4.72	*14.4*	*13.4*	*0.0635*	*0.0195*	*1.51*	*1*	**772*	**0.37*

* Data obtained in production run experiment for 1st part (sharp grinding wheel)

Production Run Experiment

Table C.3: Dressing and grinding parameters for production runs (Inconel 718)

Production Run	Number of Parts	Dressing Overlap Ratio	Grinding Wheel Speed (m/s)	Stock Removed per Pass (mm)	Feed Rate (mm/s)	Wheel Material (A or B)
1-R	250	2.36	33.5	0.127	0.0391	Cincinnati (A)
2-R	250	2.36	19.1	0.127	0.0391	Cincinnati (A)
3-F	500	4.72	33.5	0.0635	0.0195	Cincinnati (A)
4-R	250	2.36	33.5	0.127	0.0391	Norton SG (B)
5-R	250	2.36	19.1	0.127	0.0391	Norton SG (B)
6-F	500	4.72	33.5	0.0635	0.0195	Norton SG (B)

Table C.4: Time series data for production run experiment (Inconel 718)

Production Run 1

Part Number	Grinding Power (W)	Surface Roughness (μm)	Diameter Error (mm)	Transition Radius Error (mm)
1	902	1.65	0.00000	0.00000
25	852	0.91	-0.00084	0.01270
50	1128	0.87	-0.00170	0.02794
75	1179	0.88	-0.00170	0.03302
100	1163	0.87	0.00508	0.05334
125	1345	0.87	0.00762	0.06858
150	1273	0.85	0.01016	0.08128
175	1501	0.86	0.01440	0.09652
200	1356	0.85	0.01948	0.10414
225	1398	0.85	0.01948	0.10922
250	1461	0.87	0.02032	0.13208

Production Run 2

Part Number	Grinding Power (W)	Surface Roughness (μm)	Diameter Error (mm)	Transition Radius Error (mm)
1	761	1.85	0.00000	0.00000
25	814	1.03	-0.00254	0.02794
50	857	1.02	0.00338	0.04064
75	899	0.93	0.01100	0.07620
100	799	0.83	0.01270	0.10414
125	1013	0.85	0.01948	0.13716
150	1013	0.84	0.02370	0.15748
175	1025	0.81	0.02370	0.17018
200	902	0.70	0.02370	0.19050
225	935	0.72	0.03132	0.19812
250	1002	0.69	0.03894	0.21336

Production Run 3

Part Number	Grinding Power (W)	Surface Roughness (μm)	Diameter Error (mm)	Transition Radius Error (mm)
1	872	0.54	0.00000	0.00000
50	944	0.45	-0.00254	0.00000
100	1036	0.42	-0.00084	0.01016
150	1116	0.42	0.00084	0.01524
200	1110	0.41	0.00424	0.02286
250	1130	0.43	0.00424	0.03302
300	1081	0.42	0.00846	0.04318
350	1124	0.41	0.00846	0.05588
400	1176	0.43	0.01100	0.06096
450	1231	0.41	0.01100	0.06858
500	1248	0.41	0.01440	0.08128

Production Run 4

Part Number	Grinding Power (W)	Surface Roughness (μm)	Diameter Error (mm)	Transition Radius Error (mm)
1	861	1.67	0.00000	0.00000
25	987	1.33	-0.00254	0.01270
50	931	1.23	-0.00508	0.02032
75	1047	1.18	-0.00678	0.03048
100	902	1.14	-0.00170	0.03556
125	1157	1.09	0.00170	0.04318
150	1183	1.13	0.00170	0.05080
175	1114	1.07	0.00170	0.05588
200	1217	1.17	0.00000	0.07112
225	1255	1.09	0.00678	0.07874
250	1172	1.13	0.00592	0.09144

Production Run 5

Part Number	Grinding Power (W)	Surface Roughness (μm)	Diameter Error (mm)	Transition Radius Error (mm)
1	685	1.83	0.00000	0.00000
25	718	1.33	-0.00170	0.00762
50	852	1.30	0.00170	0.01778
75	779	1.22	0.00338	0.02540
100	776	1.18	0.00678	0.03048
125	745	1.14	0.00932	0.04064
150	1031	1.12	0.01186	0.05588
175	957	1.12	0.01270	0.07366
200	1013	1.13	0.01524	0.08636
225	1034	1.14	0.01948	0.10160
250	1096	1.13	0.02202	0.11684

Production Run 6

Part Number	Grinding Power (W)	Surface Roughness (μm)	Diameter Error (mm)	Transition Radius Error (mm)
1	508	0.81	0.00000	0.00000
50	647	0.76	0.00000	0.00000
100	928	0.75	-0.00508	0.00508
150	1056	0.73	-0.00678	0.01270
200	776	0.65	-0.00424	0.01778
250	839	0.58	-0.00678	0.02286
300	929	0.53	-0.00338	0.03302
350	946	0.54	-0.00084	0.03556
400	898	0.53	-0.00084	0.03810
450	923	0.55	0.00170	0.04318
500	862	0.54	0.00424	0.04572

Table C.5: Dressing and machining parameters for production runs (Ti-6Al-4V)

Production Run	Number of Parts	Dressing Overlap Ratio	Grinding Wheel Speed (m/s)	Stock Removed per Pass (mm)	Feed Rate (mm/s)	Wheel Material (A or B)
1-R	250	2.36	33.5	0.127	0.0391	Kinik (A)
2-R	250	2.36	19.1	0.127	0.0391	Kinik (A)
3-F	500	4.72	14.4	0.0635	0.0195	Kinik (A)
4-R	250	2.36	33.5	0.127	0.0391	Norton (B)
5-R	250	2.36	19.1	0.127	0.0391	Norton (B)
6-F	500	4.72	14.4	0.0635	0.0195	Norton (B)

Table C.6: Time series data for production run experiment (Ti-6Al-4V)

Production Run 1

Part Number	Grinding Power (W)	Surface Roughness (μm)	Diameter Error (mm)	Transition Radius Error (mm)
1	1208	1.61	0.00000	0.00000
25	1251	1.28	-0.00254	0.02794
50	1267	1.25	-0.00254	0.06096
75	1371	1.24	-0.00254	0.07620
100	1360	1.15	-0.00254	0.09652
125	1258	1.15	-0.00254	0.12446
150	1311	1.14	-0.00338	0.13208
175	1307	1.14	-0.00338	0.14478
200	1336	1.10	-0.00424	0.16510
225	1336	1.09	-0.00170	0.19304
250	1414	1.07	-0.00084	0.20066

Production Run 2

Part Number	Grinding Power (W)	Surface Roughness (μm)	Diameter Error (mm)	Transition Radius Error (mm)
1	946	1.82	0.00000	0.00000
25	835	1.09	0.00170	0.02794
50	797	1.07	0.00170	0.06350
75	790	1.07	0.00170	0.08890
100	763	1.03	0.00338	0.11684
125	752	1.06	0.00338	0.14478
150	767	1.08	0.00338	0.18034
175	790	1.09	0.00424	0.22860
200	785	1.06	0.00424	0.27686
225	850	1.09	0.00678	0.32512
250	830	1.13	0.00678	0.36068

Production Run 3

Part Number	Grinding Power (W)	Surface Roughness (μm)	Diameter Error (mm)	Transition Radius Error (mm)
1	913	0.45	0.00000	0.00000
50	810	0.40	0.00000	0.03556
100	783	0.41	-0.00084	0.08382
150	796	0.39	0.00170	0.12700
200	796	0.40	0.00170	0.15494
250	700	0.40	0.00424	0.18796
300	745	0.40	0.00424	0.21590
350	705	0.39	0.00424	0.24384
400	705	0.38	0.00424	0.27940
450	714	0.38	0.00424	0.29972
500	732	0.41	0.00424	0.30734

Production Run 4

Part Number	Grinding Power (W)	Surface Roughness (μm)	Diameter Error (mm)	Transition Radius Error (mm)
1	1268	1.44	0.00000	0.00000
25	1528	0.97	-0.00424	0.02540
50	1675	0.94	-0.00678	0.04064
75	1622	0.86	-0.00678	0.06858
100	1747	0.85	-0.00762	0.07366
125	1792	0.88	-0.01016	0.10160
150	1767	0.91	-0.01016	0.12446
175	1669	0.88	0.00170	0.14478
200	1703	0.82	-0.00254	0.15748
225	1777	0.80	-0.00254	0.17780
250	1817	0.80	-0.00170	0.20574

Production Run 5

Part Number	Grinding Power (W)	Surface Roughness (μm)	Diameter Error (mm)	Transition Radius Error (mm)
1	814	1.65	0.00000	0.00000
25	783	0.87	0.00254	0.02794
50	801	0.81	0.00170	0.04064
75	828	0.82	0.00170	0.06858
100	765	0.82	0.00254	0.07366
125	819	0.81	0.00254	0.10414
150	774	0.81	0.00424	0.13208
175	736	0.81	0.00338	0.16510
200	772	0.80	0.00338	0.20066
225	810	0.80	0.00592	0.22860
250	799	0.80	0.00592	0.25654

Production Run 6

Part Number	Grinding Power (W)	Surface Roughness (μm)	Diameter Error (mm)	Transition Radius Error (mm)
1	872	0.37	0.00000	0.00000
50	766	0.36	0.00000	0.03810
100	747	0.35	0.00170	0.07112
150	722	0.35	0.00170	0.09906
200	831	0.34	0.00170	0.11430
250	750	0.35	0.00084	0.14224
300	744	0.35	0.00424	0.17018
350	749	0.34	0.00424	0.18288
400	728	0.34	0.00424	0.21082
450	733	0.35	0.00424	0.23876
500	736	0.34	0.00424	0.25146

Table C.7: Summary of machining parameters for Inconel 718 rough pass production runs

Production Run	Wheel Material (A or B)	Grinding Wheel Speed (m/s)	Dressing Overlap Ratio	Regulating Wheel Speed (m/min)	Stock Removed per Pass (mm)	Feed Rate (mm/s)
A1	A	33.5	2.36	13.4	0.127	0.0391
A2	A	19.1	2.36	13.4	0.127	0.0391
B1	B	33.5	2.36	13.4	0.127	0.0391
B2	B	19.1	2.36	13.4	0.127	0.0391

Table C.8: Wheel topography data summary for Cincinnati Inconel 718 grind wheel (A1)

Part Number	1	25	50	75	100	125	150	175	200	225	250
% Active Grains	5.8	8.2	13.5	16.3	18.1	17.6	19.3	17.8	19.5	18.4	19.7
% Wear Flat Area	0.7	1	1.3	1.5	1.5	1.6	1.7	1.7	1.8	2	2.1
% Grain Pullouts	4.2	6.8	7.7	9	10.5	13	16.3	18.8	21.5	23	25.5

Table C.9: Wheel topography data summary for Cincinnati Inconel 718 grind wheel (A2)

Part Number	1	25	50	75	100	125	150	175	200	225	250
% Active Grains	9.4	12.5	17.1	22.2	24.9	24.7	25.1	25.8	26	26.4	26.9
% Wear Flat Area	0.6	0.9	1.1	1.1	1.2	1.3	1.3	1.4	1.4	1.5	0.6
% Grain Pullouts	2.8	4.7	5.9	7	7.9	11.4	14.4	17	19.9	21.9	23

Table C.10: Wheel topography data summary for Norton SG Inconel 718 grind wheel (B1)

Part Number	1	25	50	75	100	125	150	175	200	225	250
% Active Grains	4.6	7.5	8.5	11.3	11.5	12.1	10.1	11	13.2	13	14.5
% Wear Flat Area	0.5	0.7	0.9	1	1.2	1.4	1.5	1.5	1.6	1.7	1.7
% Grain Pullouts	2.6	5	6.8	7.6	9	10	10.8	12.8	14.3	15.2	16

Table C.11: Wheel topography data summary for Norton SG Inconel 718 grind wheel (B2)

Part Number	1	25	50	75	100	125	150	175	200	225	250
% Active Grains	8.8	10.4	14	18.5	20.5	21	22.5	21.3	22.1	22.3	22.5
% Wear Flat Area	0.4	0.6	0.8	0.9	0.9	1	1	1	1.2	1.3	1.3
% Grain Pullouts	2	2.9	4.8	5.8	6.8	8.3	9.5	10.4	12	13.4	13.9

Graphite Lubrication Experiment

Table C.12: Graphite lubrication experiment data (Inconel 718)

Graphite Platelet Diameter	Graphite Concentration by Weight	SGE at 15.4 mm^3/s (J/mm^3)	SGE at 30.9 mm^3/s (J/mm^3)	SGE at 61.9 mm^3/s (J/mm^3)
1 μm	1 %	62.1	42.4	25.7
1 μm	1 %	56.1	35.6	17.7
1 μm	2 %	55.9	41.2	23.6
1 μm	2 %	62.1	34.8	17.2
15 μm	1 %	57.4	38.8	17.2
15 μm	1 %	51.6	32.8	23.6
15 μm	2 %	47.8	30.0	18.7
15 μm	2 %	52.6	35.0	23.7

Table C.13: Graphite lubrication experiment data (Ti-6Al-4V)

Graphite Platelet Diameter	Graphite Concentration by Weight	SGE at 15.4 mm^3/s (J/mm^3)	SGE at 30.9 mm^3/s (J/mm^3)	SGE at 61.9 mm^3/s (J/mm^3)
1 μm	1 %	67.4	42.3	27.4
1 μm	1 %	72.3	47.5	23.0
1 μm	2 %	71.2	46.8	27.2
1 μm	2 %	67.4	42.2	22.8
15 μm	1 %	66.1	44.9	26.3
15 μm	1 %	61.3	40.5	22.3
15 μm	2 %	63.7	43.6	26.2
15 μm	2 %	58.7	39.0	22.0

APPENDIX D: Data Analysis

Characterization Experiment – S/N Ratio Analysis

Table D.1: S/N ratio analysis summary for grinding power response (Inconel 718)

Experimental Level	Grinding Wheel Speed	Regulating Wheel Speed	Stock Removed per Pass	Grinding Wheel Material
1	-61.64	-61.02	-60.25	-63.28
2	-61.76	-63.52	-64.29	-61.26
3	-62.55	---	---	---
4	-63.13	---	---	---
ABS (Max – Min)	1.48	2.50	4.05	2.01
Rank	4	2	1	3
% Contribution	14.8	24.9	40.3	20.0

Table D.2: S/N ratio analysis summary for grinding power response (Ti-6Al-4V)

Experimental Level	Grinding Wheel Speed	Regulating Wheel Speed	Stock Removed per Pass	Grinding Wheel Material
1	-60.71	-61.74	-60.28	-61.63
2	-60.77	-62.47	-63.93	-62.58
3	-63.39	---	---	---
4	-63.55	---	---	---
ABS (Max – Min)	2.84	0.74	3.66	0.94
Rank	2	4	1	3
% Contribution	34.7	9.0	44.7	11.5

Table D.3: S/N ratio analysis summary for surface roughness response (Inconel 718)

Experimental Level	Grinding Wheel Speed	Regulating Wheel Speed	Stock Removed per Pass	Grinding Wheel Material
1	-8.78	*-7.16*	*-7.21*	*-8.47*
2	-8.55	-9.84	-9.80	-8.54
3	-8.53	---	---	---
4	*-8.16*	---	---	---
ABS (Max – Min)	0.62	2.68	2.58	0.07
Rank	3	1	2	4
% Contribution	10.3	45.1	43.5	1.1

Table D.4: S/N ratio analysis summary for surface roughness response (Ti-6Al-4V)

Experimental Level	Grinding Wheel Speed	Regulating Wheel Speed	Stock Removed per Pass	Grinding Wheel Material
1	-8.31	*-6.36*	*-6.34*	-8.25
2	-7.51	-9.09	-9.10	*-7.19*
3	-7.58	---	---	---
4	*-7.49*	---	---	---
ABS (Max – Min)	0.82	2.73	2.76	1.06
Rank	4	2	1	3
% Contribution	11.1	37.0	37.5	14.4

Characterization Experiment – Multiple Regression Model Statistics

Table D.5: Grinding power response model statistics (Inconel 718)

Regression Statistics	
Multiple R	0.965
R Square	0.931
Adjusted R Square	0.903
Standard Error	89.8
Observations	22

ANOVA

	df	*F*	*Significance F*
Regression	6	33.5	7.34E-08
Residual	15		
Total	21		

	Coefficients	*Standard Error*	*t Stat*	*P-value*
Intercept	-426.9	206.0	-2.1	0.055843
Dressing Overlap Ratio	63.1	35.6	1.8	0.096809
Grinding Wheel Speed	12.4	3.5	3.5	0.003021
Regulating Wheel Speed	1102.3	315.8	3.5	0.003289
Stock Removed per Pass	3704.2	1139.6	3.3	0.005377
Feed Rate	7118.8	3022.3	2.4	0.032535
Grinding Wheel Material	-183.5	38.3	-4.8	0.000241

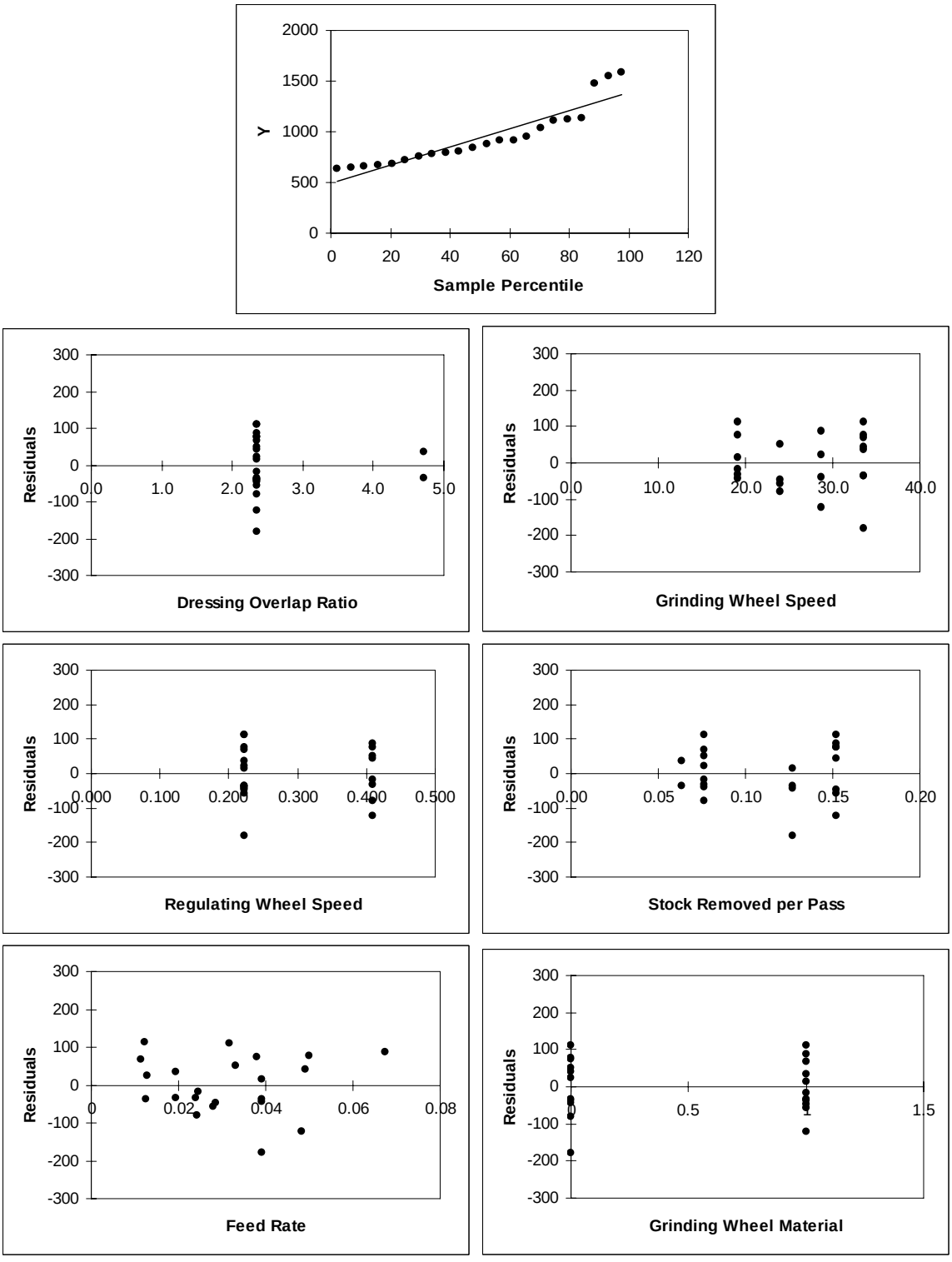

Figure D.1: Normal probability and residual plots

Grinding power response model (Inconel 718)

Table D.6: Surface roughness response model statistics (Inconel 718)

Regression Statistics	
Multiple R	0.993
R Square	0.986
Adjusted R Square	0.981
Standard Error	0.071
Observations	22

ANOVA

	df	*F*	*Significance F*
Regression	6	179.5	4.25E-13
Residual	15		
Total	21		

	Coefficients	*Standard Error*	*t Stat*	*P-value*
Intercept	1.592	0.240	6.634	0.000008
Dressing Overlap Ratio	-0.197	0.036	-5.453	0.000067
Grinding Wheel Speed	-0.013	0.004	-3.560	0.002853
Regulating Wheel Speed	1.212	0.529	2.292	0.036819
Stock Removed per Pass	3.374	1.080	3.124	0.006968
Feed Rate	16.212	3.969	4.085	0.000976
Sparkout Time	-0.236	0.082	-2.874	0.011596

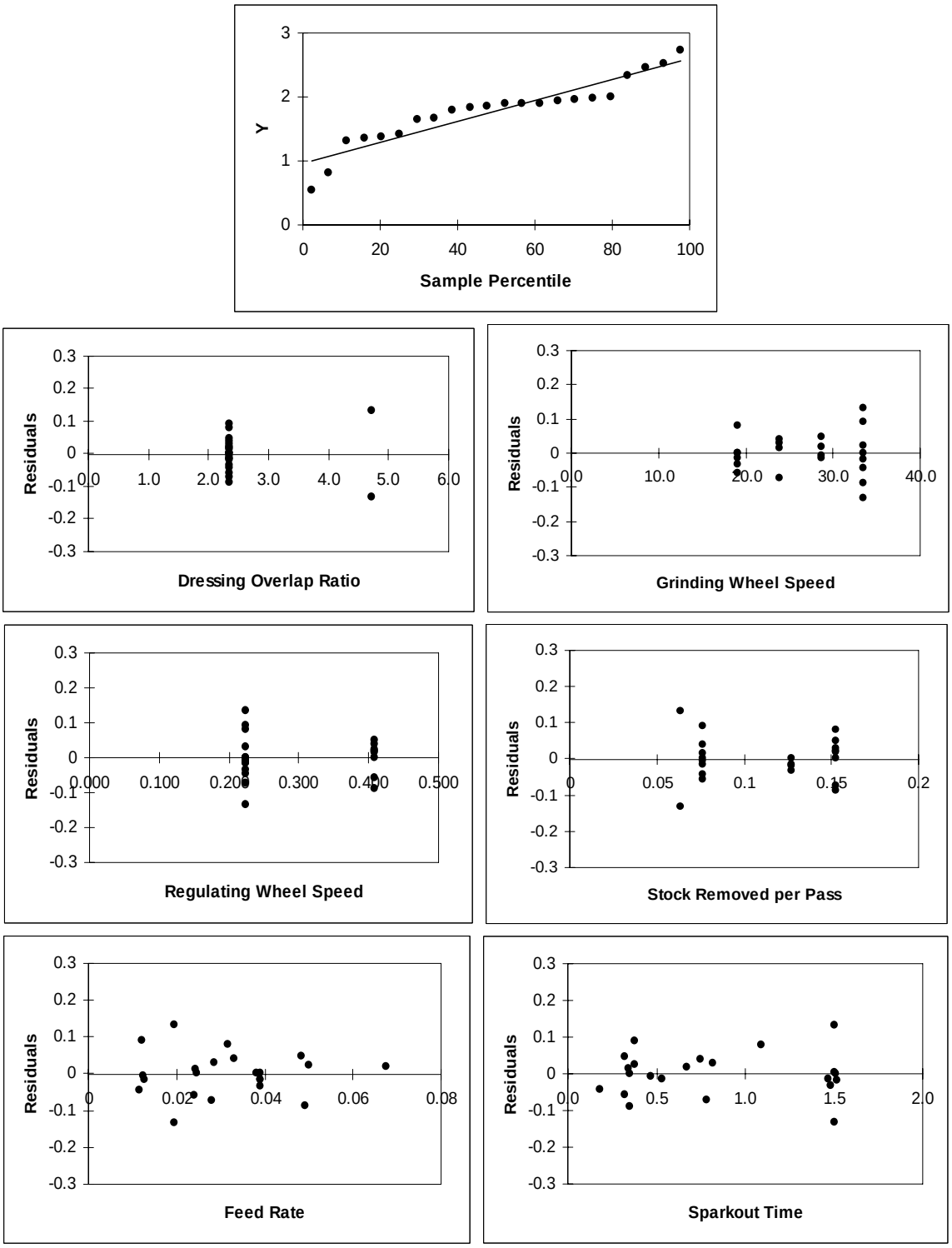

Figure D.2: Normal probability and residual plots

Surface roughness response model (Inconel 718)

Table D.7: Grinding power response model statistics (Ti-6Al-4V)

Regression Statistics	
Multiple R	0.957
R Square	0.915
Adjusted R Square	0.881
Standard Error	93.1
Observations	22

ANOVA

	df	*F*	*Significance F*
Regression	6	27.0	3.16E-07
Residual	15		
Total	21		

	Coefficients	*Standard Error*	*t Stat*	*P-value*
Intercept	-728.2	234.9	-3.1	0.007313
Dressing Overlap Ratio	125.4	40.9	3.1	0.007780
Grinding Wheel Speed	20.0	3.8	5.2	0.000108
Regulating Wheel Speed	459.0	258.2	1.8	0.095687
Stock Removed per Pass	3262.1	924.5	3.5	0.003042
Feed Rate	8015.8	2616.9	3.1	0.007889
Grinding Wheel Material	150.3	41.9	3.6	0.002723

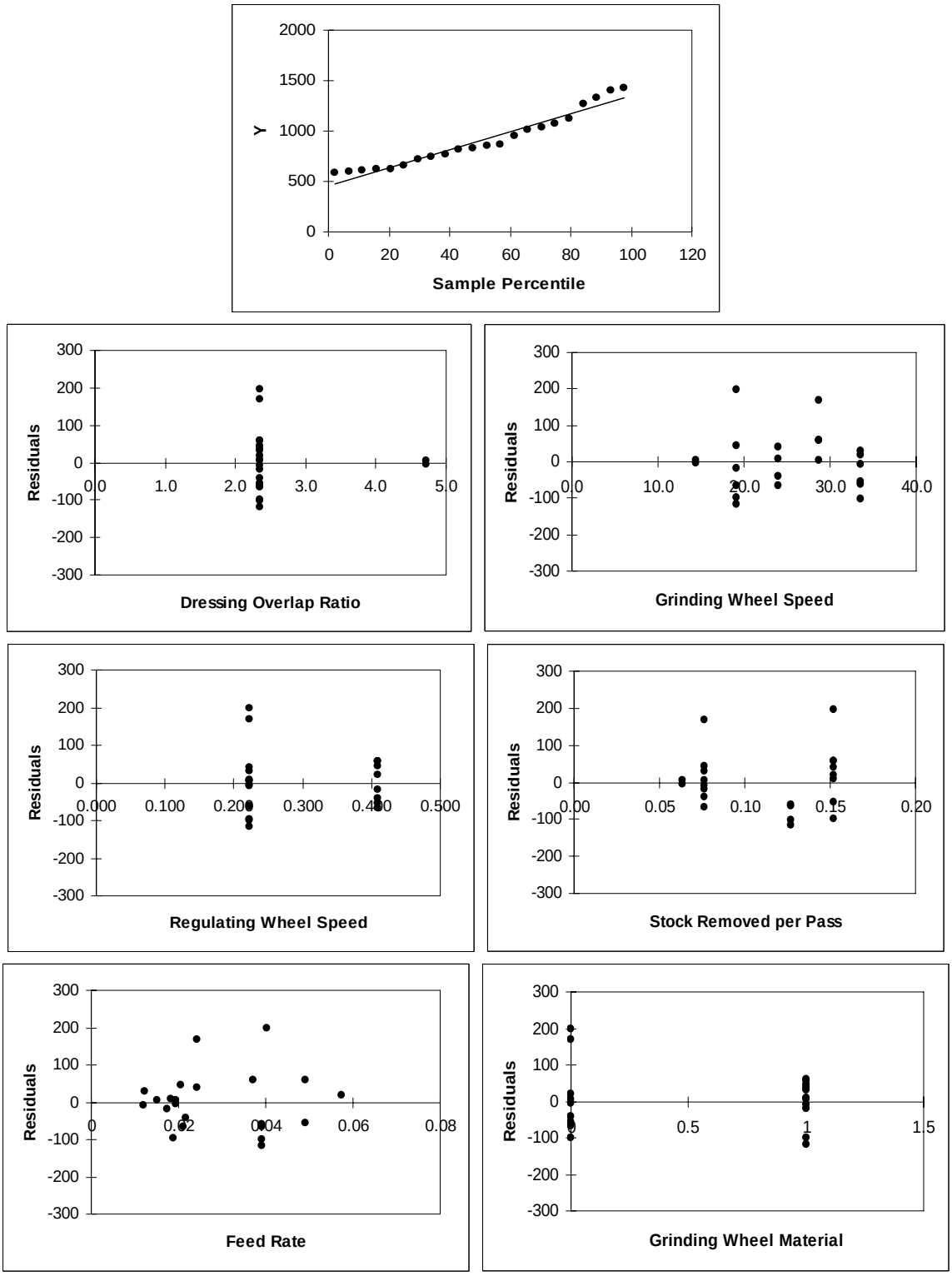

Figure D.3: Normal probability and residual plots

Grinding power response model (Ti-6Al-4V)

Table D.8: Surface roughness response model statistics (Ti-6Al-4V)

Regression Statistics	
Multiple R	0.993
R Square	0.987
Adjusted R Square	0.980
Standard Error	0.075
Observations	22

ANOVA

	df	*F*	*Significance F*
Regression	7	150.5	4.38E-12
Residual	14		
Total	21		

	Coefficients	*Standard Error*	*t Stat*	*P-value*
Intercept	1.841	0.320	5.755	0.000050
Dressing Overlap Ratio	-0.384	0.033	-11.652	1.363E-08
Grinding Wheel Speed	-0.012	0.003	-3.478	0.003693
Regulating Wheel Speed	1.571	0.550	2.857	0.012674
Stock Removed per Pass	3.520	1.315	2.678	0.018027
Feed Rate	14.331	4.714	3.040	0.008820
Grinding Wheel Material	-0.170	0.034	-4.929	0.000222
Sparkout Time	-0.143	0.080	-1.790	0.095119

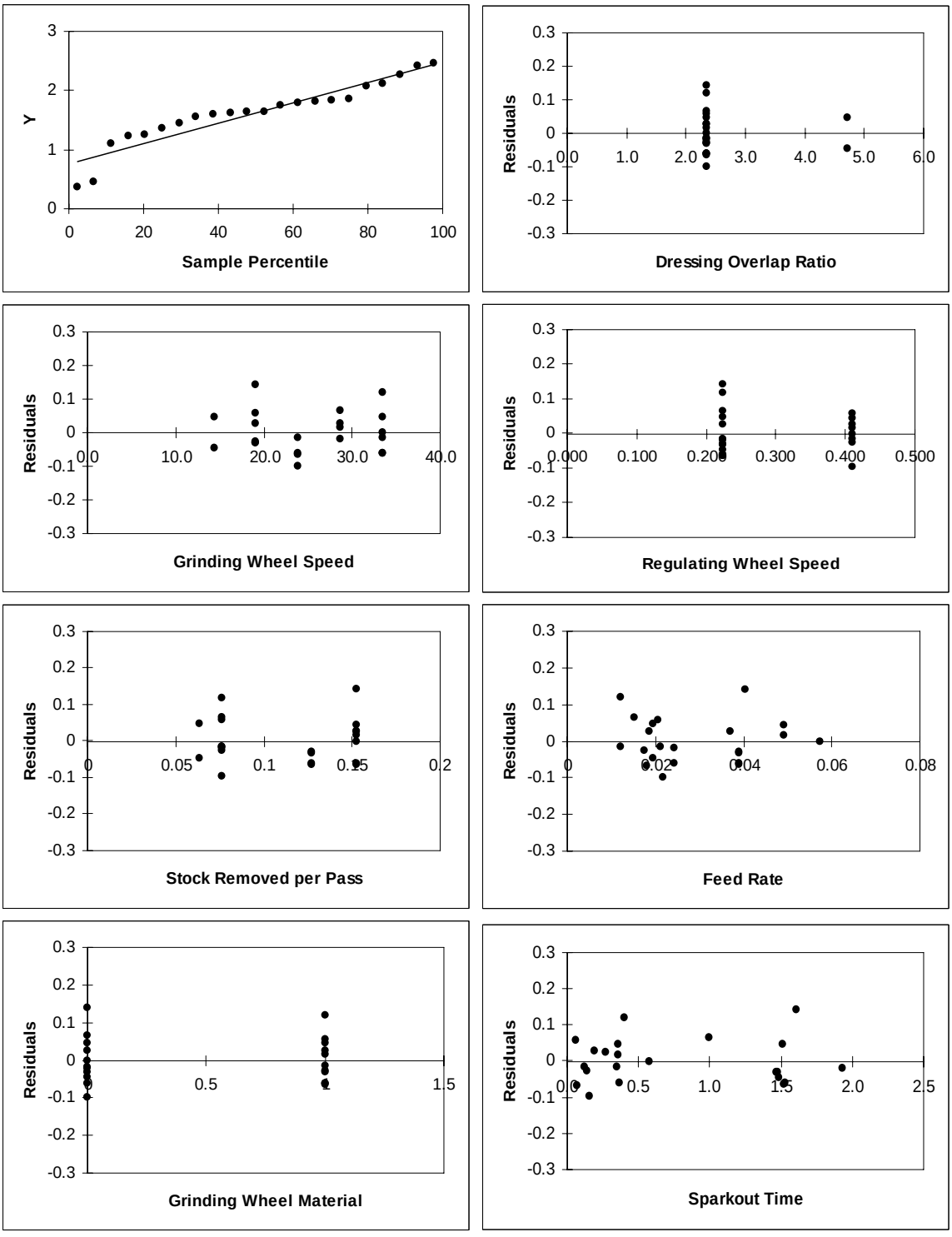

Figure D.4: Normal probability and residual plots

Surface roughness response model (Ti-6Al-4V)

Table D.9: Sample correlation matrix for characterization experiment factors

Grinding power response (Inconel 718)

	Dressing Overlap Ratio	Grinding Wheel Speed	Regulating Wheel Speed	Stock Removed per Pass	Radial Feed Rate	Grinding Wheel Material
Dressing Overlap Ratio	1.000	---	---	---	---	---
Grinding Wheel Speed	*0.531*	1.000	---	---	---	---
Regulating Wheel Speed	-0.239	0.127	1.000	---	---	---
Stock Removed per Pass	*-0.423*	0.224	0.048	1.000	---	---
Radial Feed Rate	-0.226	*0.302*	*0.313*	*0.670*	1.000	---
Grinding Wheel Material	0.000	0.000	0.000	0.000	-0.198	1.000

APPENDIX E: Index of Equations for Economic Simulation Algorithm

Parts per Dress = [Number of Ground Parts] x [Grain Protrusion Height / OD Error] (E.1)

Dressing Frequency During Production = [Number of Parts to Process] / [Parts per Dress] (E.2)

Total Dressing Time = [Dress Time at Beginning of Production] + [Dress Frequency During Production] x [(2 x Number of Dress Passes) x (Grinding Length / Dresser Traverse Rate)] (E.3)

Total Loading Time = [Number of Ground Parts] x [Loading Time per Part] (E.4)

Total Unloading Time = [Number of Ground Parts] x [Unloading Time per Part] (E.5)

Grinding Time per Part = [Volume of Material Removed] / [Material Removal Rate] (E.6)

Total Grinding Time = [Number of Ground Parts] x [Grinding Time per Part] (E.7)

Total Spark-Out Time = [Number of Ground Parts] x [Spark-Out Time per Part] (E.8)

Total Part Inspection Time = [Inspection Time per Part] x [Number of Ground Parts / Inspection Frequency] (E.9)

Production Time per Part = [1 / Number of Parts to Process] x [(Total Transfer Time) + (Total Setup Time)+ (Total Dressing Time) + (Total Loading Time) + (Total Grinding Time) + (Total Unloading Time) + (Total Part Inspection Time) + (Total Break Time)] (E.10)

Number of Produced Parts = [Production Period] / [Production Time per Part] (E.11)

Machine Cost per Part = [Unit Machine Cost] / [Number of Produced Parts] (E.12)

Wheel Cost per Part = [Unit Wheel Cost] x [Number of Wheels] / [Number of Produced Parts] (E.13)

Labor Cost per Part = [Time to Process Part] x [Labor Rate] (E.14)

Total Cost per Part = [Machine Cost per Part] + [Wheel Cost per Part] + [Labor Cost per Part] (E.15)

REFERENCES

[1] Subramanian, K., 1994, "Finishing Methods Using Multipoint or Random Cutting Edges," ASM Handbook, **5**, pp. 90-98.

[2] Rabinowicz, E., 1995, *Friction and Wear of Materials.* John Wiley, New York.

[3] Shaw, M., 1972, "Fundamentals of Grinding," *Proceedings of the International Grinding Conference: New Developments in Grinding*," Pittsburgh, PN, pp. 221-258.

[4] Komanduri, R., 1971, "Some Aspects of Machining with Negative Rake Tools Simulating Grinding," *International Journal of Machine Tool Design*, **11**, pp. 223-233.

[5] Maan, N. and Groenou, A.B., 1977, "Low Speed Scratch Experiments on Steels," *Wear*, **42**, pp. 365-390.

[6] Torrance, A.A., 1981, "A New Approach to the Mechanics of Abrasion," *Wear*, **67**, pp. 233-257.

[7] Challen, J.M. and Oxley, P.L.B., 1978, "An Explanation of the Different Regimes of Friction and Wear Using Asperity Deformation Models," *Wear*, **53**, pp. 229-243.

[8] Hokkirigawa, K. and Kato, K., 1988, "An Experimental and Theoretical Investigation of Ploughing, Cutting, and Wedge Formation During Abrasive Wear," *Tribology International*, **21**, pp. 51-57.

[9] Williams, J.A. and Xie, Y., 1992, "The Generation of Worn Surfaces by the Repeated Interaction of Parallel Grooves," *Wear*, **164**, pp. 864-872.

[10] Doman, D.A., Warkentin, A., and Bauer, R., 2006, "A Survey of Recent Grinding Wheel Topography Models," *International Journal of Machine Tools and Manufacture*, **46**, pp. 343-352.

[11] Hahn, R.S. and Lindsay, R.P., 1982A, "Principles of Grinding Part I. The Metal Removal Parameter," Grinding: Theory, Techniques and Trouble Shooting, SME, pp. 3-10.

[12] Hahn, R.S. and Lindsay, R.P., 1982B, "Principles of Grinding Part II. The Metal Removal Parameter," Grinding: Theory, Techniques and Trouble Shooting, SME, pp. 11-17.

[13] Hahn, R.S. and Lindsay, R.P., 1982C, "Principles of Grinding Part III. The Wheel Removal Parameter," Grinding: Theory, Techniques and Trouble Shooting, SME,

pp. 18-24.

[14] Hahn, R.S. and Lindsay, R.P., 1982D, "Principles of Grinding Part IV. Surface Finish, Geometry, and Integrity," Grinding: Theory, Techniques and Trouble Shooting, SME, pp. 25-35.

[15] Malkin, S., 1989, *Grinding Technology: Theory and Application of Machining with Abrasives.* Ellis Horwood Limited, New York.

[16] Shaw, M.C., 1996, *Principles of Abrasive Processing*. Oxford University Press, New York.

[17] Brinksmeier, E., Tönshoff, H., Czenkusch, C., and Heinzel, C., 1998, "Modeling and Optimization of Grinding Processes," *Journal of Intelligent Manufacturing*, **9**, pp. 303-314.

[18] Mukherjee, I. and Ray, P.K., 2008, "A Systematic Solution Methodology for Inferential Multivariate Modeling of Industrial Grinding Process," *Journal of Materials Processing Technology*, **196(1-3)**, pp. 379-392.

[19] Mohanasundararaju, N., Sivasubramanian, R., Gnanaguru, R., and Alagumurthy, N., 2008, A Neural Network and Fuzzy-Based Methodology for the Prediction of Work Roll Surface Roughness in a Grinding Process," *International Journal of Computational Methods in Engineering Science and Mechanics*, **9(2)**, pp. 103-110.

[20] Anamou, R., Ben Fredj, N., Fnaiech, F., 2008, "Improved Method for Grinding Force Prediction Based on Neural Network," *International Journal of Advanced Manufacturing Technology*, **39(7-8)**, pp. 656-668.

[21] Nandi, A.K., Pratihar, D.K., and Banerjee, M.K., 2004, "Prediction of Grinding Power and Surface Finish – A GA-Fuzzy Approach," *Integrated Computer-Aided Engineering*, **11(4)**, pp. 373-382.

[22] Qi, H.S., Rowe, W.B., and Mills, B., 2001, "Fuzzy Contact and Its Effect on Thermal Damage in Grinding Processes," *Key Engineering Materials*, **202-203**, pp. 15-24.

[23] Doman, D.A., Warkentin, A., and Bauer, R., 2009, "Finite Element Modeling Approaches in Grinding," *International Journal of Machine Tools and Manufacture*, **49**, pp. 109-116.

[24] Mukherjee, I. and Ray, P.K., 2006, "A Review of Optimization Techniques in Metal Cutting Processes," *Computer and Industrial Engineering*, **50**, pp. 15-34.

[25] Ross, P.J., 1989, *Taguchi Techniques for Quality Engineering*. McGraw-Hill, New York.

[26] Montgomery, D.C., 2001, *Design and Analysis of Experiments*. Wiley and Sons, New York.

[27] Alagumurthi, N., Palaniradja, K., and Soundrarajan, V., 2006, "Optimization of Grinding Process Through Design of Experiments (DOE) – A Comparative Study," *Materials and Manufacturing Processes*, **21**, pp. 19-21.

[28] Tricard, M., Gust, D.J., and Shih, A.J., 1999, "Systems Approach for the Ceramic Thru-Feed Centerless Grinding," *Machining Science and Technology*, **3(2)**, pp. 201-219.

[29] Kwak, J.S., 2005, "Application of Taguchi and Response Surface Methodologies for Geometric Error in Surface Grinding Process," *International Journal of Machine Tools and Manufacture*, **45**, pp. 327-334.

[30] Dhavlikar, M.N., Kulkarni, M.S., and Marlappan, V., 2003, "Combined Taguchi and Dual Response Method for Optimization of a Centerless Grinding Operation," *Journal of Materials Processing Technology*, **132(1-3)**, pp. 90-94.

[31] King, R.I. and Hahn, R.S., 1986, *Handbook of Modern Grinding Technology*. Chapman and Hall, New York, pp. 246-247.

[32] Farmer, D.A. and Shaw, M.C., 1967, "Abrasive Machining Economics," ASTME Paper No. MR67-595.

[33] Shaw, M.C., 1969, "Cost Reduction in Stock Removal Grinding," *Annals of the CIRP*, **17**, pp. 539-540.

[34] Hahn, R.S., 1964, "Controlled-Force Grinding – A New Technique for Precision Internal Grinding," *ASME Journal of Engineering for Industry*, **86**, pp. 287-293.

[35] Brinksmeier, E., 1991, "Self-Tuning Adaptive Control System for Grinding Process," *Annals of the CIRP*, **40**, pp. 355-358.

[36] Jenkins, H.E., 1996, "Process Estimation and Adaptive Control of a Grinding System," Ph.D. Thesis, Georgia Institute of Technology, GA.

[37] Hecker, R.L. and Liang, S.Y., 2000, "Power Feedback Control in Cylindrical Grinding Process," *Proceedings of the ASME International Mechanical Engineering Congress and Exhibition*, Orlando, FL, DSC **69**, pp. 713-718.

[38] Hekman, K., Hecker, R.L., and Liang, S.Y., 2001, "Adaptive Power Control of Cylindrical Traverse Grinding," *Proceedings of the 3rd International Conference on Metal Cutting and High Speed Machining*, Metz, France, **2**, pp. 262-264.

[39] Peters, J. and Arens, R., 1980, "Optimization Procedure of Three Phase Grinding

Cycles of Series without Intermediate Dressing," *Annals of the CIRP*, **29**, pp. 195-200.

[40] Amitay, G., Malkin, S., and Koren, Y., 1981, "Adaptive Control Optimization of Grinding," *ASME Journal of Engineering for Industry*, **103(1)**, pp. 102-111.

[41] Xiao, G., Malkin, S., and Danai, K., 1993, "Autonomous System for Multi-Stage Cylindrical Grinding," *ASME Journal of Dynamic System Measurement and Control*, **115(4)**, pp. 667-672.

[42] Dong, S., Danai, K., Malkin, S., and Deshmukh, A., 2004, "Continuous Optimal Infeed Control for Cylindrical Plunge Grinding, Part 1: Methodology," *Journal of Manufacturing Science and Engineering*, **126**, pp. 327-333.

[43] Goldberg, D.E., 2002, *Genetic Algorithms in Search, Optimization, and Machine Learning.* Pearson Education, Boston, MA.

[44] Glover, F. and Laguna, M., 2002, *Tabu Search*. Kluwer Academic Publishers, London.

[45] Kirkpatrick, K., Gelett, C.D., and Vecchi, M.P., 1983, "Optimization by Simulated Annealing," *Sciences*, **220**, pp. 671-680.

[46] Dall, A., 1946, "Rounding Effect in Centerless Grinding," *Mechanical Engineering*, **58**, pp. 325-329.

[47] Rowe, W.B. and Barash, M.M., 1964, "Computer Method for Investigating the Inherent Accuracy of Centerless Grinding," *International Journal of Machine Tool Design and Research*, **4**, pp. 91-116.

[48] Rowe, W.B., Barash, M.M., and Koenigsberger, F., 1965, "Some Roundness Characteristics of Centerless Grinding," *International Journal of Machine Tool Design and Research*, **5**, pp. 203-215.

[49] Gurney, J.P, 1964, "An Analysis of Centerless Grinding," *ASME Journal of Engineering for Industry*, **86**, pp 163-174.

[50] Romanov, V.L, 1966, "Roundness Errors in Centerless Grinding," *Machines and Tooling*, **5**, pp. 4-10.

[51] Gallego, I., 2007, "Intelligent Centerless Grinding: Global Solution for Process Instabilities and Optimum Cycle Design," *Annals of the CIRP*, **56(1)**, pp. 347-352.

[52] Pande, S.S., Naik, A.R., and Somasundaram, S., 1993, "Computer Simulation of the Plunge Centerless Grinding Process," *Journal of Materials Processing Technology*, **39**, pp. 179-189.

[53] Drobashevski, G.S., 1973, "Optimum Settings for a Centerless Grinder," *Machines and Tooling*, **44**, pp. 20-21.

[54] Chien, A.Y., 1981, "The Rounding Off Theory of Centerless Grinding," *International Journal of Machine Tool Design Research*, **21**, pp. 49-55.

[55] Udupa, N.G., Shunmugam, M.S., and Radhakrishnan, V., 1987, "Optimizing Workpiece Position in Centerless Grinding by Roundness Profile Analysis," *Precision Engineering*, **9(1)**, pp. 23-30.

[56] Shunmugam, M.S., Udupa, N.G., and Radhakrishnan, V., 1984, "A Preliminary Investigation on the Surface Finish and Roundness Error in Centerless Grinding," *Proceedings of the 11th AIMTDR*, pp. 251-258.

[57] Pande, S.S. and Lanka, B.R., 1989, "Investigations on the Through-Feed Centerless Grinding Process," *International Journal of Production Research*, **27(7)**, pp. 1195-1208.

[58] Hahn, R.S., 1954, "On the Theory of Regenerative Chatter in Precision-Grinding Operations," *Transactions of the ASME*, pp. 593-597,

[59] Hahn, R.S, 1959, "Vibrations of Flexible Precision Grinding Spindles," *ASME Journal of Engineering for Industry*, **81**, p. 201.

[60] Hahn, R.S., 1963, "Grinding Chatter: Causes and Cures," *Tool Manufacturing Engineering*, **51**, p.74.

[61] Gurney, J.P., 1962, "General Analysis of Two Degrees of Freedom Instability in Machine Tools," *Journal of Mechanical Engineering Science*, **4**, p. 53.

[62] Rowe, W.B. and Koenigsberger, F., 1965, "The Work-Regenerative Effect in Centerless Grinding," *International Journal of Machine Tool Design Research*, **4**, pp. 175-187.

[63] Hashimoto, F., Zhou, S.S., Lahoti, G.D., and Miyashita, M., 2000, "Stability Diagram for Chatter Free Centerless Grinding and Its Application in Machine Development," *Annals of the CIRP*, **49(1)**, pp. 225-230.

[64] Hashimoto, F., Lahoti, G.D., and Miyashita, M., 1998, "Safe Operations and Friction Characteristics of Regulation Wheel in Centerless Grinding," *Annals of the CIRP*, **47(1)**, pp. 281-286.

[65] Hashimoto, F. and Miyashita, M., 1979, "Friction Characteristics of Regulating Wheel and Its Evaluation in Centerless Grinding," *Lect. JSPE*, **3**, p. 169.

[66] Hashimoto, F. and Miyashita, M., 1981, "Wear Characteristics of Regulating Wheel

in Centerless Grinding," *Lect. JSPE*, **3**, p. 548.

[67] Udupa, N.G., Shunmugam, M.S., and Radhakrishnan, V., 1987, "Frictional Behavior and Its Influence on Quality in Centerless Grinding," *Wear*, **118**, pp. 147-160.

[68] Klocke, F., Friedrich, D., Linke, B., and Nachmani, Z., 2004, "Basics for In-Process Roundness Error Improvement by a Functional Workrest Blade," *Annals of the CIRP*, **53(1)**, pp. 275-280.

[69] Harrison, A.J. and Pearce, T.R., 2004, "Reduction of Lobing in Centerless Grinding via Variation of Set-Up Angles," *Key Engineering Materials*, **257**, pp. 159-164.

[70] Koenig, W. and Henn, K., 1985, "Centerless Grinding – Principles of Process Control," *VDI-Z*, **27(12)**, pp. 429-435.

[71] Rowe, W.B., Bell, W.F., and Brough, D., 1987, "Limit Charts for High Removal Rate Centerless Grinding," *International Journal of Machine Tools and Manufacture*, **27(1)**, pp. 15-25.

[72] Rowe, W.B., Ebbrell, S., and Morgan, M.N., 2004, "Process Requirements for Reduced-Cost Precision Grinding," *Annals of the CIRP*, **53(1)**, pp. 255-258.

[73] Malkin, S. and Anderson, R.B., 1974, "Thermal Aspects of Grinding, Part 1 – Energy Partition," *ASME Journal of Engineering for Industry*, **96**, p. 1177.

[74] Lefebvre, A., Lipinski, P., Vieville, P. and Lescalier, C., 2008, "Experimental Analysis of Temperature in Grinding at the Global and Local Scales," *International Journal of Machining Science and Technology*, **12**, pp. 1-14.

[75] Malkin, S. and Anderson, R.B., 1974, "Thermal Aspects of Grinding, Part 2 – Surface Temperature and Workpiece Burn," *ASME Journal of Engineering for Industry*, **96**, p. 484.

[76] Snoeys, J., Maris, M., and Peters J., 1978, "Thermally Induced Damage in Grinding," *Annals of the CIRP*, **27(2)**, pp. 571-581.

[77] Torrance, A.A., 1978, "Metallurgical Effects Associated with Grinding," *Proceedings of the 12th International Machine Tool Design and Research Conference*, p. 637.

[78] Wetton, A.G., 1969, "A Review of Theories of Metal Removal in Grinding," *Journal of Mechanical Engineering Science*, **11(4)**, p. 412.

[79] Guo, Y.B. and Janowski, G.M., 2004, "Microstructural Characterization of White Layers Formed During Hard Turning and Grinding," *Transactions of NAMRI/SME*, **32**, pp. 367-374.

[80] Jaeger, J.C., 1942, "Moving Sources of Heat and Temperature at Sliding Contacts," *Royal Society of New South Wales – Journal and Proceedings*, **76**, pp. 203-224.

[81] Carslaw, H.S. and Jaeger, J.C., 1959, *Conduction of Heat in Solids*. Oxford University Press, New York.

[82] Outwater, J.O. and Shaw, M.C., 1952, "Surface Temperatures in Grinding," *Transactions of the ASME*, **74(1)**, pp. 73-81.

[83] Hahn, R.S., 1962, "On the Nature of the Grinding Process," *Proceedings of the 3rd Machine Tool Design and Research Conference*, pp. 129-154.

[84] Ramanath, S. and Shaw, M.C., 1988, "Abrasive Grain Temperature at the Beginning of a Cut in Fine Grinding," *ASME Journal of Engineering for Industry*, **110**, pp. 15-18.

[85] Makino, Suto, and Fokushima, 1966, "An Experimental Investigation of the Grinding Process," *Journal of Mechanical Laboratory of Japan*, **12(1)**, p. 17.

[86] Des Ruisseaux, N.R. and Zerkle, R.D., 1970, "Temperature in Semi-Infinite and Cylindrical Bodies Subjected to Moving Heat Sources and Surface Cooling," *ASME Journal of Heat Transfer*, **92**, pp. 456-464.

[87] Howes, T.D., Neailey, K., and Harrison, A.J., 1987, "Fluid Film Boiling in Shallow Cut Grinding," *Annals of the CIRP*, **36(1)**, pp. 223-226.

[88] Shafto, G.R., 1975, "Creep Feed Grinding," Ph.D. Thesis, University of Bristol, England.

[89] Rowe, W.B., Black, S.C., Mills, B., Qi, H.S, and Morgan, M.N., 1995, "Experimental Investigation of Heat Transfer in Grinding," *Annals of the CIRP*, **44(1)**, pp. 329-332.

[90] Lavine, A.S., 1988, "A Simple Model for Convective Cooling During the Grinding Process," *ASME Journal of Engineering for Industry*, **110**, pp. 1-6.

[91] Jen, T.C. and Lavine, A.S., 1991A, "Thermal Aspects of Grinding: Heat Transfer to Workpiece, Wheel, and Fluid," *ASME Journal of Heat Transfer*, **113**, pp. 296-303.

[92] Jen, T.C. and Lavine, A.S., 1991B, "Coupled Heat Transfer to Workpiece, Wheel, and Fluid in Grinding, and the Occurrence of Workpiece Burn," *International Journal of Heat and Mass Transfer*, **34(4/5)**, pp. 983-992.

[93] Jen, T.C. and Lavine, A.S., 1996, "A Variable Heat Flux Model of Heat Transfer in Grinding with Boiling," *ASME Journal of Heat Transfer*, **118(2),** pp. 463-470.

[94] Yasui, H. and Tsukada, S., 1983, "Influence of Fluid Type on Wet Grinding Temperature," *Bull. Japanese Society of Precision Engineering*, **17(2)**, pp. 133-134.

[95] Kim, J.W., Howes, T.D., and Gupta, H., 1997, "The Search for an Economic Domain of Operation when Grinding Below the Film Boiling Limit," *International Journal of Machine Tools and Manufacture*, **37(4)**, pp. 391-399.

[96] Kohli, S., Guo, C., and Malkin, S., 1993, "Energy Partition to the Workpiece for Grinding with Aluminum Oxide and CBN Abrasive Wheels," *Journal of Engineering for Industry*, **117**, pp. 160-168.

[97] Guo, C., Wu, Y., Varghese, V., and Malkin, S., 1999, "Temperatures and Energy Partition for Grinding with Vitrified CBN Wheels," *Annals of the CIRP*, **48(1)**, pp. 247-251.

[98] Isenberg, J. and Malkin, S., 1974, "Effects of Variable Thermal Properties on Moving Band Source Temperatures," *ASME Journal of Engineering for Industry*, **96**, p. 1184.

[99] Kovach, J.A. and Malkin, S., 1988, "Thermally Induced Grinding Damage in Superalloy Materials," *Annals of the CIRP*, **37(1)**, p. 309.

[100] Klocke, F., 1997, "Dry Cutting," *Annals of the CIRP*, **46(2)**, pp 519-526.

[101] Yoon, S.C. and Krueger, M., 1999, "Optimizing Grinding Performance by the Use of Sol-Gel Alumina Abrasive Wheels and a New Type of Aqueous Metalworking Fluid," *Machining Science and Technology*, **3(2)**, pp. 287-294.

[102] Paul, S. and Chattopadhyay, A.B., 1995, "Effects of Cryogenic Cooling by Liquid Nitrogen Jet on Forces, Temperature, and Surface Residual Stresses in Grinding Steels," *Cryogenics*, **35(8)**, pp. 515-523.

[103] Shaji, S. and Radhakrishnan, V., 2003, "Analysis of Process Parameters in Surface Grinding with Graphite as Lubricant Based on the Taguchi Method," *Journal of Materials Processing Technology*, **141(1)**, pp. 51-59.

[104] Gopal, A. and Rao, P., 2004, "Performance Improvement of Grinding of SiC Using Graphite as Solid Lubricant," *Materials and Manufacturing Processes*, **19(2)**, pp. 177-186.

[105] Babic, D.M., Torrance, A.A. and Murray, D.B., 2005, "Soap Mist Jet Cooling of Grinding Processes," *Key Engineering Materials*, **291**, pp. 239-244.

[106] De Silva, L.R., Bianchi, E.C., Fusse, R.Y., Catai, R.E., Franca, T.V., and Aguiar, P.R., 2007, "Analysis of Surface Integrity for Minimum Quantity Lubricant – MQL in Grinding," *International Journal of Machine Tools and Manufacture*, **47**, pp. 412-418.

[107] Shen, B., Malshe, A.P., Kalita, P., and Shih, A.J., 2008, "Performance of Novel MoS_2 Nanoparticles Based Grinding Fluids in Minimum Quantity Lubrication Grinding," *Transactions of NAMRI/SME*, **36**, pp. 357-364.

[108] Ali, Y.M. and Zhang, L.C., 2004, "A Fuzzy Model for Predicting Burns in Surface Grinding of Steel," *International Journal of Machine Tools and Manufacture*, **44**, pp. 563-571.

[109] Engineer, F., Guo, C., and Malkin, S., 1992, "Experimental Measurement of Fluid Flow Through the Grinding Zone," *Transactions of the ASME*, **114**, pp. 61-66.

[110] Guo, C. and Malkin, S., 1992, "Analysis of Fluid Flow Through the Grinding Zone," *ASME Journal of Engineering for Industry*, **114**, pp. 427-434.

[111] Trmal, G., and Kaliszer, H., 1975, "Mechanics of Grinding Fluid Delivery," SME Paper No. MR75614, pp. 1-17.

[112] Davies, T.P. and Jackson, R.G., 1981, "Air Flow Around Grinding Wheels," *Precision Engineering*, **3(4)**, pp. 225-228.

[113] Shibata, J., Goto, T., Yamamoto, M., and Tsuwa, H., 1982, "Characteristics of Air Flow Around a Grinding Wheel and Their Availability for Assessing the Wheel Wear," *Annals of the CIRP*, **31(1)**, pp. 233-238.

[114] Wu, H., Lin, B., Cai, R., and Morgan, M.N., 2007, "Measurement of the Air Boundary Layer on the Periphery of a Rotating Grinding Wheel Using LDA," *Journal of Physics: Conference Series*, **76**, pp. 1-6.

[115] Trmal, G. and Kaliszer, H., 1976, "Delivery of Cutting Fluids in Grinding," *In. Mech. Eng.*, pp. 95-100.

[116] Campbell, J.D., 1995, "Optimized Coolant Application," *Proceedings of the 1st International Machining and Grinding Conference*, Dearborn, Michigan, SME, MR95-211, pp. 894-904.

[117] Baines-Jones, V.A., 2008, "System Design for Improved Useful Fluid Flow in Grinding," Ph.D Thesis, Liverpool John Moores University, England.

[118] Webster, J., 1995, "Selection of Coolant Type and Application Technique in Grinding," *Supergrinding 1995 – Polishing with Superabrasives*, Nov. 2-3, Connecticut, pp. 205-220.

[119] Vits, R., 1985, "Technologisch Aspete der Kuhlschmeirung beim Schleifen," Dr. Ing. Dissertation, Technische Hochschulle, Aachen, Germany.

[120] Brucher, T., 1996, "Kuhlschmierung beim Schleifen Keramischer Werkstoffe," Dr. Ing. Dissertation, Universität Bremen, Düsseldorf, Germany.

[121] Karpinski, T. and Sienawski, J., 2002, "Ecological Methods of Cooling in Grinding Processes," *Archives of Civil and Mechanical Engineering*, **2(1)**, pp. 73-81.

[122] Brinksmeier, E., Heinzel, C., and Wittman, M., 1999, "Friction, Cooling, and Lubrication in Grinding," *Annals of the CIRP*, **48(2)**, pp. 581-598.

[123] Klocke, F., Baus, A., and Beck, T., 2000, "Coolant Induced Forces in CBN High Speed Grinding with Shoe Nozzles," *Annals of the CIRP*, **49(1)**, pp. 241-244.

[124] Webster, J., Brinksmeier, E., Heinzel, C., Wittman, M., and Thoens, K., 2002, "Assessment of Grinding Fluid Effectiveness in Continuous-Dress Creep Feed Grinding," *Annals of the CIRP*, **51(1)**, pp. 235-240.

[125] Jakimov A.B., 1984, "Abrazivno-Almaznaja Obrabotka Fasonnych Poverchnostej, *Mašinostroenie*, pp. 117–124.

[126] Jakimov A.B., 1975, "Optimizacija Processa Slifovanija," *Mašinostroenie*, pp. 64-74.

[127] Webster, J., Cui, C., and Mindek, R.B., 1995, "Grinding Fluid Application System Design," *Annals of the CIRP*, **44(1)**, pp. 333-338.

[128] Klocke, F, Beck, T., Eisenblätter, G., and Lung, D., 2000, "Minimal Quantity Lubrication (MQL) in Cutting and Grinding," *Proceedings of the 12th International Colloquium of Industrial and Automotive Lubrication*, Essligen, Germany.

[129] Klocke, F., Beck, T., Eisenblätter, G., Fritsch, R., Lung, D., and Pöhls, M., 2000, "Applications of Minimal Quantity Lubrication – Motivation, Fundamentals, Vistas," *Proceedings of the 12th International Colloquium of Industrial and Automotive Lubrication*, Essligen, Germany.

[130] Morgan, M.N., Jackson, A.R., Wu, H., Baines-Jones, V., Batako, A., and Rowe, W.B., 2008, "Optimization of Fluid Application in Grinding," *Annals of the CIRP*, **57(1)**, pp. 363-366.

[131] Gviniashvili, V., Wooley, N.H., and Rowe, W.B., 2004, "Useful Flow Rate in Grinding," *International Journal of Machine Tools and Manufacture*, **44(6)**, pp. 629-636.

[132] Avallone, E., Baumeister, T., and Sadegh, A., 2007, *Marks' Standard Handbook for Mechanical Engineers*. McGraw-Hill, New York, pp 87-90.

[133] Donachie, M.J., 2001, *Titanium: A Technical Guide*. ASM International, pp.79-81.

[134] Hecker, R.L., Ramoneda, I.M., and Liang, S.Y., 2003, "Analysis of Wheel Topography and Grit Force for Grinding Process Modeling," *Journal of Manufacturing Processes*, **5(1)**, pp. 13-23.

[135] Snoeys, R., Peters, J., and Decneut, A., 1974, "The Significance of Chip Thickness in Grinding," *Annals of the CIRP*, **23(2)**, p. 227.

[136] Hou, Z.B., and Komanduri, R., 2003, "On the Mechanics of the Grinding Process – Part I: Stochastic Nature of the Grinding Process," *International Journal of Machine Tools and Manufacture*, **43(15)**, pp. 1579-1593.

[137] Malkin, S., and Anderson, R.B., 1972, "Active Grains and Dressing Particles in Grinding," *Proceedings of the International Grinding Conference*, Pittsburgh, PA, p. 161.

[138] Tamaki, J. and Matsui, S., 1989, "Characterization of Surface Topography of Metal Bonded Diamond Grinding Wheel," *Journal of Society of Precision Engineering*, **55(1)**, pp. 85-90.

[139] Jodan, K., Matsumaru, K., Nanko, M., and Ishizaki, K., 2003, "A Precise Method to Estimate Abrasive-Grain Protrusion Heights for Grinding Stones," *Advancements in Technology of Materials and Material Processing Journal*, **5(1)**, pp. 25-30.

[140] Abellan, J.V., Romero, F., Siller, H.R., Estruch, A., and Vila, C., 2008, "Adaptive Control Optimization of Cutting Parameters for High Quality Machining Operations Based on Neural Networks and Search Algorithms," *Advances in Robotics, Automation, and Control*. *In-Tech*, Vienna, Austria, p. 10.

[141] Marinescu, I., Hitchiner, M., Uhlmann, E., Inasaki, I., and Rowe, W.B., 2006, *Handbook of Machining with Grinding Wheels*. CRC Press, New York, pp. 418, 521-522.

[142] Rowe, W.B., Morgan, M.N., Black, S.C., and Mills, B., 1996, "A Simplified Approach to Control of Thermal Damage in Grinding," *Annals of the CIRP*, **45(1)**, pp. 299-302.

[143] Marinescu, I., Haber, B., Dimitrov, B., and Inasaki, I., 2004, *Tribology of Abrasive Machining Processes*. William Andrew Publishing, New York, pp. 138-139.

[144] Xu, X.P., Yu, Y.Q., and Xu, H.J., 2002, "Effect of Grinding Temperatures on the Surface Integrity of a Nickel-Based Alloy," *Journal of Materials Processing Technology*, **129** pp. 359-353.

[145] Chen, M., Sun, F.H., Lee, Y.M., and Yang, S.H., 2004, "Surface Quality Studies with Respect to Grinding Burn of New Typical Nickel-Based Superalloy," *Key*

*Engineering Material*s, **259**, pp. 233-238.

[146] Degouy, J., 2006, "High Efficiency Deep Grinding of Light Alloys," M.S. Thesis, Cranfield University, England.

[147] Howes, T.D., Tönshoff, H.K. and Heuer, W., 1991, "Environmental Aspects of Grinding Fluids," *Annals of the CIRP*, **40(2)**, pp. 623-629.

[148] Hafenbraedl, D. and Malkin, S., 2000, "Environmentally-Conscious Minimum Quantity Lubrication (MQL) for Internal Cylindrical Grinding," *Transactions of NAMRI/SME*, **28**, pp.149-154.

[149] Alves, J.A., Fernandes, U.B., Silva, J.C., Bianchi, E.C., Aguiar, P.R., and Silva, E.J., 2009, "Application of the Minimum Quantity Lubrication Technique in the Plunge Cylindrical Grinding Operation," *Journal of the Brazilian Society of Mechanical Sciences and Engineering*, **31(1)**, pp. 47-51.

[150] Sadeghi, M.H., Haddad, M.J., Tawakoli, T., and Emami, M., 2009, "Minimum Quantity Lubrication-MQL in Grinding of Ti-6Al-4V Titanium Alloy," *International Journal of Advanced Manufacturing Technology*, **44(5)**, pp. 487-500.

[151] Heisel, U, Lutz, D., Wassmer, R., and Walter U., 1998, "The Minimum Quantity Lubricant Technique and Its Applications in the Cutting Process," *Machines and Metals*, **386**, pp. 22-38.

[152] Reddy, N.S. and Rao, P.V., 2006, "Experimental Investigation to Study the Effect of Solid Lubricants on Cutting Forces and Surface Quality in End Milling," *International Journal of Machine Tools Design*, **46**, pp. 189-198.

[153] Mukhopadhyay, D., Banerjee, S. and Reddy, N.S., 2007, "Investigation to Study the Application of Solid Lubricant in Turning AISI 1040 Steel," *Transactions of the ASME*, **129**, pp. 520-526.

[154] Alberts, M., Kalaitzidou, K., and Melkote, S., 2009, "An Investigation of Graphite Nanoplatelets as Lubricant in Grinding," *International Journal of Machine Tools and Manufacture*, **49**, pp. 966-970.

[155] Shaji, S. and Radhakrishnan, V., 2002, "Investigations on the Application of Solid Lubricants in Grinding," *Journal of Engineering Manufacture*, **216**, pp. 1325-1343.

[156] Bryant, P.J., Gutshall, P.L., and Taylor, L.H., 1964, "A Study on Mechanisms of Graphite Friction and Wear," *Wear*, **7(3)**, pp. 118-119.

[157] Kalaitzidou, K., Fukushima, H., and Drzal, L.T., 2007, "Mechanical Properties and Morphological Characterization of Exfoliated Graphite-Polypropylene Nanocomposites," *Compos Part A-App*, **38**, pp. 1675-1682.